Streamer discharges and their interaction with dielectrics

A COMPUTATIONAL STUDY

Xiaoran Li

PhD Thesis

Streamer discharges and their interaction with dielectrics

Document Version:
Publisher's PDF, also known as Version of Record (includes final page, issue and volume numbers)

Please check the document version of this publication:

• A submitted manuscript is the version of the article upon submission and before peer-review. There can be important differences between the submitted version and the official published version of record. People interested in the research are advised to contact the author for the final version of the publication, or visit the DOI to the publisher's website.
• The final author version and the galley proof are versions of the publication after peer review.
• The final published version features the final layout of the paper including the volume, issue and page numbers.

Link to publication

Download date: 16. Oct. 2023

Streamer discharges and their interaction with dielectrics

a computational study

PROEFSCHRIFT

ter verkrijging van de graad van doctor aan de Technische Universiteit Eindhoven, op gezag van de rector magnificus, prof.dr. S.K. Lenaerts, voor een commissie aangewezen door het College voor Promoties, in het openbaar te verdedigen op maandag 30 oktober 2023 om 11:00 uur

door

Xiaoran Li

geboren te Hebei, China

Dit proefschrift is goedgekeurd door de promotoren en de samenstelling van de promotiecommissie is als volgt:

Voorzitter:	prof.dr. C. Storm	
Promotoren:	prof.dr. U.M. Ebert	
	prof.dr. A. Sun	Xi'an Jiaotong University
Copromotor:	dr. H.J. Teunissen	Centrum Wiskunde & Informatica
Leden:	prof.dr.ir. B. Koren	
	prof.dr.ir. W. Van Saarloos	Universiteit Leiden
	prof.dr. Y. Li	Xi'an Jiaotong University
	prof.dr. X. Yang	Xi'an Jiaotong University

The cover image is created by Midjourney, inspired by the stained-glass windows of The Sagrada Família.

Contents

Chapter 1

Introduction

1.1 Research background

1.1.1 Electrical discharges and streamer discharges

An electrical discharge is the release and transmission of electricity through a non-conducting medium such as a gas. It occurs when a sufficient voltage difference is applied across a medium, causing the atoms or molecules in the medium to ionize and become electrically conductive. Discharges involve a rapid multiplication of free electrons. How free electrons grow determines the type of electrical discharges. The most common mechanism for generating new free electrons in many types of discharges is impact ionization, which occurs when an electron (e) collides with an atom or molecule (M) and carries enough energy to liberate another electron from the neutral:

$$e + \mathrm{M} \rightarrow e + e + \mathrm{M}^+. \tag{1.1}$$

If the electric field is strong enough, the above process can form a chain reaction that finally leads to an electron avalanche. The concept of a Townsend discharge was proposed by John Sealy Townsend in 1897 based on the above mentioned mechanism. According to the Townsend theory, the number of electrons N_e in an avalanche from a single electron after propagating a distance d can be expressed as:

$$N_e = e^{\overline{\alpha} d}, \tag{1.2}$$

where $\overline{\alpha}$ is referred to as the effective ionization coefficient, which depends on the electric field and gas properties. However, an avalanche would not always grow according to equation 1.2. Actually, a Townsend discharge can only be sustained under certain circumstances. For instance, the Townsend discharge mechanism appeared to be applicable to cases with $pd < 133\text{-}266\,\mathrm{mbar\cdot cm}$ in air, where p represents the gas pressure and d is the gap length [1].

During an electron avalanche, charges become separated as electrons move away from positive ions. This charge separation becomes more pronounced as

the avalanche expands. As the avalanche progresses, the accumulated net charge begins to significantly influence the electric field through which it propagates. It is at this stage that the electron avalanche transitions into a streamer discharge, as proposed by Raether [2], Loeb and Meek [3–5] in the 1930s.

A streamer discharge normally has a finger-like shape, as shown in figure 1.1. The elongated shape of their channels greatly enhances the electric field at their tips. This leads to a key feature of streamer discharges: they can incept in an area with the electric field above the breakdown field and then penetrate into low-field areas. The streamer channel is quasi-neutral with equal numbers of positive and negative charges and has a relatively low field. Light is only emitted near the streamer head.
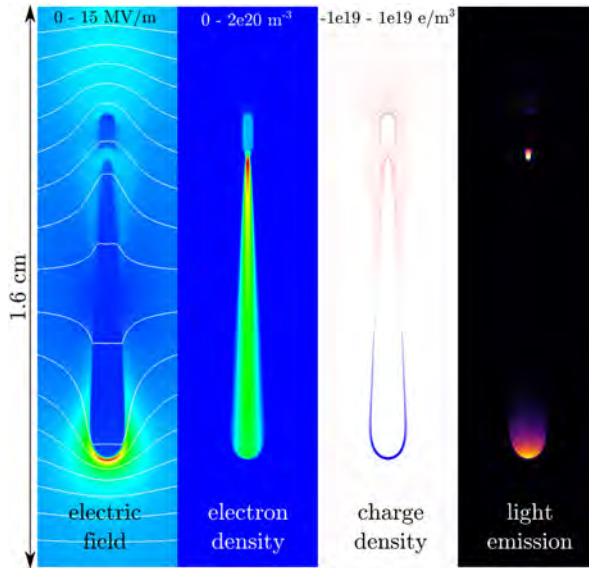
Figure 1.1: Simulation of a positive streamer propagating downwards. The simulation was performed with an axisymmetric fluid model in air at 1 bar, in a gap of 1.6 cm with an applied voltage of 32 kV. This figure is taken from [6].

Streamers do not always take the shape as depicted in figure 1.1. The actual appearance and behavior of streamers can vary depending on various factors such as the specific electrode geometry, gas compositions, and applied voltages. The shape and evolution of streamers can exhibit complex dynamics, resulting in a more intricate and irregular structure, as shown in figure 1.2. Branching streamers typically originate from a single filament streamer. Each branch retains the fundamental characteristics of a single filament streamer.

Streamer discharges can be divided into two categories according to their polarity: positive streamers and negative streamers. Negative streamers propagate against the direction of the electric field, from cathode to anode, following the electron drift. Positive streamers propagate in the opposite direction, along the
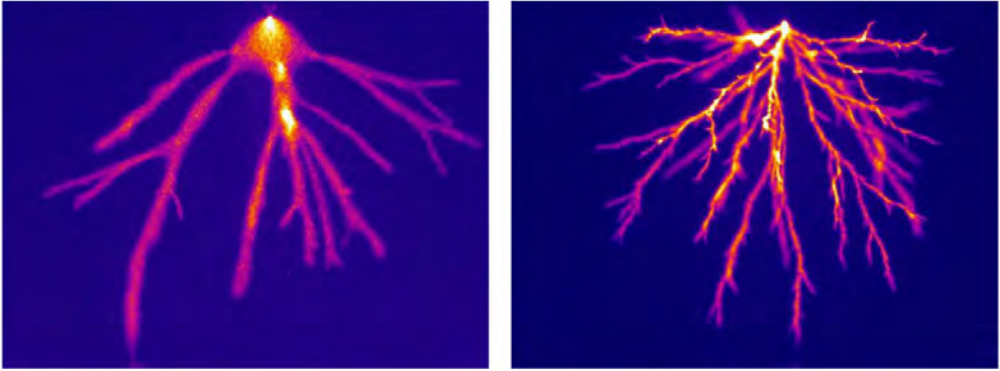
Figure 1.2: Positive streamers in air (left) and nitrogen (right), under the same conditions (4 cm needle-to-plane gap, 0.4 bar, 16 kV). The figure is taken from [7].

direction of the electric field. There are also double-headed streamers that propagate in both directions. The major difference between positive and negative streamers is that positive streamers require a source of free electrons ahead of them to grow. These electrons generate ionization in the high-field region around the streamer tip and are subsequently absorbed into the channel. In the case of air, photoionization is the main mechanism producing such electrons [8]. As negative streamers propagate in the electron-drift direction, they do not require an additional electron source ahead of them. Negative streamers in air typically require a higher voltage for initiation and propagate slower compared to their positive counterparts, as reported by [7, 9].

Streamer discharges involve a wide range of temporal and spatial scales. For a streamer in air at 1 bar and room temperature, the mean free path of electrons between collisions with neutrals is around tens of nanometers, the ionization length $1/\alpha(E)$ is around several micrometers, and the whole streamer length could be up to several centimeters. The time between collisions is usually on the order of picoseconds, while the total time for streamer propagation could be hundreds of nanoseconds to microseconds. This multi-scale nature of streamer discharges poses challenges for modeling and diagnostics.

1.1.2 Streamer discharges in nature and in industry

In nature   Lightning is the most well-known example of natural electrical discharges. Streamers create the first ionized path for lightning leaders. Streamer discharges in nature also take on various captivating forms [10]: Sprites are upper atmospheric discharges that appear as red flashes with upward-reaching tendrils above thunderstorms. St. Elmo's Fire produces bluish or violet glows around pointed objects under electrically charged conditions. Lastly, volcanic lightning occurs during volcanic eruptions, generating lightning bolts within the volcanic

plume or luminous glows near the volcano. These natural phenomena showcase the dynamic beauty and interplay between electricity and the environment.

In electrical engineering Streamer discharges serve as a precursor to the overall breakdown process in high voltage devices. These discharges initiate the formation of ionized channels, paving the way for the subsequent development of more intense and heat-dominated discharges, such as sparks or arcs. Understanding and controlling streamer discharges are crucial in high voltage technology to ensure the reliable operation and safety of electrical systems.

Other industrial applications Streamer discharges exhibit a highly non-equilibrium nature, characterized by a strong field enhancement at the streamer head. This unique feature allows electrons to transiently acquire energies of tens of electron volts (eV) while the surrounding gas remains relatively cold, enabling streamer discharges to trigger chemical reactions without significant gas heating. Consequently, streamer discharges find wide-ranging industrial applications, including plasma-assisted ignition and combustion [11], industrial surface treatment [12], plasma medicine [13] and environmental applications [14]. The ability of streamer discharges to efficiently initiate chemical reactions while minimizing energy loss through gas heating offers innovative and environmentally friendly solutions in diverse fields.

1.1.3 Streamer diagnostics

For almost a century, streamer discharges have been extensively studied through experiments, as reviewed in [6, 15, 16]. The most common strategy for studying discharges is electrical diagnostics, including voltage and/or current waveform measurements, though it only provides limited information. To gain a deeper understanding of streamer morphology, optical imaging techniques have proven valuable, utilizing tools such as ICCD cameras and streak cameras. Optical emission spectroscopy is frequently employed to identify specific species present in the discharge. Moreover, laser diagnostics have been introduced, enabling the measurement of species densities, kinetics, temperatures, and even electric fields associated with streamer discharges. These evolving diagnostic technologies provide researchers with increasingly sophisticated means to explore and comprehend the complex nature of streamer discharges.

1.1.4 Streamer modeling

Computational models can be used to study the behavior of streamer discharges by solving the governing equations that describe the physics of streamer propagation. Commonly employed simulation techniques include particle-in-cell (PIC)

methods, fluid models, and hybrid models that combine both approaches. Microscopically, the physics of a streamer discharge is governed by the dynamics of various particles, including electrons, ions, neutral gas molecules, and photons. In a particle model, the locations and velocities of these particles (in particular electrons) are tracked, and their movement is influenced by electric fields and collisions with each other. To reduce computational costs, acceleration methods, such as adaptive mesh refinement(AMR) and super-particles, are commonly adopted, which will be further discussed in section 2.3. In a fluid model, particles such as electrons, ions, and neutral gas molecules are treated as densities. The evolution of these densities is described by partial differential equations (PDEs). These models can be derived through phenomenological arguments, conservation laws, or by considering velocity moments of Boltzmann's equation. A common type of fluid model is the drift-diffusion-reaction model, which will be extensively discussed in section 2.2.

Together with the developing diagnostic technologies in the past century, numerical simulations are also increasingly used to help explain experimental results and to study the physics of streamer discharges. Simulations provide the full temporal and spatial evolution of fields and plasma species, which are experimentally challenging to obtain. Furthermore, simulations allow for the deactivation or artificial amplification of physical mechanisms, and enable exploration of inaccessible environments. By offering a detailed understanding of streamer behavior, simulations enhance research possibilities and contribute to the optimization and mitigation of streamer discharges in various applications.

1.1.5 Topics addressed in this thesis

This thesis takes a further step on previous computational studies of streamer discharges. We focus on four independent but also closely related open questions pertaining to discharges in high-voltage devices.

The first topic of this thesis involves the accuracy examination of our simulation model, which is a commonly employed model in the field. This investigation is of importance as it directly impacts the reliability and validity of our research findings.

Streamers can exhibit various behaviors in different background electric fields, including acceleration, deceleration, or stagnation. We secondly investigate how streamer properties are influenced by background electric fields, with a particular focus on steady and stagnating streamers.

Discharges rarely occur in open space without being influenced by the surrounding medium. This is particularly true in electrical equipment, where discharges tend to occur around the surfaces of solid dielectrics. Therefore, the interaction between streamers and dielectrics is the focus of our third topic.

Streamer properties are significantly influenced by the composition of the surrounding gases, making it the subject of our fourth topic. The first three

topics primarily investigate streamers in air, as it is the most extensively studied gas for streamer discharges. However, in the fourth topic, we delve into the propagation of positive streamers in gases different from air, particularly focusing on CO_2 as it represents the main component of new insulating gases.

For each of the aforementioned four topics, a comprehensive summary of previous research pertaining to each aspect is presented in section 1.2, providing a foundation for our subsequent investigations. Furthermore, in section 1.3, we provide a concise summary of the research questions and content covered in this thesis.

1.2   A summary of related past work

1.2.1   Validation of streamer discharge models

Numerical simulations are a powerful tool for studying streamer discharges, providing a cost-effective and detailed understanding of their behavior and underlying physics. How well commonly used streamer discharge models approximate physical reality is an important and still partially open question. When simulations are employed not only for qualitative comprehension but also for quantitative predictions, it becomes necessary to perform verification and validation (V&V) of simulation codes, as outlined in the work of Roache [17]. Here *verification* means ensuring the model equations are correctly solved, and *validation* means ensuring the model is consistent with experimental results.

Below, we first briefly present examples of past work in which streamer simulations and experiments were compared. Pancheshnyi et al. [18] experimentally investigated cathode-directed streamer discharges in synthetic air in a pressure range of 300 to 760 Torr and compared with axisymmetric fluid simulations. Deviations of up to 35% were observed in the anode current and in the streamer velocity. The companion papers of Briels [7] and Luque [19] presented measurements and simulations of short positive and negative streamers in air at standard temperature and pressure. Komuro et al. [20] compared the simulated and experimental light emission for discharges in a pin-plate electrode geometry using streak images. Good agreement was achieved for the propagation of the primary streamer front, and secondary streamers were observed in both the experiments and simulations. In a related publication [21] the effect of the pulse rise time was investigated, and qualitative agreement was found for the streamer development in experiments and simulations. In [22], they extended the comparison to the distribution of electron densities, and qualitative agreement was achieved.

Eichwald et al. [23] compared simulations and experiments of primary and secondary streamers in a point-plane positive corona discharge, focusing on the production of oxygen and nitrogen radicals. The experimental and simulated production of these radicals were found to be in qualitative agreement. Nijdam et al. [24] investigated the role of free electrons in the guiding of positive stream-

ers in nitrogen–oxygen mixtures through a combination of experiments and 3D simulations, with the latter supporting the experimental observations. Marode et al. [25] studied diffuse discharges with a 2D fluid model and experiments. Similar light emission structures were recognized. A related paper [26] investigated the electric field distribution in diffuse discharges at high over-voltages, using both fluid simulations and experiments. Experimentally, spectral line ratios were used to determine the electric field. Similar maximal electric field strengths were found, but several qualitative discrepancies were observed in the obtained field distributions. In contrast, in a recent comparison of a fluid model and E-FISH measurements [27], good agreement was found for the shape of the electric field profile but not for its peak amplitude. Furthermore, the light emission from discharges was compared between simulations and experiments for a glow-like discharge in [28] and for a conical discharge at high over-voltage in [29]. Good agreement for the maximal discharge diameter and estimated velocity was obtained in [29].

Ono et al. [30] have recently focused on comparing experiments and simulations. A single-filament streamer was generated from a pointed anode to a planar cathode in atmospheric-pressure air. Branching was suppressed by simultaneously generating four streamers from pointed electrodes placed around the central electrode. The experimental light emission intensity, streamer diameter, and cathode current were compared with 2D axisymmetric fluid simulations. Most of the main discharge features could be reproduced by the model but discrepancies were also observed. One reason for this could be that in the simulations a single hyperbolically shaped electrode was used to mimic the field created by the combined pointed electrodes. The streamer propagation velocity was then used to fit the tip radius of this hyperbolic electrode, whereas ideally it would be a parameter to validate.

Plasma jets are related to streamer discharges. Yousfi et al. [31] investigated the ionization wave dynamics of a low-temperature plasma jet with 1.5D fluid simulations and experiments. Similar ionization wave velocities were found both experimentally and numerically. Hofmans et al. [32] compared experimental measurements and 2D axisymmetric fluid simulations of a kHz atmospheric pressure He plasma jet. Excellent agreement was obtained for the gas mixture distribution, the discharge length and velocity and the electric field in the discharge front. Based on this, Viegas et al. [33] studied the interaction of a plasma jet with grounded and floating metallic targets both experimentally and computationally.

Finally, we also list several studies in which different streamer discharge models were compared. Li et al. [34] have compared 3D particle, fluid and hybrid simulations for negative streamers in air without photoionization in overvolted gaps. We should point out that the classical fluid model, which is also used in the present thesis, was not implemented correctly in this comparison. Markosyan et al. [35] evaluated the performance of three plasma fluid models: a first and second order drift-diffusion-reaction model based on respectively the local field approx-

imation and the local energy approximation, and a high order fluid model by Dujko et al. [36]. They compared these three models to a particle-in-cell/Monte Carlo (PIC/MC) code in 1D. Bagheri et al. [37] compared six simulation codes for 2D axisymmetric positive streamer discharges from six different research groups. Four of these codes were self-implemented and two made use of COMSOL. All groups used the same fluid model with the same transport coefficients. With sufficiently fine grids and small time steps, good agreement was observed between several codes. The code used in this thesis is among them.

1.2.2   Steady and stagnating positive streamers

Streamer properties largely relate to background electric fields. Depending on the background electric field, streamer propagation can be accelerating, steady, or stagnating. Accelerating streamers have been widely studied through numerical simulations [19, 37, 38]. Steady and stagnating streamers are numerically less investigated, even though they are closely related to an important empirical concept known as the "stability field" [39].

The "stability field" E_{st} [40] is often defined as the minimal background electric field that can sustain streamer propagation. A better understanding of the stability field would be useful for preventing electrical breakdown in electrical devices. Experimentally, stability fields have been extensively investigated [41–46]. For positive streamers in air with standard humidity ($11\,\mathrm{g/m^3}$), reported values range from 4.1 to $6\,\mathrm{kV/cm}$, with values around $5\,\mathrm{kV/cm}$ being the most common. Note that if there are multiple streamers, they will modify the background field in which each of them propagates. However, the small spread in experimental measurements indicates that the concept of a stability field nevertheless remains useful.

In [40, 41] it was suggested that a streamer would propagate with a constant velocity and radius in the stability field. This led to the concept of a "steady propagation field" in which streamer properties like velocity and radius do not change [47, 48]. Such steady propagation was recently observed in numerical simulations in air in a field of about $4.65\,\mathrm{kV/cm}$ [48], as shown in figure 1.3. In these simulations, the conductivity behind the streamer head was lost after a certain length due to electron attachment and recombination. The resulting discharge resembled the minimal streamers found in [7]. Qin *et al.* [47] proposed that steady propagation fields in air depend on streamer properties and that they could be as high as the breakdown electric field ($28.7\,\mathrm{kV/cm}$), based on energy conservation criteria [1].

Streamer stagnation is closely related to the concept of the stability field. Understanding how streamers decelerate in fields lower than their steady propagation field helps to predict the lengths of such streamers. Below, we briefly summarize some of the past work on decelerating and stagnating streamers. Pancheshnyi *et al.* [49] numerically investigated the stagnation dynamics of positive stream-
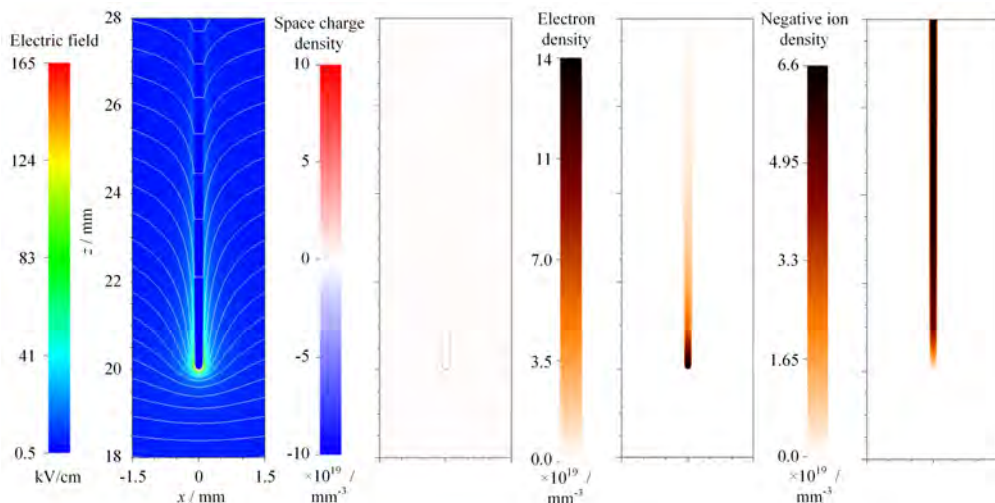
Figure 1.3: Electric field with white equipotential lines, space charge density, electron density, and negative ion density of a positive steady streamer with a background electric field of $4.65\,\mathrm{kV/cm}$. This figure is taken from reference [48].

ers with an axisymmetric fluid model. It was shown that the streamer's radius decreased as it decelerated, which led to a rapid increase in the electric field at the streamer head. More recently, Starikovskiy *et al.* [50] studied decelerating streamers in an inhomogeneous gas density with an axisymmetric fluid model. Among other things, the authors demonstrated the rather different stagnation dynamics of positive and negative streamers. In [48], it was observed that positive streamers decelerate and eventually stagnate in a background electric field below their steady propagation field. With a standard fluid model with the local field approximation, the electric field at the streamer head diverges as the streamer stagnates. In [51], suitable models for simulating positive streamer stagnation were investigated, and it was shown that the field divergence can be avoided by using an extended fluid model.

Several relations between the properties of streamers have been found in past studies, in particular between the streamer velocity and radius. In the experimental work of Briels *et al* [7], the velocity v was parameterized in terms of the diameter d as $v = 0.5d^2\mathrm{mm}^{-1}\mathrm{ns}^{-1}$, for both positive and negative streamers in an inhomogeneous field. In contrast, simulation results in [19] indicated an approximately linear relation between streamer velocity and radius for accelerating streamers. Approximate analytic results in [52] supported this quasi-linear relation, and it was shown that with certain assumptions, the maximum electric field at the streamer head can be determined from v and d.

1.2.3   Streamer discharges interacting with dielectrics

Electrical discharges in electronic devices and HV (high-voltage) equipment often occur along dielectric materials. In the regions of HV stress around an insulator, electron avalanches and streamer discharges can develop. These partial discharges may eventually result in surface flashover of the insulator, i.e., electric breakdown. In [53] it was found that around atmospheric pressure, surface flashover voltages were 10%-50% lower than flashover voltages in pure gas gaps. A dielectric present in the vicinity of the electrodes not only modifies the fields between the electrodes, but also serves as a possible source or sink of electrons during the breakdown process. Studying the interaction between dielectrics and streamer discharges is therefore important to understand surface flashover.

Early studies of surface discharges focused on the measurement of flashover voltage [54–56] and surface charge accumulation [57]. In the past few decades, the use of high-speed cameras has revealed more details about the early stages of surface discharges. In several experiments, streamer discharges were observed to have an affinity to propagate along dielectric surfaces rather than through the background gas [58, 59], as shown in figure 1.4. This affinity for a dielectric surface was reported to depend on the discharge gap geometry [60], gas composition, pressure [61], dielectric properties [62, 63] and surface charges [64–67].
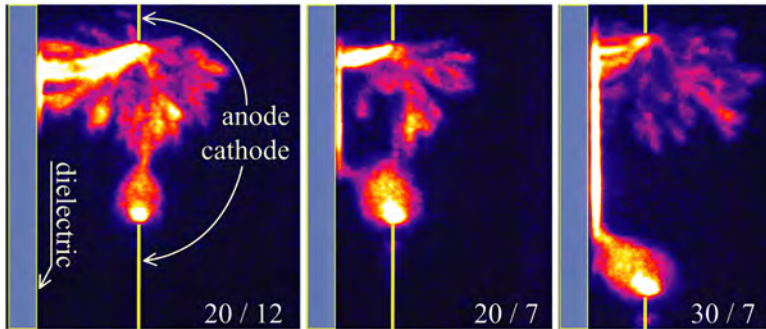
Figure 1.4: Photographs of discharges for three different geometries, specified in the right bottom corners. 20/12 denotes the geometry with 20 mm spacing between the electrodes and 12 mm between the electrodes and the dielectric, 20/7 marks the 20–7 mm and 30/7 specifies the 30–7 mm combination. Breakdown may happen along a dielectric surface or through a bulk gas depending on electrode geometries. This figure is taken from [60].

Such experimental studies can provide practical guidelines for insulation engineers. However, performing a microscopic investigation on the plasma-surface interaction, especially at atmospheric pressure, is extremely challenging, as a non-intrusive diagnostic method with a spatial resolution down to micrometers and a temporal resolution down to nanoseconds is required [68]. To gain fur-

ther insight into the physics of surface discharges, different types of numerical simulations have been performed, see e.g. [61, 69–74]. Studies on the interaction between plasmas and dielectrics have often been performed at lower pressure and in noble gases, where the discharge mechanisms are relatively well understood [75, 76]. Several authors have also studied surface discharges in atmospheric air. An incomplete list is given below.

Jorgenson *et al.* [69] investigated the role of photoemission in the surface breakdown process. With Monte Carlo simulations, they concluded that photoemission plays a role at low field values near the breakdown threshold. Celestin *et al.* [77] studied dielectric barrier discharges in air both experimentally and computationally, and highlighted the importance of surface charge. Jánský *et al.* [70] presented simulations of an air plasma discharge at atmospheric pressure, initiated by a needle anode set inside a dielectric capillary tube. Meyer *et al.* [78] studied surface streamers with a plasma fluid model in a 2D geometry. Agreement with empirical estimates for streamer propagation lengths was found, and it was observed that the surface charge quickly reaches so-called 'saturation charge' conditions. Tran *et al.* [79] performed 2D axisymmetric simulations of negative corona and barrier discharges in a needle-to-plane geometry. They validated the model parameters by comparing with experimental data. Sima *et al.* [80] used a 2D axisymmetric fluid model to identify different surface discharge stages from the electric current, in a geometry consisting of two plate electrodes and a cylindrical insulator. The resulting surface charge and the effects of the voltage amplitude and the dielectric properties were also investigated.

Numerical 2D simulations of nanosecond-pulsed surface dielectric barrier discharges of positive and negative polarity have also been performed. Babaeva *et al.* [71, 81] used a hybrid fluid-Monte Carlo model to more accurately capture secondary electron emission caused by positive ions and photons. In [82] and [71], the near-surface discharge structure and electric field were analyzed, with the latter also focusing on secondary electron emission. Furthermore, several computational studies of plasma-liquid interaction and plasma-tissue interaction have been performed at atmospheric pressure, see for example [83, 84]. In such studies, the liquid or skin is often modeled as a dielectric, sometimes with a finite conductivity.

1.2.4 Streamer discharges in gases other than air

Streamer discharges can occur in a wide range of gases. There have been some experimental as well as computational studies in different gases, such as pure noble gases (e.g. Ar, He) [85] and industrial gases (e.g. CO_2, SF_6, C_4F_7N, CH_4) and their mixtures [86, 87]. Streamer properties, such as velocities, radii, and electron densities in a streamer channel, are influenced by the gas composition in several ways, including electron ionization and attachment, electron energy losses, visibility, and photoionization [6]. Photoionization, in particular, plays a

crucial role in generating non-local free electrons. For positive streamers, which propagate along the electric field direction, the presence of free electrons ahead of the streamer head is essential [8].

Photoionization in air has been experimentally detected [88] and a computational model proposed by Zheleznyak [89] has been widely accepted. This model has also been extended to other N_2-O_2 mixtures [90]. In [91], a photoionization model was built for pure N_2 based on data from [92]. However, there is limited knowledge regarding photoionization in gases other than N_2, O_2, and their mixtures. Therefore, how positive discharges propagate in gases with low background ionization levels, other than N_2-O_2 mixtures, is often not well understood.

Among many different gases, we focus our study on CO_2 as it is increasingly used as the main component of new insulating gases to replace SF_6 in high-voltage equipment [86, 93]. The electric breakdown properties of CO_2 have been measured at different pressures and temperatures and for different voltage waveforms [94–100]. However, there are relatively few experimental studies on streamer discharges in CO_2. A challenge is that such discharges are hard to image, due to their low light emission, as shown in figure 1.5 [101]. Seeger *et al* [102] experimentally investigated the streamer stability field, streamer radius and velocity in 0.05-0.5 MPa CO_2 at positive and negative polarity. They found streamer stability fields of about $11 \pm 2\,V(m\cdot Pa)^{-1}$ for negative polarity. For positive polarity, stability fields were up to a factor of two higher, depending on the pressure, which is in strong contrast with the behavior in air. Mirpour *et al* [103] measured the delay in streamer inception in high-purity CO_2 at 0.3 bar for varying voltage waveforms, which included a 'pre-pulse' before the main pulse. The response to this pre-pulse was observed to be different in CO_2 than in air, which the authors relate to the different electron detachment mechanisms in these gases.

There are also few computational studies on streamers in CO_2. Levko *et al* [104] investigated the branching of negative streamers in atmospheric-pressure CO_2, using 2D particle-in-cell simulations. Photoionization was not included in these simulations, as it was argued to be negligible. Bagheri *et al* [105] simulated positive streamer propagation in atmospheric-pressure CO_2 with a 2D axisymmetric fluid model. They also argued that there is negligible photoionization in gases with a large CO_2 fraction, and therefore included different levels of background ionization (10^9 and $10^{13}\,m^{-3}$). With such background ionization, positive streamers were faster in CO_2 than in air when using the same background field, which seems to contradict the experimental findings of [102]. However, the authors note that fluid simulations with low background ionization densities can be unrealistic [106]. Whether positive streamers could continue propagating in low background ionization densities without additional electron sources is unclear.

We note that photoionization data, such as photon production and absorption, were reported in the sixties by Przybylski [107] and Teich [108]. With these available data, a photoionization model can be developed, allowing us to further

(a) CO$_2$ 0.1 MPa

(b) CO$_2$ 0.1 MPa

(c) Air 0.1 MPa

(d) Air 0.1 MPa
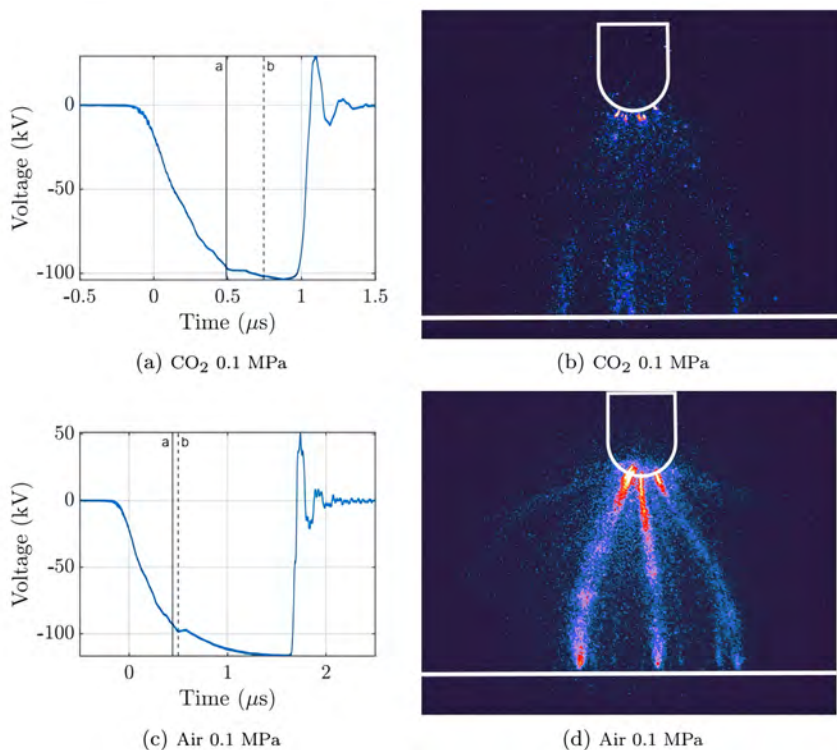
Figure 1.5: Streamer images observed in 0.1 MPa CO$_2$ and in atmospheric air. Subfigures (a) and (c) show the voltage waveforms applied on the rod-plane geometry in CO$_2$ and in air, respectively. The camera gate opening and closing are represented with the solid 'a' and dashed 'b' vertical lines. Subfigures (b) and (d) show the corresponding images of the discharges. Although subfigure (b) was taken with the maximum possible intensification of the ICCD camera, streamers in CO$_2$ are extremely dim before crossing the gap. This figure is taken from [101].

investigate the effect of photoionization on the propagation of positive streamers in CO$_2$.

1.3   Organization of the thesis

1.3.1   Research questions

Section 1.2 has provided an extensive review of previous work on streamer discharges, focusing on four specific topics addressed in this thesis. In this section, we summarize the limitations of earlier studies and emphasize the necessity of our current research.

How accurate are the simulation models? Experimental and computational results were compared with each other in many studies. Most of the studies mentioned in section 1.2.1 have reported qualitative agreement between simulations and experiments. However, quantitative comparisons remain challenging. Single streamers are relatively easy to simulate, but they are harder to generate experimentally, as demonstrated by the work of [30]. Modeling branching streamers requires 3D models, and statistical comparison is necessary, which leads to even greater computational demands. Considering computational costs, streamer simulations are typically performed using fluid models instead of particle models, and Cartesian or axisymmetric 2D models are more commonly employed compared to 3D models. Therefore, our focus is on validating the commonly used 2D axisymmetric fluid model. This is achieved by generating stable and reproducible streamers in a relatively simple geometry, and subsequently comparing the experimental results with computational results obtained from a 2D axisymmetric fluid model under closely matching conditions.

How do streamer properties relate to background electric fields? The properties of streamers are closely tied to the background electric field E_{bg}. They can be accelerating, steady, or stagnating depending on E_{bg}. An important empirical concept known as the "stability field" is defined as the minimal background field required to sustain streamer propagation. It is also considered the background field for a steady propagation streamer. However, the relationship between steady and stagnating streamers and background electric fields remains uncertain, and modeling these streamers poses a challenging task. By introducing appropriate modifications to the simulation model, we were able to generate steady and stagnating streamers under different electric field conditions. The relationship between streamer properties and background electric fields is further analyzed, shedding light on the prediction of maximum streamer length.

How do streamers interact with dielectrics? The presence of dielectrics in a gas gap can attract streamers and reduce the breakdown voltage, which has been shown by several previous experimental studies. Dielectrics can modify the distribution of the electric field and have the ability to absorb or emit electrons during discharges. However, understanding the influence of dielectrics on the discharge process is a complex task due to the involvement of multiple factors. To tackle this challenge, we have utilized simulation techniques that allow us to selectively deactivate or artificially enhance specific physical mechanisms. Through these simulations, we have made progress in elucidating how surface discharge is affected by various factors, thus uncovering the intricate interaction between dielectrics and streamer discharges.

How do positive streamers propagate in CO_2? Photoionization plays a vital role in the propagation of positive streamers by providing free electrons ahead of the streamer head. In the case of air, the photoionization mechanism is relatively well-understood, and there exists a widely accepted quantitative model. However, the understanding of how positive streamers propagate in gases different from air, particularly with a low background ionization level, remains unclear. To address this knowledge gap, our focus is on studying positive streamers in CO_2, which has much weaker photoionization compared to air. By utilizing existing photoionization data, our aim is to develop a photoionization model for CO_2 and explore whether photoionization alone can sustain positive streamer propagation in CO_2.

1.3.2 Content of the thesis

In chapter 1, we have provided an introduction to fundamental aspects of streamer discharges and offer a brief overview of previous studies. We then highlighted the necessity of our work.

In chapter 2, modeling methods of streamer discharges are introduced.

In chapter 3, we compare simulations and experiments of single positive streamer discharges in air at 100 mbar via a 2D axisymmetric drift-diffusion-reaction fluid model aiming towards model validation. Streamer velocities, radii and light emission profiles are compared between simulations and experiments. The effect of various parameters on the computational results is studied.

Chapter 4 addresses two main topics: steady propagation fields for positive streamers in air and streamer deceleration in fields below the steady propagation field. We generate constant-velocity positive streamers in air by initially adjusting the applied voltage based on the streamer velocity. The properties of steady streamers are analyzed. Stagnating streamers are simulated by applying a constant applied voltage. We show how properties of these streamers relate to the steady cases.

In chapter 5, we simulate streamer discharges that propagate towards a dielectric surface, attach to it, and then propagate over the surface. The differences between surface streamers and streamers in bulk gas are compared. The effects of the applied voltage, the dielectric permittivity and the electron emission from the dielectric surface and the preset surface charge on the propagation of surface streamers are investigated.

In chapter 6, we study the effect of photoionization on positive streamer propagation in CO_2 with 2D particle-in-cell simulations. Furthermore, we propose a self-sustaining criterion for streamer discharges in CO_2 and discuss the uncertainties in the photoionization model.

In chapter 7, we summarize the main conclusions of this thesis and give an outlook.

Chapter 2

Simulation Model

2.1 Introduction

Streamer discharges can be described via different kinds of simulation models. In this thesis, we use a drift-diffusion-reaction type fluid model with the local field approximation to simulate streamers in air. The discharges in CO_2 are simulated with a particle-in-cell model with Monte Carlo collisions. The fluid and particle models are based on `afivo-streamer` and `afivo-pic`, respectively. Both `afivo-streamer` and `afivo-pic` are open source codes based on the Afivo framework [109], which features adaptive mesh refinement (AMR), geometric multigrid methods for Poisson's equation, and OpenMP parallelism. For a comparison between `afivo-streamer` and five other simulation codes see [37]. In [110], fluid simulations with `afivo-streamer` were compared against particle-in-cell simulations with `afivo-pic` in 2D and 3D, generally finding good agreement. In this chapter, we introduce several essential components of both fluid and particle models. The governing equations of a fluid model and a particle model are given in section 2.2 and 2.3, respectively. Section 2.4 to 2.7 present basic information on the field solver, photoionization, mesh refinement and time integration, respectively. Further details about `afivo-streamer` and `afivo-pic` can be found in references [109, 111, 112]. Detailed information about computational domains and initial conditions used in the simulations of each chapter is given in the respect chapter.

2.2 Fluid model

In a drift-diffusion-reaction type fluid model, the temporal evolution of the electron density (n_e) is given by

$$\partial_t n_e = -\nabla \cdot (-n_e \mu_e \vec{E} - D_e \nabla n_e) + S, \qquad (2.1)$$

Table 2.1: An example reactions list, with reaction rates and references.

No.	Reaction	Reaction rate coefficient	Reference
1	$e + N_2 \xrightarrow{k_1} e + e + N_2^+$ (15.60 eV)	$k_1(E/N)$	[115, 116]
2	$e + N_2 \xrightarrow{k_2} e + e + N_2^+$ (18.80 eV)	$k_2(E/N)$	[115, 116]
3	$e + O_2 \xrightarrow{k_3} e + e + O_2^+$	$k_3(E/N)$	[115, 116]
4	$e + O_2 + O_2 \xrightarrow{k_4} O_2^- + O_2$	$k_4(E/N)$	[115, 116]
5	$e + O_2 \xrightarrow{k_5} O^- + O$	$k_5(E/N)$	[115, 116]

where μ_e is the electron mobility, D_e the electron diffusion coefficient, $\vec{E}$ the electric field and S the sum of source terms. The sum of source terms S depends on the reactions included in a simulation. Normally, it consists of source terms for impact ionization, attachment, detachment, electron–ion recombination and non-local photoionization.

The temporal evolution of ion species n_j can be described by

$$\partial_t n_j = -\nabla \cdot (\pm n_j \mu_{\text{ion}} \vec{E}) + S_j, \qquad (2.2)$$

where S_j is the sum of source terms for n_j, μ_{ion} is the ion mobility, and $\pm$ is the sign of the species' charge.

Plasma-chemical reactions for non-equilibrium discharges in nitrogen-oxygen mixtures are complex [113]. In fluid simulations, the consideration of chemical reactions can vary from extensive models involving hundreds of reactions [114] to simplified approaches that focus on effective ionization rates [37]. The selection of chemical reactions to include in a plasma simulation is determined by the specific physical and chemical processes that are important for the system under study. In table 2.1 we give a simple reaction list as an example which includes electron impact ionization (k_1 – k_3) and electron attachment (k_4, k_5). According to table 2.1, the impact ionization S_i and the electron attachment source term S_{attach} are calculated as,

$$S_i = n_e[N_2]k_1 + n_e[N_2]k_2 + n_e[O_2]k_3, \qquad (2.3)$$
$$S_{\text{attach}} = n_e[O_2]^2 k_4 + n_e[O_2]k_5, \qquad (2.4)$$

where $[N_2]$ indicates the number density of N_2, the same for $[O_2]$, and k_j, $j = 1, 2, ..., 5$ are the respective reaction rate coefficients.

In a fluid model with the local field approximation, transport coefficients (μ_e, D_e) and reaction coefficients related to electrons depend on the reduced electric field E/N. These coefficients can be computed from electron-neutral collision cross sections using Boltzmann solvers [116–118] or Monte Carlo swarm simulations [119, 120]. For N_2 and O_2, there are several sets of cross sections

available on LXCat [121, 122], such as Phelps [115, 123], IST Lisbon [124–126], Morgan [127], TRINITI [128] and Biagi [119, 129] databases. A commonly used two-term Boltzmann solver is BOLSIG+ [116], which is also available online via lxcat.net.

2.3   Particle model

In a particle-in-cell (PIC) model, charged particles (electrons and ions) are represented by a large number of computational particles. The particles' trajectories are tracked by solving Newton's equations of motion, taking into account the forces from the electric field and collisions with neutrals. To compute the electric field, particles are mapped to a charge density on a numerical grid. As the particles move, the charge on the grid changes, modifying the electric field for the subsequent time step.

2.3.1   Particle movements and collisions

In a particle-in-cell simulation, charged particles are accelerated by the electric field and stochastically collide with neutral gas molecules. Their coordinates $\mathbf{x}$ and velocities $\mathbf{v}$ are advanced with the "velocity Verlet" scheme [130] as:

$$\mathbf{x}(t + \Delta t) = \mathbf{x}(t) + \Delta t \mathbf{v}(t) + \frac{1}{2}\Delta t^2 \mathbf{a}(t), \tag{2.5}$$

$$\mathbf{v}(t + \Delta t) = \mathbf{v}(t) + \frac{1}{2}\Delta t[\mathbf{a}(t) + \mathbf{a}(t + \Delta t)], \tag{2.6}$$

where the acceleration $\mathbf{a} = q/m_q \mathbf{E}$ in which $\mathbf{E}$ is the electric field and q/m_q represents charge over mass.

In this thesis, we specifically consider discharges that are weakly ionized with ionization degrees ranging from 10^{-5} to 10^{-4}. At such low ionization levels, electron-neutral collisions are the dominant process, thus electron-electron and electron-ion collisions are neglected. Additionally, in nanosecond time scale simulations, ions hardly move due to their low mobility compared to electrons, we therefore describe the electrons as particles and the ions as densities here. Isotropic scattering is assumed for collisions. Electron-neutral scattering cross sections for many different gases can be obtained from LXCat, mainly including elastic scattering, inelastic scattering (e.g. electronic excitations), electron impact ionization, and electron attachment. Electron–neutral collisions are handled with the null-collision method proposed in reference [131].

2.3.2   Super-particles

In PIC-MCC simulations, it is often necessary to use super-particles to represent a group of real particles. This is because simulating the motion and behavior

of individual particles in a plasma discharge can be computationally expensive and time-consuming. Super-particles can be considered as a bundle of real particles that are treated as a single entity in the simulation. By grouping particles together, super-particles are assigned higher weights than real particles.

The weights of super-particles (how many physical particles they stand for) are adaptively controlled to obtain a desired number of simulated particles per cell N_{ppc} [112]. The desired particle weights w then can be calculated as

$$w = n_e \times \Delta V / N_{\mathrm{ppc}}, \tag{2.7}$$

where n_e is the electron density in a cell, ΔV the volume of the grid cell.

Particle weights are adjusted under specific conditions in the simulation, including when the number of particles increases by a factor of 1.25, when there is a change in the mesh, or after a certain number of time steps. When the weight of a particle falls below $2/3w$, it is combined with another nearby particle of similar energy into a single particle with a combined weight equal to the sum of the original particles. The resulting merged particle gets its position and velocity randomly from one of the original particles. Conversely, when the weight of a particle exceeds $3/2w$, it is split into two particles of equal weight, with identical copies added to the simulation that will soon deviate due to random collisions.

2.4 Field solver

Electric field profiles are needed both for fluid and particle models to control the movement of charged particles. The electrostatic approximation is commonly employed for calculating the electric fields of streamer discharges, as discussed in section 5.1 of [6].

In the electrostatic approximation, the electric field $\vec{E}$ is computed as $E = -\nabla\phi$ after solving Poisson's equation for the electric potential ϕ:

$$\nabla \cdot (\varepsilon_0 \nabla \phi) = -\rho, \tag{2.8}$$

where ε_0 is the vacuum permittivity and ρ is the space charge density.

For surface discharges, the permittivity (ε) undergoes a jump from ε_1 to ε_2 at the dielectric-gas interface. Additionally, surface charges (σ_s) accumulate on the dielectric surface. This poses a challenge for the Poisson solver in our model: the right-hand side of Poisson's equation is defined at the cell center, while the surface charge is defined at the cell face. To address this, we introduce δ_s, which maps the surface charge σ_s on the gas-dielectric interface to the grid cells adjacent to the dielectric according to the dielectric permittivity on each side. The modified form of equation 2.8 is as follows:

$$\nabla \cdot (\varepsilon \nabla \phi) = -(\rho + \delta_s \sigma_s). \tag{2.9}$$

Specifically, $\delta_s = \varepsilon_1/(\varepsilon_1 + \varepsilon_2)$ on the side with a permittivity of ε_1, and $\delta_s = \varepsilon_2/(\varepsilon_1 + \varepsilon_2)$ on the other side.

The discrete form of $\varepsilon \nabla \phi$ at the interface is given by

$$\frac{\varepsilon_1 \varepsilon_2}{\varepsilon_1 + \varepsilon_2} \frac{\phi_{i+1} - \phi_i}{\Delta r}, \tag{2.10}$$

where ϕ_{i+1} and ϕ_i are the potentials on each side of the interface, and Δr is the grid spacing. The harmonic mean of the dielectric permittivities on two sides is used as the permittivity at the interface [109].

In the Afivo framework, a geometric multigrid method [132] is used to solve Poisson's equation. The basic idea behind geometric multigrid methods is to use a hierarchy of grids, each with successively finer resolution, to accelerate the solution of the PDE. The coarsest grid represents the problem at a low level of detail, while the finest grid represents the problem with high accuracy. The solution is first approximated on the coarsest grid and then improved iteratively on finer grids until the desired level of accuracy is achieved.

Geometric multigrid methods are among the fastest methods for solving elliptic equations and are well-suited for adaptively refined meshes [109]. Unlike traditional methods, geometric multigrid is matrix-free, which means that changes in the mesh do not result in additional computational costs. However, it is important to note that the operator must be well-defined on the coarse grid levels, which can complicate the implementation of irregular boundaries that do not align with the mesh.

2.5 Photoionization

Photoionization is a physical process in which an atom or molecule is ionized by absorbing a photon with sufficient energy to eject one or more electrons from the target species, resulting in free electrons and positive ions. This process can have a significant impact on the properties of streamer discharges, particularly for positive streamers that propagate against the electron drift velocity and require a source of free electrons in front of them.

Photoionization in N_2-O_2 mixtures has been widely studied [8, 9, 38, 88, 133, 134]. The ionization of O_2 molecules due to the absorption of the emission produced by excited N_2 is the dominant photoionization process for streamer discharges in N_2-O_2 mixtures. A commonly used model for photoionization is Zheleznyak's model [89], which is also employed in this thesis. Assuming that ionizing photons do not scatter and that their direction is isotropically distributed, the photoionization source term $S_{\text{ph}}(r)$ can be given by

$$S_{\text{ph}}(r) = \int \frac{I(r')f(|r - r'|)}{4\pi|r - r'|^2} d^3 r', \tag{2.11}$$

where $I(r)$ is the source of ionizing photons, and $f(r)$ is the absorption function that gives the probability density of photon absorption at a distance r. According to Zheleznyak et al [89], $f(r)$ is expressed as

$$f(r) = \frac{\exp(-\mu_{\min}p_{O_2}r) - \exp(-\mu_{\max}p_{O_2}r)}{r\log(\mu_{\max}/\mu_{\min})}, \qquad (2.12)$$

where $\mu_{\min}$ and $\mu_{\max}$ are the pressure-reduced absorption coefficients, which are around $0.035\,\mathrm{cm}^{-1}\,\mathrm{Torr}^{-1}$ and $2\,\mathrm{cm}^{-1}\,\mathrm{Torr}^{-1}$, respectively, and p_{O_2} is the partial pressure of oxygen.

The source of ionizing photons $I(r)$ is proportional to the electron impact ionization source term S_i:

$$I(r) = \frac{p_q}{p + p_q}\xi S_i, \qquad (2.13)$$

where p is the gas pressure, $p_q = 40\,\mathrm{mbar}$ the quenching pressure, and ξ a field-dependent proportionality factor, which is in the range of 0.05 to 0.12 when the reduced electric field E/N is between 100 and 600 Td [89, 112].

The absorption function $f(r)$ in the integrand of equation 2.11 complicates the numerical solution of the photoionization source term $S_{\mathrm{ph}}(r)$. Several previous studies proposed different approximations to solve $S_{\mathrm{ph}}(r)$ more efficiently, such as [133, 135–138]. In this thesis, a continuum approach named Helmholtz method [135, 136] is utilized in chapters 3 and 4. A stochastic (Monte Carlo) approach, as described in chapter 11 of [139], is employed in chapter 5.

There is limited knowledge regarding photoionization in discharges in unitary gases. Specifically, in pure O_2 and N_2 gases, it is suggested that ionizing photons are primarily generated through electron impacts, either by direct dissociative excitation (O_I, N_I) or by direct ionizing excitation (O_{II}, N_{II}), followed by radiative transitions of the excited neutral atom or ion, respectively [92]. Studies on photoionization in pure CO_2 are even more limited [92, 108], and we explore this topic further in chapter 6.

2.6 Mesh refinement

Streamer discharges are characterized by a range of length scales, from the small-scale ionization processes at the tip of the streamers to the larger-scale behavior of the streamer as a whole. For computational efficiency, `Afivo` framework uses adaptive mesh refinement (AMR), which allows the grid to be refined in regions where the solution has a large gradient, while keeping the grid coarser in regions where the solution is relatively smooth. The refinement criterion is based on $1/\alpha(E)$, which is the average distance between ionization events for an electron [111]:

$$\text{refine if } \Delta x > c_0 c_1/\alpha(c_1 E), \qquad (2.14)$$

$$\text{de-refine if } \Delta x < \min\{0.125\,c_0 c_1/\alpha(c_1 E),\, d_0\} \qquad (2.15)$$

where $\alpha(E)$ is the field-dependent ionization coefficient, Δx is the grid spacing, and c_0, c_1 and d_0 are constants. Here c_1 is used to balance the refinement ahead and on the sides of the streamer. The specific values of these parameters are provided in each chapter.

2.7   Time integration

For the fluid simulations in this thesis, time integration was performed with Heun's method, a two-step explicit second order Runge-Kutta scheme, for more details see section 2.4 of [111]. The time step is limited according to

$$\Delta t_{\mathrm{cfl}} \left(\tfrac{4D_e}{\Delta x^2} + \sum \tfrac{v_i}{\Delta x} \right) \leq 0.5, \tag{2.16}$$

$$\Delta t_{\mathrm{drt}} \left(e\mu_e n_e/\varepsilon_0 \right) \leq 1, \tag{2.17}$$

$$\Delta t = 0.9 \times \min(\Delta t_{\mathrm{drt}}, \Delta t_{\mathrm{CFL}}), \tag{2.18}$$

where Δt_{cfl} corresponds to a CFL condition (including diffusion), Δt_{drt} corresponds to the dielectric relaxation time, and Δt is the actual time step used in the simulations. The simulations in this thesis are not sensitive to the time step, i.e., changing the safety factor from 0.9 to 0.5 hardly affects the results.

For the particle simulations, the time step is calculated in the following form [112, 140]:

$$\Delta t_{\mathrm{cfl}} \tfrac{v_{\max}}{\Delta x_{\min}} \leq 0.5, \tag{2.19}$$

$$\Delta t_{\mathrm{drt}} \left(e\mu_{e,\max} n_e/\varepsilon_0 \right) \leq 1, \tag{2.20}$$

$$\Delta t = \min(\Delta t_{\mathrm{drt}}, \Delta t_{\mathrm{cfl}}), \tag{2.21}$$

where $\Delta x_{\min}$ is the minimum grid spacing, $\mu_{e,\max}$ is the maximal electron density, and $v_{\max}$ is an estimate of the particle velocity at the 90%-quantile, which prevents a few fast particles from affecting Δt_{cfl}.

Chapter 3

Comparing simulations and experiments of positive streamers in air: steps toward model validation

We compare simulations and experiments of single positive streamer discharges in air at 100 mbar, aiming towards model validation. Experimentally, streamers are generated in a plate-plate geometry with a protruding needle. We are able to capture the complete time evolution of reproducible single-filament streamers with a ns gate-time camera. A 2D axisymmetric drift-diffusion-reaction fluid model is used to simulate streamers under conditions closely matching those of the experiments. Streamer velocities, radii and light emission profiles are compared between model and experiment. Good qualitative agreement is observed between the experimental and simulated optical emission profiles, and for the streamer velocity and radius during the entire evolution. Quantitatively, the simulated streamer velocity is about 20% to 30% lower at the same streamer length, and the simulated radius is about 1 mm (20% to 30%) smaller. The effect of various parameters on the agreement between model and experiment is studied, such as the used transport data, the background ionization level, the photoionization rate, the gas temperature, the voltage rise time and the voltage boundary conditions. An increase in gas temperature due to the 50 Hz experimental repetition frequency could probably account for some of the observed discrepancies.

This chapter is adapted from the following publication:

Xiaoran Li, Siebe Dijcks, Sander Nijdam, Anbang Sun, Ute Ebert and Jannis Teunissen. Comparing simulations and experiments of positive streamers in air: steps toward model validation. *Plasma Sources Science and Technology*, 30(9): 095002, 2021.

The introduction and simulation model sections have been condensed for conciseness in this adaptation.

Siebe Dijcks built the experimental setup, and performed the experiments. Xiaoran Li performed the simulations and comparisons, and wrote the paper.

3.1 Introduction

Numerical simulations are a powerful tool to help explain experimental results and to study the physics of streamer discharges. How well commonly used streamer discharge models approximate physical reality is an important question which is still partially open. If simulations are not just used for qualitative understanding but also for quantitative predictions, the verification and validation [17] of simulation codes are required. In this chapter, we take steps towards model validation for streamer discharges, extending past validation work [18, 30]. A summary of the approach taken in this chapter is given below:

- We experimentally generate stable and reproducible single positive streamers in air in a plate-plate geometry with a protruding needle.

- With a camera with ns gate time, the time evolution of the streamers was captured in great detail, as well as the shape of the emission profiles.

- A 2D axisymmetric fluid model was used to simulate streamers under conditions closely matching those of the experiments, e.g. using the same applied voltage waveform, gas, and electrode geometry.

- The model includes light emission, and this light emission is processed to be directly comparable with the experimental observations.

- We perform quantitative comparisons of streamer velocities, radii and light emission profiles between model and experiment.

- The effect of various parameters on the agreement between model and experiment is studied, such as numerical convergence, transport data sources, background ionization levels, photoionization rates, gas temperatures, voltage rise times and voltage boundary conditions.

For the simulations in this chapter, we use a drift-diffusion-reaction type fluid model with the local field approximation as described in section 2.2 and section 3.2.2. The computational domain and other specific settings are also given in section 3.2.2. To check how reliable simulations are, we first study the deviation between experimental and simulation results in section 3.3. Then we perform parameter studies to investigate possible sources of the observed discrepancies in section 3.4.

3.2 Experimental & Simulation Methods

3.2.1 Experimental method

Since streamer discharges are a reaction of a gaseous medium to strong electric fields, having good control over both the field and the gas is essential. We use

a quasi-cylindrical vessel (as shown in figure 3.17) with a diameter of 324 mm and a height of 380 mm for which the discharge operating pressure range is 1–1000 mbar.

The vessel is grounded and the electrode geometry inside it is illustrated in figure 3.1. An elevated grounded plate with a 6 cm radius is positioned 10 cm from the HV (high voltage) electrode, which has a 4 cm radius. A 1 cm long needle electrode with a 0.5 mm radius is connected to the HV electrode. This cylindrical electrode ends in a cone with a 60° top angle that transitions into a spherical tip with a radius of curvature of 50 μm. The plate-plate geometry with a protruding needle results in a field that is approximately homogeneous in the gap, which suppresses streamer branching. The cylindrical symmetry of the vessel is broken at a distance of about 15 cm from its center due to windows for optical access.
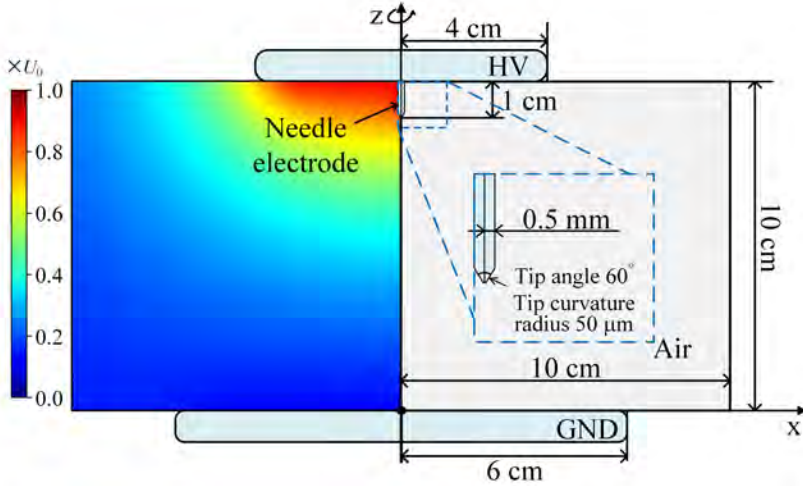
Figure 3.1: The electrode geometry in the experiments and simulations, consisting of parallel plates and a needle electrode from which discharges start. Right: the computational domain, for which $0 \leq r, z \leq 10$ cm. The needle electrode is inside the computational domain and the plate electrodes are on its upper and lower boundary. We use a coordinate system in which the electrode tip is at $z = 90$ mm and the grounded plate electrode is at $z = 0$ mm. Left: the electric potential in the absence of space charge.

A strong field is generated at the protruding needle by applying a fast HV pulse. The high voltage is generated by a DC source (Spellman Bertan 205B), which charges a discharging capacitor (40 kV | 2000 pF), which in turn is discharged by a HV switch (Behlke HTS 651-15-Sic-GSM) coupling the charged capacitor to the HV electrode for 200 ns at 50 Hz with 350 ps jitter on the start time. The voltage waveform at the HV electrode is shown in figure 3.2.

Figure 3.2: The voltage waveform as measured at the HV electrode. This waveform is also used in the simulations.

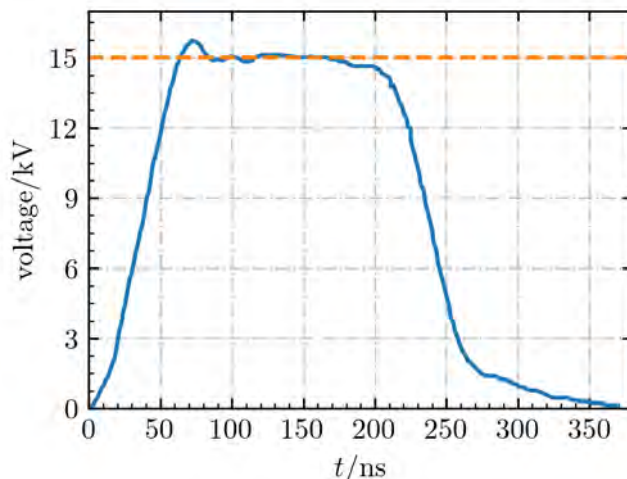Imaging is performed using an UV optimized ICCD (Lavision PicoStar HR + UV 105 mm lens) system. The CCD is synchronized with the discharge repetition rate, such that one discharge is imaged per exposure. The intensifier is then directly gated, where a gate of 900 ps is sequentially delayed through the voltage waveform, creating a phase-resolved sequence of images depicting the propagation of the streamer. Each image has an effective resolution of about 0.2 mm per pixel for the 10 cm discharge gap. Most of the image intensity comes from the decay of excited nitrogen molecules in the plasma, with the second positive system contributing most, and smaller contributions from the first positive and negative systems.

With a 50 Hz repetition rate remnants from previous discharges reduce the stochasticity in streamer inception [141]. This greatly improves the stability of the discharges and thus the quality of the measurements. Besides inception, the propagation of consecutive discharges is essentially independent of that of previous ones at 50 Hz [141, 142]. Slight changes in frequency hardly affect streamer behavior, but changing the frequency by an order of magnitude leads to visually observable differences.

All experiments were performed with the vessel at room temperature, and a pressure controller kept the pressure inside the vessel at 0.1 bar, with about 1% uncertainty. The vessel was continuously flushed with 2 SLM synthetic air while performing the experiments, giving a residence time of a couple of minutes.

3.2.2   Simulation model

We use a drift-diffusion-reaction type fluid model with the local field approximation to simulate positive streamers in artificial air, composed of 80% nitrogen and 20% oxygen at 300 K and 0.1 bar. Two-dimensional axisymmetric simulations are performed with `Afivo-streamer` [111], see detailed model description in chapter 2.

Photoionization

In the simulations of this chapter, the proportionality factor ξ (see equation (2.13)) in the photoionization model is set to 0.075 [89, 112]. The effect of ξ is investigated in section 3.4.5. Note that the factor $p_q/(p + p_q)$ is about 7.4 times larger at 0.1 bar than at 1 bar, so that there is significantly more photoionization at 0.1 bar. The absorption of the ionizing photons is computed using the Helmholtz approximation with Bourdon's three-term expansion for the absorption function, as described in [38, 135].

Reactions and light emission

The reactions considered in this chapter are listed in table 3.1, including electron impact ionization (k_1 - k_3), electron attachment (k_4, k_5) and reactions related to light emission (k_6 - k_9). All transport and reaction coefficients ($k_1 - k_6$) depend on the reduced electric field E/N, and they were computed using BOLSIG+ [143] with Phelps' cross sections for (N_2, O_2) [115, 123]. In section 3.4.3 the effect of different cross sections and Boltzmann solvers is compared. Ions are assumed to be immobile.

   To compare with the experimental observations, light emission of the second positive system of nitrogen is modeled. The corresponding $N_2(C^3\Pi_u \rightarrow B^3\Pi_g)$ transition is the main source of emitted light for nanosecond discharges in $N_2 - O_2$ mixtures around atmospheric pressure [144]. In table 1, k_6 is the electronic excitation rate of the $N_2(C^3\Pi_u)$ level from the ground state; k_7 and k_8 are the quenching rate constants for N_2 and O_2, respectively; the radiative lifetime of $N_2(C^3\Pi_u)$ is $1/k_9 = 42$ ns [18].

Computational domain & simulation conditions

The axisymmetric computational domain shown in figure 3.1 (the grey square) was designed to closely resemble the experimental geometry. The domain consists of the region $0 \leq r, z \leq 10$ cm, which covers the gap bounded by the plate electrodes. As in the experiments, a 1 cm long needle electrode is inserted at the HV electrode, with a 0.5 mm radius. The electrode tip is a cone with a 60° top angle that ends in a spherical tip with a radius of curvature of about 50 μm, just as in the experiments. The potential at the contour of the needle electrode is

Table 3.1: Reactions included in the model, with reaction rates and references.

No.	Reaction	Reaction rate coefficient	Reference
1	$e + N_2 \xrightarrow{k_1} e + e + N_2^+$ (15.60 eV)	$k_1(E/N)$	[115, 116]
2	$e + N_2 \xrightarrow{k_2} e + e + N_2^+$ (18.80 eV)	$k_2(E/N)$	[115, 116]
3	$e + O_2 \xrightarrow{k_3} e + e + O_2^+$	$k_3(E/N)$	[115, 116]
4	$e + O_2 + O_2 \xrightarrow{k_4} O_2^- + O_2$	$k_4(E/N)$	[115, 116]
5	$e + O_2 \xrightarrow{k_5} O^- + O$	$k_5(E/N)$	[115, 116]
6	$e + N_2 \xrightarrow{k_6} e + N_2(C^3\Pi_u)$	$k_6(E/N)$	[115, 116]
7	$N_2(C^3\Pi_u) + N_2 \xrightarrow{k_7} N_2 + N_2$	$k_7 = 0.13 \times 10^{-16}\,\mathrm{m^3 s^{-1}}$	[18]
8	$N_2(C^3\Pi_u) + O_2 \xrightarrow{k_8} N_2 + O_2$	$k_8 = 3.0 \times 10^{-16}\,\mathrm{m^3 s^{-1}}$	[18]
9	$N_2(C^3\Pi_u) \xrightarrow{k_9} N_2(B^3\Pi_g)$	$k_9 = 1/(42\,\mathrm{ns})$	[18]

fixed at the applied voltage, which was implemented by modifying the multigrid methods in [109] using a level-set function [145].

In the radial direction, the domain extends up to 10 cm, which is less than the vessel radius (16.2 cm). The effect of the finite plate electrodes is simulated by using pre-computed Dirichlet boundary conditions on the upper and lower boundaries. These boundary conditions were obtained by solving for the electric potential in the entire discharge vessel in the absence of a discharge, using a finite element model. The resulting potential is shown in figure 3.1. Homogeneous Neumann boundary conditions are applied for the electric potential in the radial direction. However, these boundary conditions may not closely match the experiments, but it is hard to use more correct ones. More information about how boundary conditions affect the results is given in section 3.4.9. In the presence of a discharge the potential distribution at the upper and lower domain boundaries changes, but computational experiments showed that these changes were not significant. For simplicity, we therefore keep the potential profile at the top and bottom boundary fixed. These profiles are normalized and scaled with the actual applied voltage on the HV electrode (U_0), so that we can account for the voltage rise time. In section 3.4.8, we study how the size of the plate electrodes affects streamer properties.

For all plasma species densities, homogeneous Neumann boundary conditions are used on all the domain boundaries. At the needle electrode electron fluxes are absorbed but not emitted, and secondary electron emission was not taken into account since a positive voltage was applied.

This is the first time we employ a needle electrode in `Afivo-streamer`. In previous computational studies, an elongated ionized seed was often used as a pseudo-electrode to start a streamer, see e.g. [105, 146]. We compared the

Table 3.2: A summary of simulation conditions. The sections in which the respective parameters are varied are indicated. The parameter c_0 is used for grid refinement, see section 3.4.1.

Parameter	Value	Section
Gas composition	80% N_2, 20% O_2	-
Gas pressure	0.1 bar	-
Gas temperature	300 K	3.4.6
Applied voltage	15 kV, 65 ns rise time, see Fig. 3.2	3.4.7
Initial ionization	10^{11} m^{-3} electrons and positive ions (uniform)	3.4.4
Numerical grid	$\Delta x_{\min} = 6.1\,\mu\text{m}$ $(c_0 = 0.5)$	3.4.1

differences between starting a streamer with an electrode and with an initial ionized seed in section 3.4.10.

The conditions used for the discharge simulations are summarized in table 3.2. In particular, the initial density of electrons and positive ions is set to 10^{11} m^{-3}. In the simulations the same applied voltage is used as in the experiments, as shown in figure 3.2. The voltage increases from 10% to 90% of its full amplitude (15 kV) in about 52 ns, so that the voltage rise time from zero to full amplitude is about 65 ns.

3.2.3 Processing of emitted light

Experimentally, the streamer morphology is captured with an ICCD camera. To quantitatively compare the simulated streamers with experiments, it is important to accurately model the light emission from the discharge, and to process it in the same way for both the experiments and simulations.

As already mentioned above, the $N_2(C^3\Pi_u \rightarrow B^3\Pi_g)$ transition is responsible for most of the optical emission under our discharge conditions [144]. Therefore the number of photons emitted at any given time is approximately proportional to the $N_2(C^3\Pi_u)$ density, which is included in the discharge model, see table 3.1. Experimentally, we get a good approximation of the instantaneous light emission by using a short camera gate time of 900 ps. As shown in section 3.3, typical streamer velocities under the present conditions are on the order of 0.5 to 1 mm/ns, which means that the streamers move less than a mm during the camera gate time.

To compare the light from axisymmetric simulations with experimental observations, we have to apply a forward Abel transform. For this purpose, the $N_2(C^3\Pi_u)$ density in the region $0 \leq r \leq 15$ mm by $0 \leq z \leq 90$ mm (from the grounded electrode to the needle electrode tip) is first stored on a uniform grid, with a resolution $\delta r = 0.01$ mm and $\delta z = 0.05$ mm. The Hansen–Law method [147] is used for the forward Abel transformation. The experimental pictures are

cropped to the same region, so that the light from the simulations and experiments is described by profiles $I(x, z)$, where $z \in [0, 90]$ mm is the propagation direction and $x \in [-15, 15]$ mm is the direction perpendicular to it.

To directly compare streamer front positions, velocities and radii between experiments and simulations, we determine these properties based on the emitted light. The procedure is illustrated in figure 3.3. To obtain the streamer's front position, we first compute

$$I_z(z) = \int_{-15\,\mathrm{mm}}^{15\,\mathrm{mm}} I(x, z) dx.$$

The front position is then determined as the minimum z coordinate where $I_z(z)$ exceeds half of its maximum. Streamer velocities are determined by taking the numerical time derivative of these z coordinates for consecutive images. For the radius we follow a similar approach, first computing

$$I_x(x) = \int_{0}^{z_{\mathrm{ub}}} I(x, z) dz.$$

The upper bound z_{ub} is used to exclude strong emission around the tip of the needle electrode. $I_x(x)$ therefore mostly consists of light emitted close to the streamer head. The streamer optical radius is then defined as the FWHM (full width at half maximum) of $I_x(x)$. A similar definition has been used in earlier work, e.g. [7].

3.3 Comparison of emission profiles and streamer properties

Figure 3.4 shows the experimental and simulated light emission profile from 6 ns to the last frame captured, together with the simulated electric field and electron density. There is good qualitative agreement between the emission profiles, although the experimental streamer has a higher velocity and a larger radius. In both the experimental and simulation figures the streamers' characteristic head shape is visible. The front of the streamer heads is always the brightest, a bit like a crescent moon, which is followed by a darker tail due to the decay of the emitting $N_2(C^3\Pi_u)$ molecules. The streamers grow wider as they propagate down, but when they approach the grounded electrode they accelerate, their radius reduces and their heads become even brighter. At the same time, the electric field and the electron density at the streamer head also increase.

Figure 3.5 shows the integrated light emission profile I_z for the experimental and simulated streamers in figure 3.4. When compared at the same length, most of the curves look similar. However, at the final time the amplitude of the simulated light emission is significantly larger. Another difference is that the tail of the emitted light is narrower in the simulations.
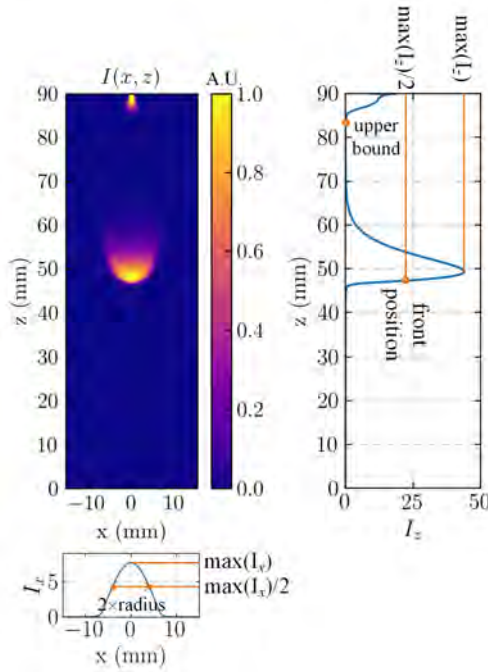
Figure 3.3: Illustration showing how the streamer front position and radius are determined from the light emission profile. The z axis shows the 90 mm between the tip of the (10 mm long) needle electrode and the grounded plate electrode.

Figure 3.6 shows the streamer velocity and radius versus the streamer length. Experimentally, each measurement is obtained from a new discharge, which leads to some fluctuations in the streamer properties. These fluctuations are smoothed by a second order Savitzky–Golay filter with a window size of nine [148].

Qualitatively, the agreement in the streamer velocity profile is quite good. After inception, the streamers first accelerate and then they slowly decelerate. Afterwards, they obtain an approximately stable velocity, and finally they accelerate again when they approach the opposite electrode. All these phases are present in both the experimental and simulation data, although the times and streamer lengths at which they occur are somewhat different. The maximal electric field at the streamer head follows a similar trend as the streamer velocity, as can be seen in figure 3.4. The deceleration of the streamers in the middle of the gap is related to the size of the plate electrodes, as discussed in detail in section 3.4.8. There is also good qualitative agreement in the streamer radius between simulations and experiments. The radius initially increases until the streamers are about 50 mm long, and then it decreases when the streamers approach the opposite electrode.

Quantitatively, figure 3.6 shows that the simulated streamer velocity is about 20% to 30% lower when compared at the same streamer length, and the simulated
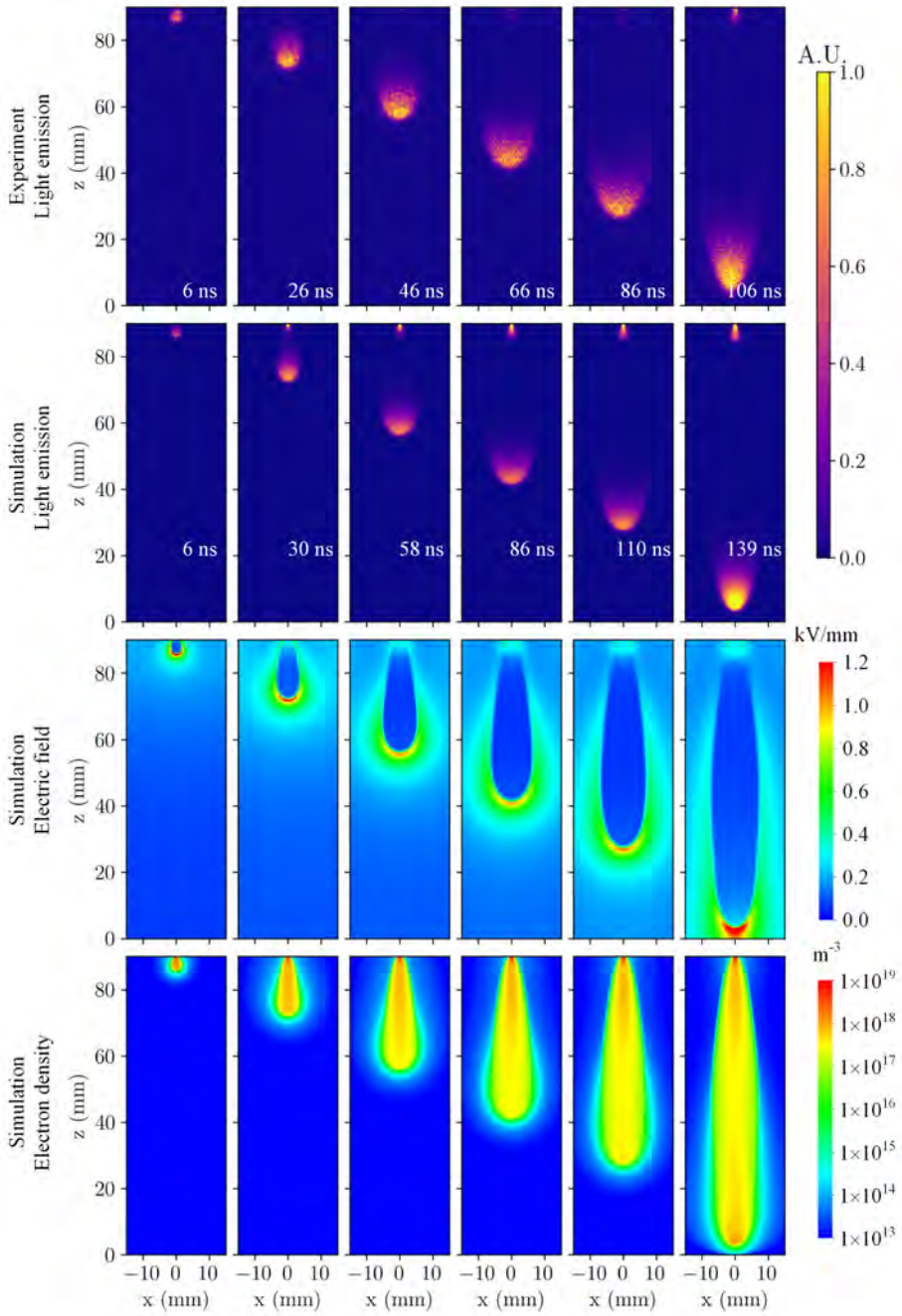
Figure 3.4: From top to bottom: the light emission profile of experiments (camera gate time 900 ps), the simulated instantaneous light emission profile, the simulated electric field and electron density. The moment when the streamer length just exceeds 2 mm is taken as 0 ns. For light emission the data was normalized <u>per row</u> to arbitrary units, so that frame-to-frame brightness variations are conserved. This was done by dividing by the value at their 0.999^{th} quantile, and limiting the result to the range [0, 1]. This ensures that a few bright pixels do not affect the brightness of the streamer head.
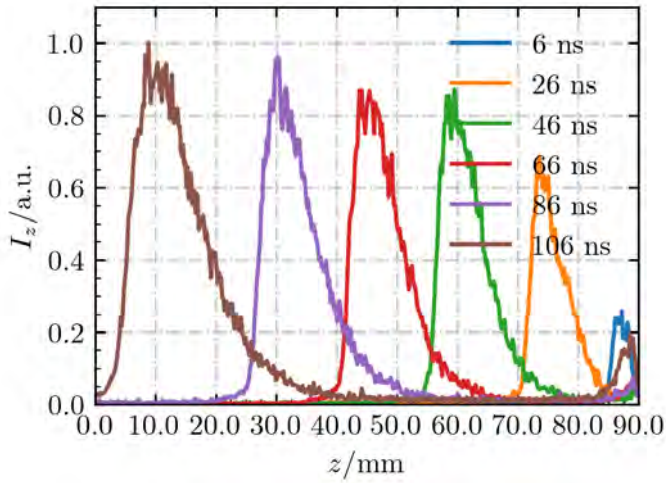
(a) Experimental results
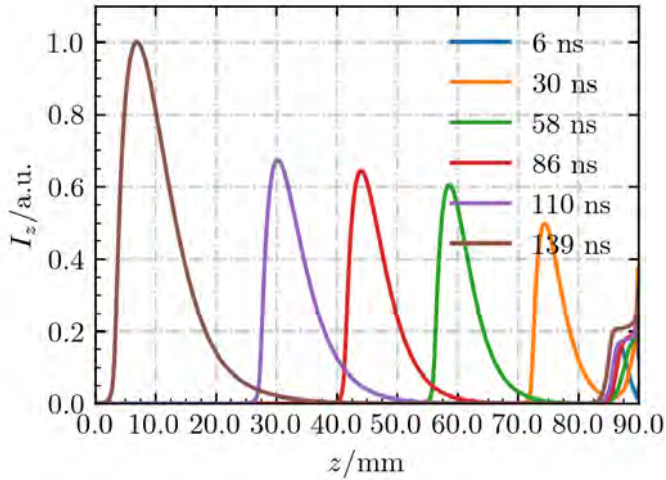
(b) Simulation results

Figure 3.5: The integrated light emission profile I_z for the experimental and simulated streamers in figure 3.4. In each sub-figure the data was normalized to a maximal amplitude of one.

radius is about 1 - 1.2 mm smaller (also 20% to 30%). These discrepancies could well be correlated, as earlier studies [7, 19, 52] have found that the streamer velocity increases with the streamer radius. On the other hand, the observed streamer velocities do not increase with the radius for streamer lengths between 15 mm and 40 mm because the streamer's maximal field in this region decreases.

Going back to figure 3.4, there is one detail in which the experimental and
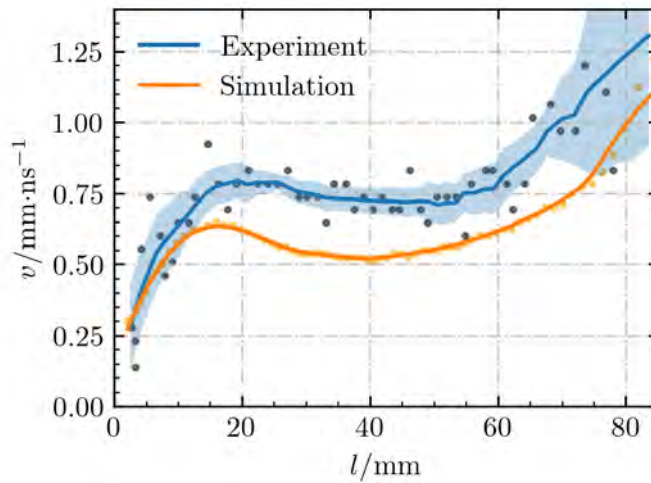
(a) Streamer velocity versus streamer length
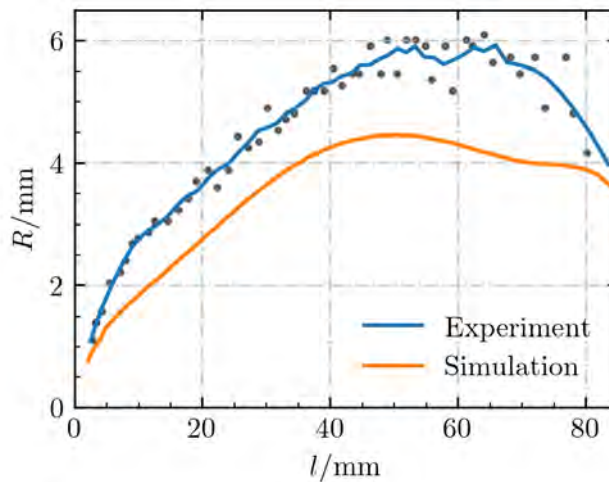
(b) Streamer radius versus streamer length

Figure 3.6: Comparison of streamer propagation parameters between experiments and simulations. The dots indicate unsmoothed data. The blue filled area shows the standard deviation between the unsmoothed and smoothed experimental velocity.

simulation results disagree: the emitted light near the electrode tip. In the simulations, a bright spot is always visible, whereas in the experiments this only happens occasionally. This could be related to the width of the streamer channel connected to the needle electrode, since a narrower connection means that a higher field and a higher electron density are required to carry the discharge

current, leading to more light emission. These effects are visible in figure 3.4, in which the electric field in this region is about $0.3\,\mathrm{kV/mm}$ and the electron density is about $1 \times 10^{19}\,\mathrm{m^{-3}}$.

As discussed in section 3.4.4, discharge inception is sometimes not accurately described by a fluid model because the continuum approximation breaks down when there are few particles. This could affect the connection of the discharge to the electrode, and thereby also the light emission around this area. Furthermore, the voltage rise time also affects the brightness of this area, see section 3.4.7.

3.4   Investigating possible sources of discrepancy

The results in section 3.3 showed good qualitative agreement between the simulations and experiments. However, the simulated streamer velocity was 20% to 30% slower, and the streamer radius was about 1 - 1.2 mm (20% - 30%) smaller, when compared at the same streamer length. In this section, we investigate how several simulation and discharge parameters affect these quantitative differences. Below we only mention the parameters that are changed, all other parameters are set according to table 3.2.

3.4.1   Numerical convergence

Model verification means checking whether the model's equations are solved correctly and with sufficient numerical accuracy, which is an important step towards the development of validated models. In an earlier study [37] the `Afivo-streamer` code was compared against five other codes for this purpose. It was found that with sufficiently fine grids and small time steps different codes could produce highly similar results, indicating numerical convergence. Below, we again test the numerical convergence of our model for the present discharge simulations.

For computational efficiency, `Afivo-streamer` uses adaptive mesh refinement (AMR). The refinement criterion has been introduced in section 2.6. We test how the refine parameter c_0 in equation (2.14) affects the simulation results. Here c_1 is set to 1. Figure 3.7 shows the streamer velocity versus the streamer length for c_0 set to 2, 1, 0.5 and 0.2 and $d_0 = 0.2\,\mathrm{mm}$. These parameters lead to a corresponding minimal grid spacing of 24.4, 12.2, 6.1 and $3.1\,\mu\mathrm{m}$. With $c_0 = 2$ the grid is clearly too coarse and the streamer is much slower than for the other cases. With $c_0 = 1$ the results are similar to those on even finer grids, but the streamer is a bit slower in the later stages. For $c_0 = 0.5$ and $c_0 = 0.2$, the streamer propagation is almost identical, indicating that the model is close to numerical convergence. For the results presented in this chapter, we therefore use $c_0 = 0.5$ ($\Delta x_{\min} = 6.1\,\mu\mathrm{m}$). Additionally, we also compared the effect of the parameter d_0, which controls the derefinement of the mesh. However, reducing d_0 to $10\,\mu\mathrm{m}$ hardly affected the results, so we use $d_0 = 0.2\,\mathrm{mm}$.

For the case with $c_0 = 0.5$, the average time step for the streamer bridging the gap was $\Delta t = 0.44$ ps. Such a small time step was required due to a high electron density of about 10^{20} cm^{-3} occurring near the tip of the needle electrode. Typical cases took about 9 to 10 hours on a node with 24 Intel Xeon E5-2695 v2 @ 2.4 GHz cores.
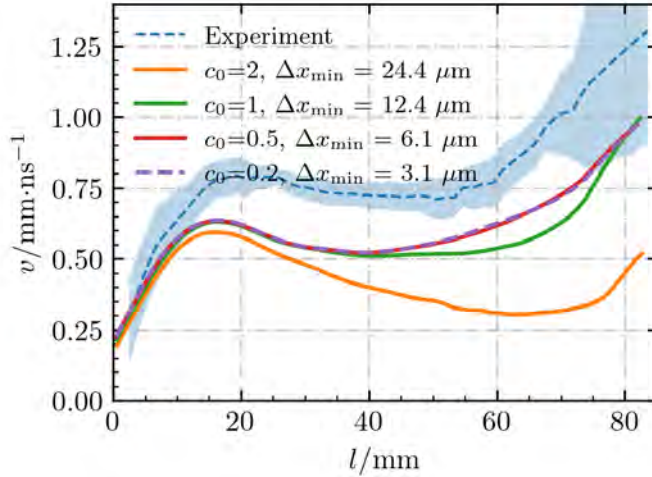

Figure 3.7: The streamer velocity versus the streamer length for streamers with different values for c_0 in the refinement criterion $\Delta x < c_0/\alpha(E)$

3.4.2 Effect of chemical reactions

The chemical reactions considered in a fluid simulation can be as extensive as in [30], with hundreds of reactions, or as simple as in [37], considering only effective ionization rates. Nine reactions are considered as the default in this chapter, including three ionization reactions, two attachment reactions and four reactions related to light emission, as shown in table 3.1. To make clear how important different reactions are in our discharge regime, three other cases are investigated:

- Case 1: reactions 1-3 and 6-9 from table 3.1; ionization reactions and reactions related to light emission.

- Case 2: all the reactions from table 3.1 and reactions 10-11 from table 3.3; adding two detachment reactions.

- Case 3: all the reactions from tables 3.1 and 3.3; adding two negative ion conversion reactions (reactions 12-13), three positive ion conversion reactions (reactions 14-16), one electron-ion recombination reaction (reaction 17) and twelve ion-ion recombination reactions (reactions 18-29).

Table 3.3: Additional chemical reactions. The effects of these reactions are studied in section 3.4.2, see figure 3.8. Label "u.s." stands for species which are not tracked in our simulation. T_e in reaction rate k_{17} is obtained from the mean electron energy (ϵ_e) computed by BOLSIG+ as $T_e = 2\epsilon_e/3k_B$. Reaction coefficients k_{10} - k_{13} are from reference [149], k_{14} - k_{16} from [150] and k_{17} - k_{29} from [113].

No.	Reaction	Reaction rate coefficient
10	$O_2^- + M \xrightarrow{k_{10}} e + O_2 + M$	$k_{10} = 1.24 \times 10^{-17} \exp(-(\frac{179}{8.8+E/N})^2)\, \mathrm{m^3 s^{-1}}$
11	$O^- + N_2 \xrightarrow{k_{11}} e + N_2O$	$k_{11} = 1.16 \times 10^{-18} \exp(-(\frac{48.9}{11+E/N})^2)\, \mathrm{m^3 s^{-1}}$
12	$O^- + O_2 \xrightarrow{k_{12}} O_2^- + O$	$k_{12} = 6.96 \times 10^{-17} \exp(-(\frac{198}{5.6+E/N})^2)\, \mathrm{m^3 s^{-1}}$
13	$O^- + O_2 + M \xrightarrow{k_{13}} O_3^- + M$	$k_{13} = 1.1 \times 10^{-42} \exp(-(\frac{E/N}{65})^2)\, \mathrm{m^3 s^{-1}}$
14	$N_2^+ + N_2 + M \xrightarrow{k_{14}} N_4^+ + M$	$k_{14} = 5 \times 10^{-41}\, \mathrm{m^6 s^{-1}}$
15	$N_4^+ + O_2 \xrightarrow{k_{15}} O_2^+ + N_2 + N_2$	$k_{15} = 2.5 \times 10^{-16}\, \mathrm{m^3 s^{-1}}$
16	$O_2^+ + O_2 + M \xrightarrow{k_{16}} O_4^+ + M$	$k_{16} = 2.4 \times 10^{-42}\, \mathrm{m^6 s^{-1}}$
17	$e + O_4^+ \xrightarrow{k_{17}} O_2 + O_2$	$k_{17}(E/N) = 1.4 \times 10^{-12}(300\mathrm{K}/T_e)^{1/2}\, \mathrm{m^3 s^{-1}}$
18	$N_2^+ + O^- \xrightarrow{k_{18}} \mathrm{u.s.}$	$k_{18} = 10^{-13}\, \mathrm{m^3 s^{-1}}$
19	$N_2^+ + O_3^- \xrightarrow{k_{19}} \mathrm{u.s.}$	$k_{19} = 10^{-13}\, \mathrm{m^3 s^{-1}}$
20	$N_2^+ + O_2^- \xrightarrow{k_{20}} \mathrm{u.s.}$	$k_{20} = 10^{-13}\, \mathrm{m^3 s^{-1}}$
21	$O_2^+ + O^- \xrightarrow{k_{21}} \mathrm{u.s.}$	$k_{21} = 10^{-13}\, \mathrm{m^3 s^{-1}}$
22	$O_2^+ + O_3^- \xrightarrow{k_{22}} \mathrm{u.s.}$	$k_{22} = 10^{-13}\, \mathrm{m^3 s^{-1}}$
23	$O_2^+ + O_2^- \xrightarrow{k_{23}} \mathrm{u.s.}$	$k_{23} = 10^{-13}\, \mathrm{m^3 s^{-1}}$
24	$O_4^+ + O^- \xrightarrow{k_{24}} \mathrm{u.s.}$	$k_{24} = 10^{-13}\, \mathrm{m^3 s^{-1}}$
25	$O_4^+ + O_2^- \xrightarrow{k_{25}} \mathrm{u.s.}$	$k_{25} = 10^{-13}\, \mathrm{m^3 s^{-1}}$
26	$O_4^+ + O_3^- \xrightarrow{k_{26}} \mathrm{u.s.}$	$k_{26} = 10^{-13}\, \mathrm{m^3 s^{-1}}$
27	$N_4^+ + O^- \xrightarrow{k_{27}} \mathrm{u.s.}$	$k_{27} = 10^{-13}\, \mathrm{m^3 s^{-1}}$
28	$N_4^+ + O_2^- \xrightarrow{k_{28}} \mathrm{u.s.}$	$k_{28} = 10^{-13}\, \mathrm{m^3 s^{-1}}$
29	$N_4^+ + O_3^- \xrightarrow{k_{29}} \mathrm{u.s.}$	$k_{29} = 10^{-13}\, \mathrm{m^3 s^{-1}}$

Figure 3.8 shows the streamer velocity versus the streamer length for the above three cases together with the default case. The results of all cases are similar. Note in particular how the inclusion of attachment and detachment reactions hardly makes a difference. The streamer is slightly slower for case 3, in which recombination is included, but this difference is much smaller than that between the experiment and the default case. We therefore conclude that ionization reactions dominate the propagation of our discharge – a streamer of

10^2 ns time scale at $0.1\,\text{bar}$ with a background electric field of about $1.5\,\text{kV/cm}$. Under these conditions, attachment, detachment and recombination appear to be less important for streamer propagation.
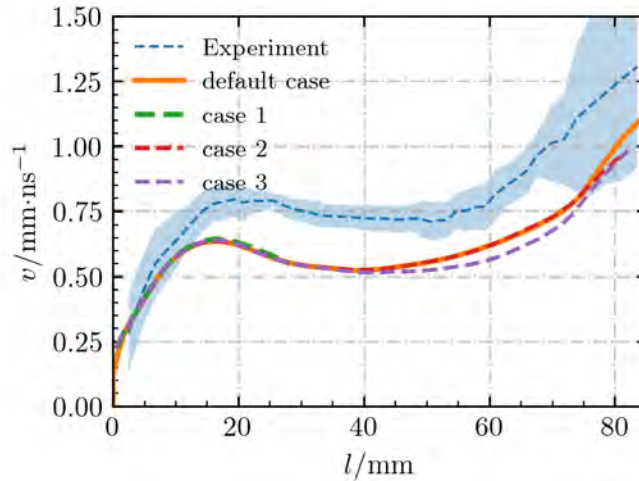

Figure 3.8: The streamer velocity versus the streamer length for streamers with different chemical reactions. The default case uses all the reactions from table 3.1; case 1, 2 and 3 are described in section 3.4.2.

3.4.3 Transport data source

Transport coefficients for fluid models can be computed from electron-neutral cross sections using two-term or multi-term Boltzmann solvers [116–118] or Monte Carlo swarm simulations [119, 120]. For N_2 and O_2, there are several sets of cross sections available at LXCAT [121, 122]. We here consider five such sets, namely those by Phelps [115, 123], IST Lisbon [124–126], Morgan [127], TRINITI [128] and Biagi [119, 129]. It has been common practice to normalize and adjust the total cross sections so that the transport coefficients computed with a Boltzmann solver agree well with experimentally measured swarm data with isotropic scattering. For e.g. Phelps' cross sections, this was done with a two-term method, whereas for Biagi's cross sections a Monte Carlo method was used. This means that even though multi-term and Monte Carlo methods are generally more accurate than two-term approaches, they do not necessarily produce transport coefficients that are closer to experimental data. In this section, we investigate how different sets of cross sections and different Boltzmann solvers affect transport coefficients and the agreement between our simulations and experiments.

We first used BOLSIG+ [116] (a two-term Boltzmann solver) to calculate transport coefficients in 80% N_2 and 20% O_2 for the Phelps, IST Lisbon, Morgan, TRINITI and Biagi cross sections. We used the online version BOLSIG+

via lxcat.net. Figure 3.9 shows how the streamer velocity in our simulations is affected by the resulting transport coefficients, which are shown in figure 3.10. The streamers with the Phelps and IST Lisbon databases are the fastest. With Morgan and TRINITI data, the streamers are similar to those with Phelps data up to a length of 50 mm, but thereafter they behave more like those with Biagi data. The streamer with the Biagi database is the slowest, and it is about 10% slower (at the same streamer length) than the fastest one. However, regardless of the cross sections used, all simulated velocities are significantly slower than the experimental one.
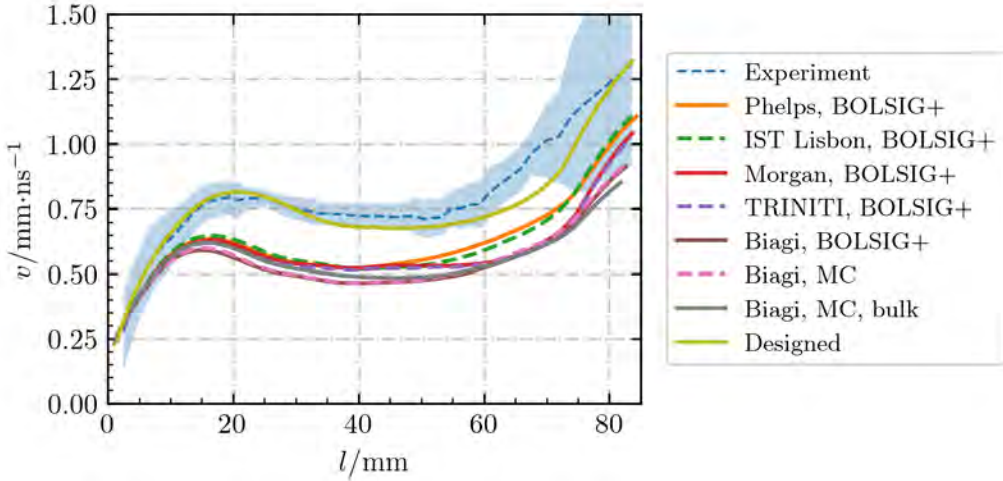

Figure 3.9: The streamer velocity versus the streamer length for simulations with different transport coefficients. The labels "Phelps", "IST Lisbon", "Morgan", "TRINITI" and "Biagi" indicate cross section databases, "BOLSIG+" and "MC" indicate the use of BOLSIG+ or a Monte Carlo Boltzmann solver, and "bulk" means that so-called bulk coefficients were used instead of flux coefficients. "Designed" is based on the "Phelps, BOLSIG+" database by increasing the ionization coefficient α and the mobility μ each with 20%.

To investigate the influence of the type of Boltzmann solver we also computed transport data from Biagi's cross sections with a Monte Carlo code (available at gitlab.com/MD-CWI-NL/particle_swarm), which is similar to e.g. [120]. The resulting transport data is shown in figure 3.10. With the Monte Carlo method, we computed both bulk and flux transport coefficients. Bulk coefficients describe average properties of a group of electrons, taking ionization and attachment into account, whereas flux properties are averages for 'individual' electrons [36, 151]. The bulk mobility is larger than the flux one at high E/N because electrons that move faster than average also typically have higher energy, and hence produce more ionization. The resulting streamer velocity with such Monte Carlo swarm

flux and bulk data is shown in figure 3.9. It can be seen that the choice of cross sections, Boltzmann solver and flux/bulk coefficients does not significantly affect the streamer velocity, at least not sufficiently to explain the observed discrepancy with the experimental results.

To match the experimental results, artificial transport coefficients were designed based on the Phelps database by increasing the ionization coefficient α and the mobility μ each with 20%. Figure 3.9 shows that with these coefficients the relative error is often below 7% when compared to the experimental velocity at the same length.
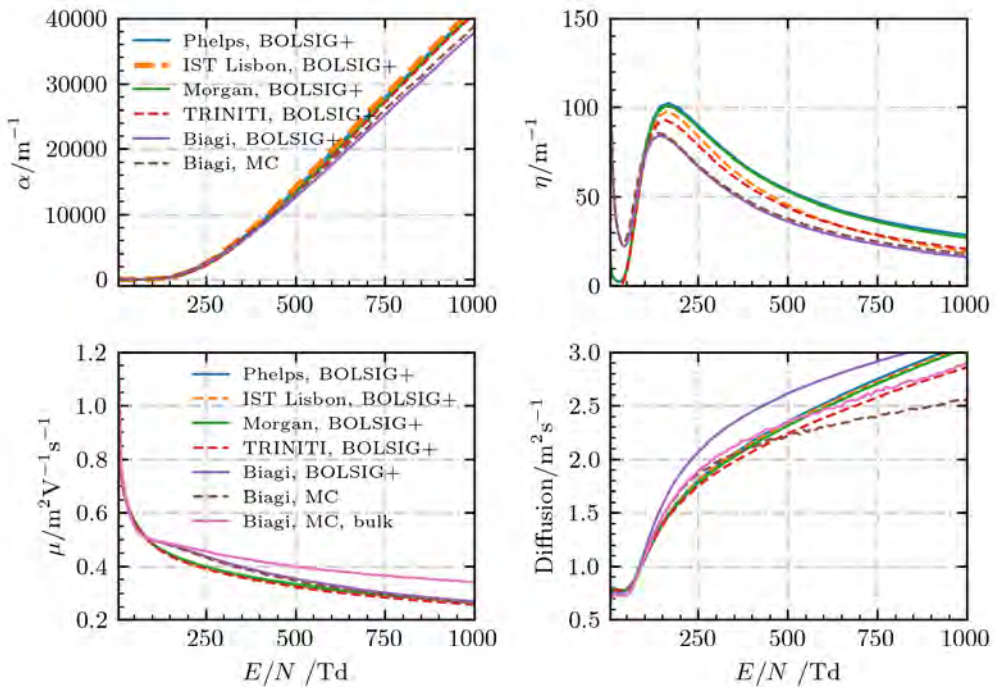

Figure 3.10: Transport coefficients (α, η, μ and Diffusion) as determined from several sets of cross sections and different Boltzmann solvers. The same labels are used as in figure 3.9.

3.4.4 Effect of background ionization density

Positive streamers require free electrons ahead of them for their propagation, which can for example be provided by photoionization or background ionization. Under the conditions considered here (air at 0.1 bar, 50 Hz repetition frequency), we generally expect photoionization to be the dominant source of free electrons. However, background ionization could play an important role in discharge inception [141]. To investigate this, we have performed simulations with homogeneous

background ionization densities of 10^3, 10^{11}, 10^{13} and $10^{15}\,\mathrm{m}^{-3}$, in the form of electrons and positive ions. Photoionization was always included.

Note that a background ionization degree of $10^3\,\mathrm{m}^{-3}$ corresponds to one electron per $(10\,\mathrm{cm})^3$. In reality, having so few electrons would mean that inception would be unlikely within a $200\,\mathrm{ns}$ voltage pulse. Only electrons close to the electrode tip could start a discharge, since those farther away would quickly attach to oxygen molecules. However, in a fluid model electrons are stored as densities which can lead to unrealistic streamer inception: an electron density in the zone above breakdown can represent a fraction of an electron, but it still can grow and rapidly start a discharge. Clearly, the continuum approximation of the fluid model breaks down in these cases. We nevertheless include this unrealistic case for demonstrative purposes.

Figure 3.11 shows that background ionization densities in the range of 10^3 to $10^{13}\,\mathrm{m}^{-3}$ have little effect on the streamer velocity versus streamer length. With a lower background ionization degree the streamer starts a bit later, but there is no significant change in the velocity. An even higher background ionization density of $10^{15}\,\mathrm{m}^{-3}$ (corresponding to $10^{17}\,\mathrm{m}^{-3}$ at $1\,\mathrm{bar}$) does lead to a significantly slower streamer. With this much background ionization the air surrounding the discharge has a non-negligible conductivity, reducing the field enhancement of the streamer. Since expected background ionization levels under the conditions studied here are much lower, background ionization will probably not significantly affect the streamer velocity.

The cases discussed above included spatially uniform background ionization. To study the effect of more localized initial ionization, we have also performed simulations with a Gaussian initial seed located close to the tip of the needle electrode. A neutral seed consisting of electrons and positive ions was used, given by $n_0 \exp(-(d/R)^2)$, with $n_0 = 10^{14}\,\mathrm{m}^{-3}$, d the distance to the needle tip at $(r,z) = (0\,\mathrm{mm},\ 90\,\mathrm{mm})$ and $R = 5\,\mathrm{mm}$. Besides this initial seed, no other (uniform) initial ionization was included. The resulting streamer velocity is shown in figure 3.11. The streamer velocity is almost the same as for the cases with a uniform background density of up to $10^{13}\,\mathrm{m}^{-3}$.

Remnants from previous pulses may affect the next streamer, in particular O_2^- ions from which electrons can detach. We therefore include a case with a $10^{14}\,\mathrm{m}^{-3}$ background density of positive (N_2^+) and negative ions (O_2^-) (see Fig. 2 of [152]) and with two detachment reactions (reaction 10 and 11 from table 3.3). The resulting streamer velocity versus length is similar to other cases with a background density of electrons and positive ions, as shown in figure 3.11.

We conclude that some type of initial or background ionization is important for streamer inception, but that the stochastic nature of inception cannot be studied by a fluid model. The streamer propagation at later times is hardly affected by background ionization, at least under our conditions (air at $0.1\,\mathrm{bar}$), consistent with [141, 142].
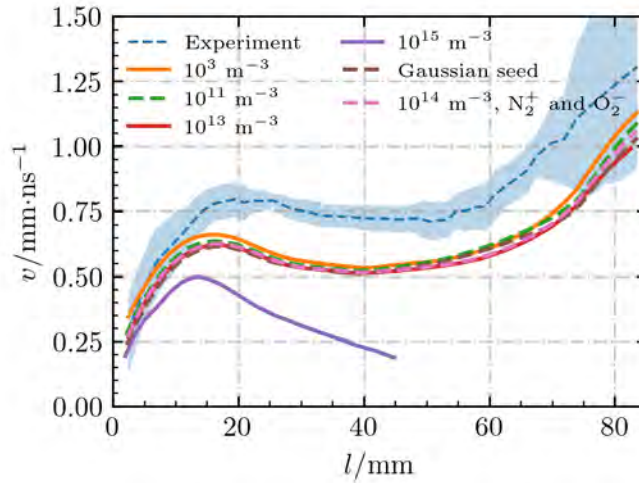
Figure 3.11: Streamer velocity versus streamer length for streamers with different uniform background ionization densities and a Gaussian initial seed. The curve labeled "$10^{14}\,\mathrm{m}^{-3}$, N_2^+ and O_2^-" has a background ionization of $10^{14}\,\mathrm{m}^{-3}$ N_2^+ and O_2^-. For the other curves the background species are electrons and N_2^+. In the rest of the chapter, a uniform background ionization of $10^{11}\,\mathrm{m}^{-3}$ electrons and N_2^+ is used.

3.4.5   Effect of the photoionization

As mentioned above, we expect photoionization to be the dominant source of free electrons ahead of the positive streamers studied here. We now investigate how sensitive streamer propagation is to the amount of photoionization and to the specific photoionization model that is used.

   The 'standard' photoionization model we use is a Helmholtz approximation to Zheleznyak's model, as introduced in section 3.2.2. With this model, we study the effect of the amount of photoionization by changing the proportionality factor ξ in equation (2.13). Four cases are considered: $\xi = 0.075$, as is used in the rest of this chapter - this value is taken from [89] considering the electric field at our streamer head - and $\xi = 0.05, 0.0075$ and 0.75.

   As mentioned in [38], photoionization can also be modeled with a discrete Monte Carlo approach instead of the continuum Helmholtz approach. We investigate how the streamer velocity is affected by these different approaches. The Monte Carlo photoionization model used here is the same as the one used in section 3.2 of [38] and ξ is set to 0.075. We call this approach "PI model 2" (with PI standing for photoionization).

   In Zheleznyak's model the generation of ionizing photons is proportional to the number of impact ionization events, with a proportionality factor ξ. Ionizing photons can instead also be directly generated based on the densities of certain

excited species, as was shown in [153, 154]. We study how such a photoionization model based on excited species affects the streamer velocity, by comparing it with the commonly used Zheleznyak's model. We call this approach "PI model 3". We generate photons according to the density of $c_4'\Sigma_u^+$ state of N_2 [153]. The reaction coefficients describing the production of this state are calculated by BOLSIG+ with cross sections from Biagi database [129]. The radiation lifetime τ used for the $c_4'\Sigma_u^+$ state is 0.9 ns [154]. Therefore, the source of ionizing photons $I(r)$ in a time step Δt is calculated as

$$I(r) = N_r \frac{p_q}{p + p_q}(1 - e^{-\Delta t/\tau})/\Delta t, \tag{3.1}$$

where N_r is the density of the $c_4'\Sigma_u^+$ state. A quenching pressure p_q of 40 mbar is used, which is consistent with the 'standard' model. A Helmholtz approach is used to solve S_{ph}, which is also the same as the 'standard' model.

Figure 3.12 shows the streamer velocity versus streamer length for the above-mentioned six cases, using a uniform background density of $10^{11}\,\mathrm{m^{-3}}$. With ten times less photoionization, the streamer velocity increases at later times, approaching the experimental streamer velocity. This behavior, which at first seems surprising, shows the nonlinear nature of streamer discharges. Less photoionization leads to sharper electron density gradients at the streamer head, a smaller radius, and a higher degree of ionization, which can result in a higher electric field and a higher streamer velocity. However, note that there is still a qualitative discrepancy between the results of this case ($\xi = 0.0075$) and the experimental velocity in the range of 15 mm $< l <$ 50 mm. With ten times more photoionization, the streamer is significantly slower. The electron density around the streamer head then increases sufficiently to reduce its field enhancement, as also happened in section 3.4.4 with a high background ionization density of $10^{15}\,\mathrm{m^{-3}}$. However, if the amount of photoionization is only slightly changed using $\xi = 0.05$ (the smallest tabulated value in [89]), the streamer velocity is hardly affected, as shown in figure 3.12.

Photoionization models 2 and 3 lead to similar results as Zheleznyak's model with a Helmholtz approximation, though the streamer velocity with PI model 3 is a bit lower for 50 mm $< l <$ 70 mm.

Additionally, we have also repeated the above simulations with an even lower background ionization density, but the results were almost identical. This indicates that even if photoionization is reduced by a factor of ten, it still dominates over a background density of $10^{11}\,\mathrm{m^{-3}}$. Finally, note that all results were obtained at a pressure of 0.1 bar, at which there is less quenching than at 1 bar, see section 3.2.2.

3.4.6 Effect of gas temperature

In our experiments the lab temperature was about 293 K, but the gas temperature in the vessel was not directly measured, and we have thus far assumed
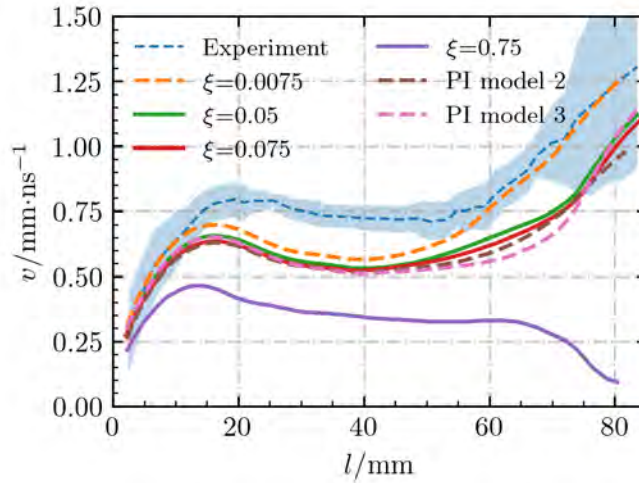
Figure 3.12: The streamer velocity versus the streamer length for streamers with different amounts of photoionization and different photoionization models. The value of ξ used in the rest of the chapter is 0.075. If not indicated otherwise, Zheleznyak's model with a Helmholtz approximation is used. Details about PI models 2 and 3 are described in section 3.4.5.

it to be 300 K. The two main factors affecting the gas temperature in the vessel are heating due to repetitive discharges and cooling due to the expansion of the compressed artificial air flowing into the vessel. To investigate the effect of temperature variations, we have performed simulations with gas temperatures of 290 K, 300 K, 310 K and 360 K. The gas pressure is always 0.1 bar in the simulations. Figure 3.13 shows the streamer velocity for these four cases, together with the experimental result. The average streamer velocity between the two electrodes is 0.58, 0.59, 0.60 and 0.69 mm/ns for the cases at 290 K, 300 K, 310 K and 360 K, respectively. For a 10 K change in the gas temperature, the change in the streamer velocity at the same length is about 3%, on average. When the gas temperature increases 20% to 360 K, the simulated streamer velocity is closer to the experimental data, and the velocity error at the same length is less than 15%.

That a higher gas temperature leads to a higher streamer velocity is to be expected, because it leads to a higher value of E/N in the discharge gap, just as when the applied voltage is increased. In our model, the gas number density is computed using the ideal gas law, so a reduction in gas pressure has a similar effect as an increase in temperature. However, the gas pressure was controlled to be 0.1 bar in the experiments, with an uncertainty of about 1%, so a change in pressure cannot account for the observed discrepancies.

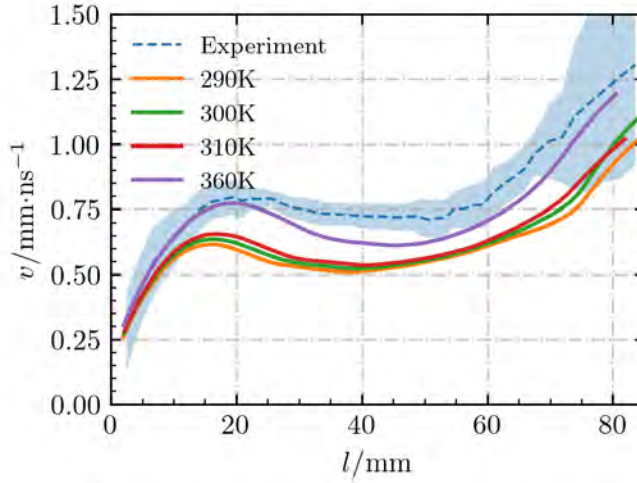We can roughly estimate the temperature increase caused by the repetitive

Figure 3.13: The streamer velocity versus the streamer length at different gas temperatures. In the rest of this chapter, a gas temperature of 300 K is used.

discharges. From the voltage-current waveform, we estimate that about 2 mJ is deposited in the plasma per 200 ns pulse. At 50 Hz repetition frequency, this corresponds to $P = 0.1$ W of heating power. The gas flush rate in the experiments was $f = 2$ SLM $\approx 2 \times 10^1$ L/min. Dry air at 0.1 bar and 300 K has a specific heat capacity $C_p = 1.0$ kJ/(kg K), a density $\rho = 0.12$ kg/m^3 and a thermal diffusivity $\alpha = 2.2 \times 10^{-4}$ m^2/s. If we assume heating happens uniformly and neglect losses to the vessel walls, then a rough estimate for the temperature increase would be $\Delta T = P/(C_p \rho f) \approx 2$ K. Alternatively, we could assume that heat is predominantly produced in the axial streamer channel and that heat diffusion occurs only in the radial direction. This results in an 'effective' volume of order $\pi \alpha h t$, where $h = 10$ cm is the gap size and t the time. The temperature increase in this volume can then be estimated as $\Delta T = P/(C_p \rho \pi \alpha h) \approx 1 \times 10^1$ K. This is a rough estimate, not accounting for e.g., wall losses or the actual flow pattern in the vessel, nor the fact that the temperature close to the center could be considerably higher. We only have preliminary experimental data on the temperature increase, obtained with Raman scattering and optical emission spectroscopy. These measurements indicated a ΔT in the range of 10^1 K to 10^2 K, consistent with the estimate given above. We therefore conclude that gas heating might explain part of the observed differences between simulations and experiments.

3.4.7 Effect of applied voltage

The uncertainty in the measured applied voltage is only about 2%, which is unlikely to account for the observed discrepancies in streamer velocity. However, out of scientific curiosity, we nevertheless investigate the effects of the

voltage amplitude and rise time on streamer propagation below. Figure 3.14 shows the streamer velocity in simulations at 12.5 kV, 15 kV and 17.5 kV, together with experimental data at 12.5 kV and 15 kV. Note that for the curve labeled "Simulation-15kV-actual voltage", the voltage is applied according to the actual waveform used in the experiment, as shown in figure 3.2. For the other cases, the applied voltage rises linearly from zero to the maximum voltage within 65 ns, after which it is constant. The streamer evolution is similar for the cases with an actual voltage waveform and the linearly-rising 15 kV voltage waveform, but the streamer is a little bit faster with the actual waveform, since it has a slight overshoot. In all cases, the velocity profiles follow the same pattern: the velocity first increases, then it decreases slightly, and finally it increases again as the streamers approach the opposite electrode. As expected, streamer velocities increase for higher applied voltages. The simulated streamers are always slower than the experimental ones at the same applied voltage. On average, the velocity in a simulation at 17.5 kV agrees quite well with the experimental velocity at 15 kV. However, since the experimental uncertainty in the voltage is only about 2%, this cannot explain the observed discrepancies.
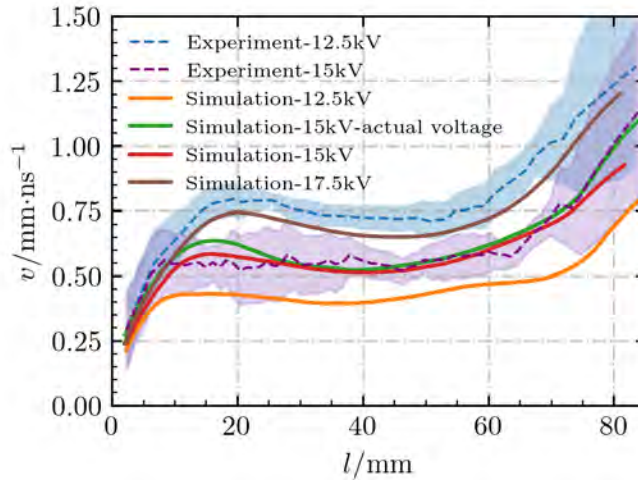

Figure 3.14: Streamer velocity versus streamer length in simulations and experiments at different applied voltages. Note that the experimental results at 12.5 kV show larger fluctuations than those at 15 kV. This happens because each frame is taken from a new streamer, and discharge inception at lower voltages is more stochastic.

We have also studied the effect of the voltage rise time on streamer propagation, using an applied voltage of 15 kV and a variable linear voltage rise. Figure 3.15 shows the streamer velocity and streamer radius versus the streamer length for voltage rise times of 0, 20, 40 and 65 ns. The streamer with 0 ns rise

time starts immediately when the simulation begins. Inception, here identified by a reduction in the maximal electric field, takes longer with a longer voltage rise time. With a rise time of 20 ns, 40 ns and 65 ns, the streamers incept at 10 ns, 20 ns and 30 ns, respectively. With a shorter rise time, the streamer velocity is initially higher. As the streamers get longer they propagate at the applied voltage and velocity differences become smaller when compared at the same length. Because the voltage rise time has an effect on the conductivity of the initial part of the streamer channel, small differences in velocity remain, with slightly higher velocities for shorter rise times. When comparing the velocity at the same streamer length ($30\,\text{mm} < l < 80\,\text{mm}$), the streamer velocity (averaged over length) of the 0 ns rise time case increases by about 10% compared to the 65 ns case. But there is still about a 20% discrepancy compared to the experiments. That a faster voltage rise leads to a higher streamer velocity was also found in [21]. As in [21], we also observe a larger streamer radius with a shorter voltage rise time, see figure 3.15 (b).

A related effect is that with a shorter voltage rise time, the electric field initially exceeds the breakdown threshold in a larger area around the needle electrode. This leads to a wider and more conductive streamer channel connected to the electrode. At later discharge stages the internal electric field in this part of the channel can therefore be lower while carrying the same electric current, which leads to less light emission around the tip of the electrode.

3.4.8　Finite plate electrode vs infinite plate electrode

In this chapter, we apply a potential profile at the upper and lower domain boundaries to make the simulations consistent with the experimental electrode geometry, as described in section 3.2.2. This potential profile depends in particular on the radius of the HV electrode in which the needle is embedded, see figure 3.1. If this electrode has a small radius, then the voltage will drop more rapidly in its vicinity, leading to a background field that is higher close to the electrode and lower farther away from it. If both the grounded and HV electrodes instead have a very large radius the voltage drop will be approximately linear, and the background field homogeneous.

Here, we compare simulation results for the experimental electrode geometry with results using quasi-infinite plate electrodes and the same 10 mm long protruding needle electrode. These 'infinite' electrodes are incorporated by applying a voltage uniformly on the upper and lower domain boundaries. We use a linearly increasing voltage with a rise time of 65 ns for both cases. Figure 3.16 (a), (b) and (c) show the streamer velocity, streamer radius, and the maximal electric field at the streamer head for these two cases. The background electric field and the potential along the z axis for these two cases are shown in figure 3.16 (d).

The use of infinite plate electrodes leads to a couple of clear differences:

- The voltage drop between the electrodes is now approximately linear at
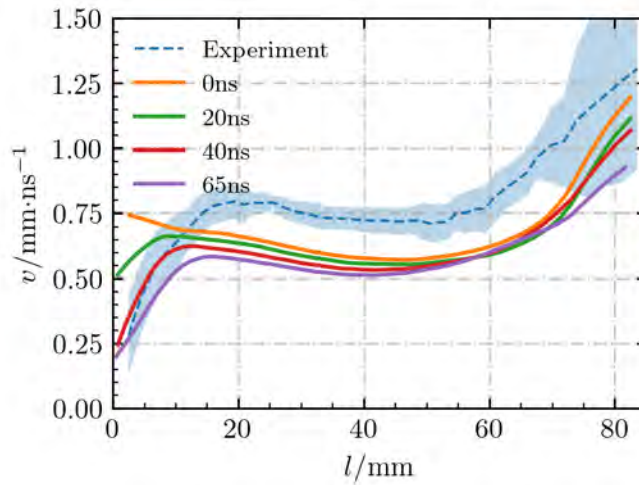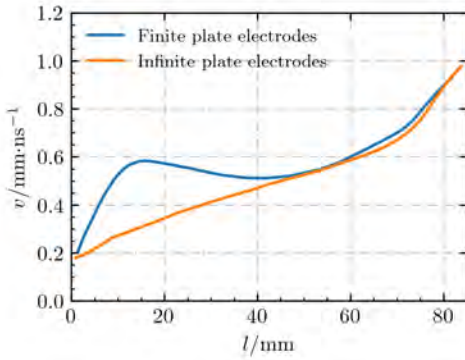
(a) Streamer velocity versus streamer length
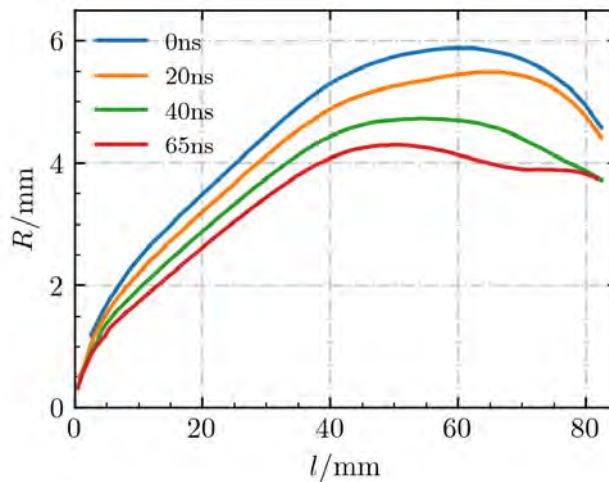
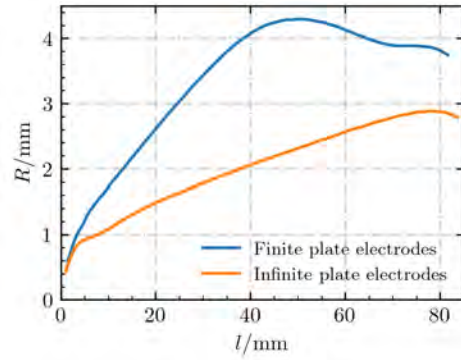(b) Streamer radius versus streamer length

Figure 3.15: The streamer velocity and streamer radius versus the streamer length for streamers with different voltage rise times.

$0 \, \text{mm} < z < 85 \, \text{mm}$, whereas with finite electrodes this drop is steeper near the HV electrode.

- The streamer velocity increases approximately linearly with streamer length, in contrast to the pattern of acceleration, deceleration and acceleration with finite electrodes.

- The streamer velocity is initially significantly lower, but when streamers
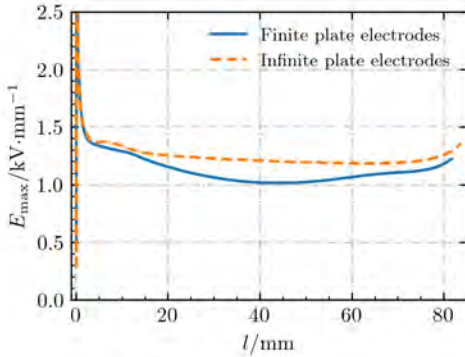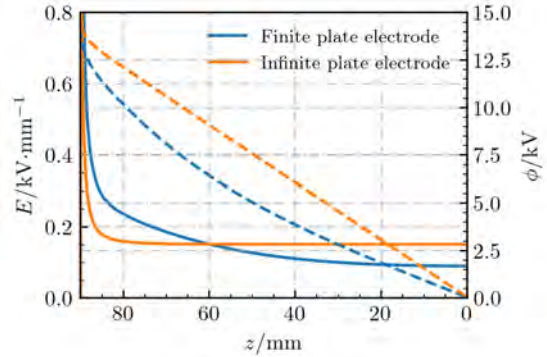
(a) Streamer velocity

(b) Streamer radius

(c) The $E_{\max}$

(d) The E and potential profiles

Figure 3.16: Panel(a) to panel(c) show the comparison of streamer propagation parameters for streamers versus the streamer length with finite plate electrodes and infinite plate electrodes, both with a needle electrode protruding 10 mm into a 10 cm wide gap. Panel(d) shows the electric field and potential distribution along the z axis in the absence of space charge. The solid lines are for electric fields, and the dashed lines for electric potentials.

have nearly bridged the whole gap their velocities are similar regardless of electrode geometry.

- The maximal electric field at the streamer head is now almost constant between 5 mm and 75 mm, whereas a decrease and consecutive increase are visible with finite electrodes.

- The background electric field is almost constant in the area 0 mm < z < 85 mm, whereas it continuously decreases from the needle electrode to the ground with finite electrodes.

- The streamer is thinner than with finite electrodes, and the streamer radius

keeps increasing until the streamer length is about 80 mm.

3.4.9   Effect of boundary conditions

The experiments are performed in a quasi-cylindrical vessel with a diameter of
32.4 cm and a height of 38.0 cm. The simulation domain does not capture the
whole vessel, see figure 3.1, so electrostatic boundary conditions for the simu-
lation domain need to be carefully set. The upper and lower boundaries use
pre-computed Dirichlet boundary conditions considering the effect of the finite
plate electrodes, as described in section 3.2.2. For our default case, these values
were pre-computed with a FEM method for a fully axisymmetric discharge ves-
sel with a 16 cm radius, in the absence of a discharge. However, the discharge
vessel contains observation windows and gas in and outlets, so it is not fully
axisymmetric, as shown in figure 3.17. In particular, it contains a large window
of 10 cm radius located 26 cm away from its center. Furthermore, we have thus
far applied homogeneous Neumann boundary conditions for the potential at the
radial boundary, whereas some type of Dirichlet boundary condition might be
more appropriate.

Figure 3.17: The geometry of the experimental discharge vessel, as seen from
the side. It is a quasi-cylindrical vessel that contains observation windows and
gas flow tubes. The ICCD camera captures pictures through the large window
on the right. We observed that streamers propagated slightly off-axis, with the
deviation towards the largest window, which is most likely related to the electric
potential distribution inside the vessel.

To investigate the effect of these boundary conditions on the potential, we
compare our default case with three other cases:

- Case 1: Identical to the default case, but using the FEM solution as a
  Dirichlet boundary condition on the radial boundary (instead of homoge-
  neous Neumann).

- Case 2: A larger $16\,\text{cm} \times 10\,\text{cm}$ computational domain, now using a Dirichlet zero boundary condition on the radial boundary.

- Case 3: Identical to case 1, but now the electric potential was pre-computed for a larger discharge vessel with a radius of $26\,\text{cm}$. This larger radius could account, to some extent, for the windows it contains.

Figure 3.18 shows the streamer velocity versus length for all cases. Case 1 and case 2 give similar results. Compared to the default case, streamer velocities are first slightly higher, but in the range $50\,\text{mm} < l < 80\,\text{mm}$ they are lower. This implies that the use of radial Dirichlet boundary conditions reduces the potential at the streamer head at later stages. On the one hand, the agreement between case 1 and case 2 shows that our computational domain is sufficiently large for these cases, so that the discharge and boundary conditions are only weakly coupled. On the other hand, the disagreement with the default case indicates that this coupling is significantly stronger with homogeneous Neumann boundary conditions. If we instead use boundary conditions pre-computed for a larger discharge vessel (case 3), the streamer velocity is similar to the default case.
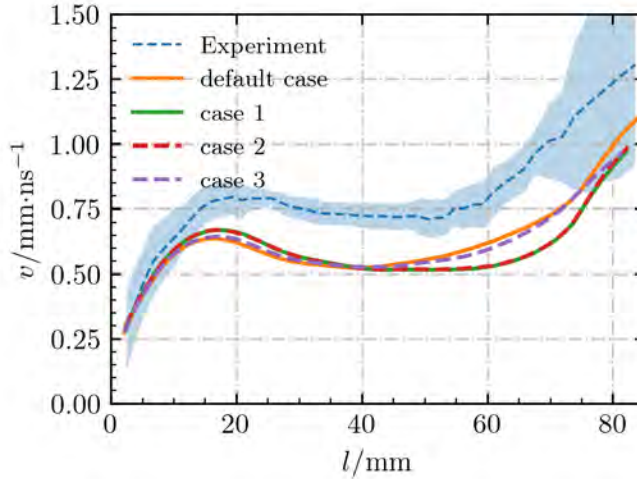

Figure 3.18: Streamer velocity versus streamer length for different boundary conditions for the electric potential. The default case uses homogeneous Neumann boundary conditions in the radial direction, whereas cases 1, 2 and 3 use Dirichlet boundary conditions, see section 3.4.9 for details.

It is difficult to say which of these cases most closely matches the experiments, as the actual discharge charge vessel is not axisymmetric and contains windows. That these windows play a role was confirmed experimentally, because the streamers propagated slightly off-axis, with the deviation towards the

largest window. The default case and case 3 seem to give slightly better qualitative agreement in the streamer velocity, but this could just be a coincidence. However, what we can conclude is that our results are sensitive to the used electrostatic boundary conditions. For future validation studies, this could mean there is a trade-off in the size of windows for optical access: large windows facilitate measurements, but they make it harder to accurately model the electrostatic boundary conditions.

3.4.10 Needle electrode vs initial ionized seed

In previous computational studies, an elongated ionized seed with an equal density of electrons and positive ions was often used as a pseudo-electrode to start a streamer, see e.g. [105, 146]. Due to electron drift such a seed becomes electrically screened, leading to a high electric field at its tip that can start a streamer discharge, depending on the shape and density of the seed [19]. However, to quantitatively compare simulations with experiments, we have here instead implemented an actual needle electrode in our field solver. This ensures that the electric potential at the electrode contour is equal to the applied voltage.
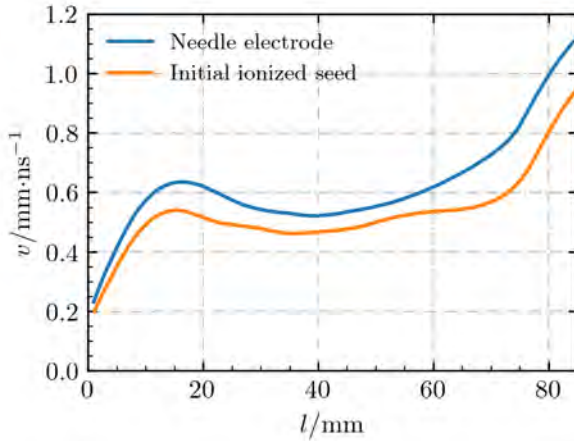
To compare streamers originating from a needle electrode to those originating from an ionized seed, we ran a simulation with an ionized seed of about $10\,\mathrm{mm}$ long with a radius of about $0.5\,\mathrm{mm}$. The electron and $\mathrm{N_2^+}$ density were $10^{19}\,\mathrm{m^{-3}}$ at its center, with a decay at a distance above $d = 0.3\,\mathrm{mm}$ using a so-called smoothstep profile: $1 - 3x^2 + 2x^3$ up to $x = 1$, where $x = (d - 0.3\,\mathrm{mm})/0.3\mathrm{mm}$ [111]. Figure 3.19 (a) shows the evolution of the electric potential at the tip of the seed and the needle electrode. With an actual electrode, the potential at the needle tip agrees with the applied voltage (shown in figure 3.2). But with an ionized seed, the actual potential at the seed tip is lower due to the seed's finite conductivity, and it essentially becomes part of the streamer. In other words, there is a potential drop between the plate electrode and the tip of the former seed. The streamer originating from an ionized seed is therefore slower, as shown in figure 3.19 (b).

3.5 Summary

We have quantitatively compared simulations and experiments of single positive streamers in artificial air at $0.1\,\mathrm{bar}$. Good qualitative agreement is observed between the experimental and simulated optical emission profiles. In both cases, the streamers have similarly shaped bright heads, and darker tails. The streamer velocity and radius also show good qualitative agreement. After inception, the streamers first accelerate, then they slowly decelerate, and finally they accelerate again when approaching the grounded electrode. Quantitatively, the simulated streamer velocity is about 20% to 30% lower at the same streamer length, and the simulated radius is about $1\,\mathrm{mm}$ (20% to 30%) smaller. These discrepancies
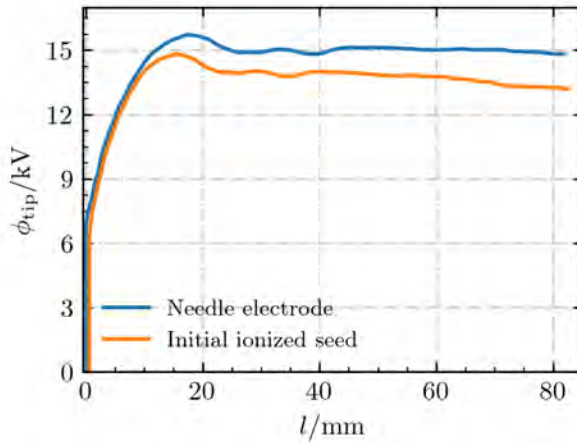
(a) Electric potential at the seed/needle electrode lower tip

(b) Streamer velocity versus streamer length

Figure 3.19: Comparison of streamers originating from an ionized seed (see text) and a needle electrode.

could be explained by a temperature increase in the experiments due to 50 Hz repetitive pulses.

3.5.1 Possible errors in the experimental measurements

1. In the experiments, only preliminary measurements were available for gas temperature variations in the vessel. These indicate that the gas temperature due to previous discharges could locally rise by roughly 10 to 100 K. A temperature increase towards the upper end of this range could explain much of the observed differences between simulations and experiments.

2. There are fluctuations in the streamer velocity obtained from the experimental images, since each image corresponds to a different discharge. The experimental velocity therefore has an intrinsic error of about 10% when compared at a particular position or time.

3. The experimental uncertainty in the applied voltage is about 2%, and in the gas pressure it is about 1%. The observed discrepancies in streamer velocity can therefore not be explained by errors in these parameters.

3.5.2 Possible errors in the simulations

1. The streamer properties in a fluid simulation depend on the used transport coefficients. The cross-section databases used here [115, 119, 124, 125] are often based on data obtained decades ago. It is difficult for us to assess the accuracy and uncertainty in this data, but having more recent cross-section data would be helpful for the validation of simulation models.

2. We have used a fluid model with the local field approximation. Previous studies have shown that the predictions of this model can deviate from those of particle-in-cell simulations, see e.g. [35]. However, based on recent unpublished comparisons of axisymmetric particle and fluid models in our group, we think such model error is unlikely to account for the observed discrepancies.

3. Related to the above point, discharge inception can sometimes not accurately be modeled with a fluid model, since the continuum approximation breaks down when there are few particles. This could perhaps also account for some of the observed discrepancies.

4. The experiments were performed with a 50 Hz repetition rate, but the simulations did not take into account remnants from previous pulses. An accumulation of long-lived excited species could for example lead to increased ionization rates. However, our simulations have been proven to be quite insensitive to initial ionization conditions.

5. The experimental vessel contains several windows, of which one is large, and it is not fully axisymmetric. This leads to uncertainty in the boundary conditions for the electric potential in the simulations. Our simulation results are sensitive to these boundary conditions. Experimentally, an off-axis deviation of the streamer towards the largest window was observed.

3.5.3 Summary of results for parameter studies

1. The propagation of the discharge considered here – a streamer developing on 10^2 ns time scale at 0.1 bar with a background electric field of about

$1.5\,\mathrm{kV/cm}$ – is mostly controlled by ionization reactions. Attachment, detachment and recombination reactions have a much smaller effect.

2. Using transport coefficients computed from different cross-section databases affects the simulated streamer evolution. However, the simulated velocities are always significantly lower than those in the experiments. The choice of Boltzmann solver (BOLSIG+ or Monte Carlo particle swarms) has little effect on the velocity. By artificially increasing both the ionization coefficient and the mobility by 20%, the simulated streamer velocity is much closer to the experimental one.

3. Increasing the applied voltage increases streamer velocities. With a $17.5\,\mathrm{kV}$ applied voltage, the simulated streamer velocity is similar to the experimental one at $15\,\mathrm{kV}$. However, the experimental uncertainty in the voltage is only about 2%. A longer voltage rise time initially slows down the streamers, but its effect is weaker at later times and longer streamer lengths.

4. Initial or background ionization is essential for streamer inception, but it hardly affects streamer propagation at later times. However, a very high background ionization level leads to slower streamers, as it reduces the field enhancement at their heads.

5. With ten times less photoionization, the streamer velocity increases by up to 30%, in particular when the streamer has almost bridged the gap. However, the velocity profile then differs qualitatively from the experimental measurements. With ten times more photoionization, streamers are significantly slower, as they lose some of their field enhancement due to the relatively high degree of ionization ahead of them.

6. A higher gas temperature leads to higher E/N values. For a $10\,\mathrm{K}$ change in the gas temperature, the change in the streamer velocity at the same length is about 3%. When the gas temperature is $360\,\mathrm{K}$ in the simulations, the difference between the simulated and experimental streamer velocity is less than 15%.

7. The size of the plate electrodes changes the background electric field in the gap. This affects the maximum electric field at the streamer head, and can lead to qualitatively different streamer propagation between the electrodes. With quasi-infinite plate electrodes, the streamer velocity monotonically increases within the gap.

Chapter 4

A computational study of steady and stagnating positive streamers in N$_2$-O$_2$ mixtures

In this chapter, we address two main topics: steady propagation fields for positive streamers in air and streamer deceleration in fields below the steady propagation field. We generate constant-velocity positive streamers in air with an axisymmetric fluid model, by initially adjusting the applied voltage based on the streamer velocity. After an initial transient, we observe steady propagation for velocities of $3 \times 10^4 \, \mathrm{m/s}$ to $1.2 \times 10^5 \, \mathrm{m/s}$, during which streamer properties and the background field do not change. This propagation mode is not fully stable, in the sense that a small change in streamer properties or background field eventually leads to acceleration or deceleration. An important finding is that faster streamers are able to propagate in significantly lower background fields than slower ones, indicating that there is no unique stability field. We relate the streamer radius, velocity, maximal electric field and background electric field to a characteristic time scale for the loss of conductivity. This relation is qualitatively confirmed by studying streamers in N$_2$-O$_2$ mixtures with less oxygen than air. In such mixtures, steady streamers require lower background fields, due to a reduction in the attachment and recombination rates. We also study the deceleration of streamers, which is important to predict how far they can propagate in a low field. Stagnating streamers are simulated by applying a constant applied voltage. We show how the properties of these streamers relate to the steady cases, and present a phenomenological model with fitted coefficients that describes the evolution of the velocity and radius. Finally, we compare the lengths of the stagnated streamers with predictions based on the conventional stability field.

The introduction and simulation model sections have been condensed for conciseness in this adaptation.

4.1 Introduction

The behavior of streamers strongly correlates with the background electric field E_{bg}. Depending on E_{bg}, the propagation of a streamer can be accelerating, steady, or stagnating. The goal of this chapter is to better understand positive streamer propagation in air. In particular, we study when such streamers accelerate or decelerate in homogeneous fields, by locating the unstable boundary between these regimes with numerical simulations.

We simulate the propagation of positive streamers in air with a 2D axisymmetric fluid model, which is described in section 4.2. In section 4.3, we investigate the properties of steady streamers, which are obtained by adjusting the applied voltage based on the streamer velocity. We simulate constant-velocity streamers at velocities of 0.03 to 0.12 mm/ns and obtain corresponding steady propagation field and apply dimensional analysis to relate the streamer radius, velocity, maximal electric field and background electric field to a characteristic time scale for the loss of conductivity. Afterwards, the deceleration of streamers is studied in section 4.4, by simulating stagnating streamers in a low background field. We show how the properties of these streamers relate to the constant-velocity cases and present a phenomenological model to describe the change in velocity and radius. We compare the lengths of the stagnated streamers with predictions based on the conventional stability field, and link the electric field inside the streamer channel with experimental stability fields.

4.2 Simulation model

4.2.1 Fluid model and chemical reactions

We use a 2D axisymmetric drift-diffusion-reaction type fluid model with the local field approximation, as described in chapter 2. The chemical reactions considered in this chapter are listed in table 4.1. They include electron impact ionization (k_1–k_3), electron attachment (k_4, k_5), electron detachment (k_6-k_8), ion conversion (k_9-k_{13}) and electron-ion recombination (k_{14}, k_{15}). The electron transport data and the electron impact reaction coefficients depend on the reduced electric field E/N, and they were computed using BOLSIG+ [116] with Phelps' cross sections for (N$_2$, O$_2$) [115, 123] using a temporal growth model. As was pointed out in [110], data computed with a temporal growth model is more suitable for positive streamer simulations than data computed with a spatial growth model, which was used in [48].

The source terms S corresponding to reaction list 4.1 is expressed as

$$S = f_\varepsilon S_i - S_\eta + S_{\text{detach}} - S_{\text{recom}} + S_{\text{ph}}, \tag{4.1}$$

where S_i, S_η, S_{detach}, S_{recom} and S_{ph} are the source terms for impact ionization, attachment, detachment, electron-ion recombination and non-local photoioniza-

Table 4.1: Reactions included in the model, with reaction rates and references. The electron temperature T_e in reaction rates k_{14} and k_{15} is obtained from the mean electron energy (ϵ_e) computed by BOLSIG+ as $T_e = 2\epsilon_e/3k_B$. Reaction coefficients k_1 - k_5 are computed using BOLSIG+ [116] with Phelps' cross sections for (N_2, O_2) [115], k_6, k_7, k_{14} and k_{15} are retrieved from [113], k_8 - k_{10} from [149], and k_{11} - k_{13} from [150].

No.	Reaction	Reaction rate coefficient
1	$e + N_2 \xrightarrow{k_1} e + e + N_2^+$ (15.60 eV)	$k_1(E/N)$
2	$e + N_2 \xrightarrow{k_2} e + e + N_2^+$ (18.80 eV)	$k_2(E/N)$
3	$e + O_2 \xrightarrow{k_3} e + e + O_2^+$	$k_3(E/N)$
4	$e + O_2 + O_2 \xrightarrow{k_4} O_2^- + O_2$	$k_4(E/N)$
5	$e + O_2 \xrightarrow{k_5} O^- + O$	$k_5(E/N)$
6	$O_2^- + N_2 \xrightarrow{k_6} O_2 + N_2 + e$	$k_6 = 1.13 \times 10^{-25}\,\mathrm{m^3 s^{-1}}$
7	$O_2^- + O_2 \xrightarrow{k_7} O_2 + O_2 + e$	$k_7 = 2.2 \times 10^{-24}\,\mathrm{m^3 s^{-1}}$
8	$O^- + N_2 \xrightarrow{k_8} e + N_2O$	$k_8 = 1.16 \times 10^{-18} \exp(-(\frac{48.9}{11+E/N})^2)\,\mathrm{m^3 s^{-1}}$
9	$O^- + O_2 \xrightarrow{k_9} O_2^- + O$	$k_9 = 6.96 \times 10^{-17} \exp(-(\frac{198}{5.6+E/N})^2)\,\mathrm{m^3 s^{-1}}$
10	$O^- + O_2 + M \xrightarrow{k_{10}} O_3^- + M$	$k_{10} = 1.1 \times 10^{-42} \exp(-(\frac{E/N}{65})^2)\,\mathrm{m^6 s^{-1}}$
11	$N_2^+ + N_2 + M \xrightarrow{k_{11}} N_4^+ + M$	$k_{11} = 5 \times 10^{-41}\,\mathrm{m^6 s^{-1}}$
12	$N_4^+ + O_2 \xrightarrow{k_{12}} O_2^+ + N_2 + N_2$	$k_{12} = 2.5 \times 10^{-16}\,\mathrm{m^3 s^{-1}}$
13	$O_2^+ + O_2 + M \xrightarrow{k_{13}} O_4^+ + M$	$k_{13} = 2.4 \times 10^{-42}\,\mathrm{m^6 s^{-1}}$
14	$e + O_4^+ \xrightarrow{k_{14}} O_2 + O_2$	$k_{14}(E/N) = 1.4 \times 10^{-12}(300\mathrm{K}/T_e)^{1/2}\,\mathrm{m^3 s^{-1}}$
15	$e + N_4^+ \xrightarrow{k_{15}} N_2 + N_2$	$k_{15}(E/N) = 2.0 \times 10^{-12}(300\mathrm{K}/T_e)^{1/2}\,\mathrm{m^3 s^{-1}}$

tion, respectively, and f_ε is a correction factor discussed below. Photoionization is computed according to Zheleznyak's model [89] using the Helmholtz approximation [135, 136], using the same photoionization model as [48].

Our model includes ion motion, which can be important at relatively low streamer velocities or when studying streamer stagnation [51]. For simplicity, we use a constant ion mobility $\mu_{\mathrm{ion}} = 2.2 \times 10^{-4}\,\mathrm{m^2/Vs}$ [155] for all ion species, as was also done in [48].

It can be difficult to simulate slow or stagnating positive streamers with a standard fluid model using the local field approximation [51]. Such streamers have a small radius, leading to strong electron density and field gradients that reduce the validity of the local field approximation [156, 157]. In [48–50] the electric field at the streamer tip was found to rapidly increase during streamer stagnation, and simulations had to be stopped after the field became unphysically large. Recently, it was shown that such unphysical behavior can be avoided by using an extended fluid model that includes a source term correction depending

on ∇n_e [51]. In this chapter, we instead use a correction factor f_ϵ for the impact ionization term as described in [158, 159]. This factor is given by

$$f_\epsilon = 1 - \frac{\hat{\mathbf{E}} \cdot \mathbf{\Gamma}^{\mathrm{diff}}}{||\mathbf{\Gamma}^{\mathrm{drift}}||}, \tag{4.2}$$

where $\hat{\mathbf{E}}$ is the electric field unit vector, and $\mathbf{\Gamma}^{\mathrm{diff}}$ and $\mathbf{\Gamma}^{\mathrm{drift}}$ are the diffusive and drift flux of electrons, respectively, and f_ϵ is limited to the range of $[0, 1]$. As discussed in [158, 159], this correction factor prevents unphysical growth of the plasma near strong density and field gradients. The underlying idea is that the diffusive electron flux parallel to the electric field (thus corresponding to a loss of energy) should not contribute to impact ionization.

4.2.2 Computational domain and initial conditions

We simulate positive streamers in N$_2$-O$_2$ mixtures at 300 K and 1 bar, using the axisymmetric computational domain illustrated in figure 4.1. A high voltage is applied to the upper plate electrode (at $z = 40$ mm), which includes a needle protrusion. The needle protrusion is implemented by modifying the multigrid methods in [109] using a level-set function, as described in [145]. For the constant-velocity streamers simulated in section 4.3, this needle is 2 mm long, with a radius of 0.2 mm and a semispherical tip. To generate the stagnating streamers simulated in section 4.4, more field enhancement is required. The needle used there is 8 mm long, with a radius of 0.2 mm, a conical tip with 60° top angle and a tip curvature radius of 50 μm. The lower plate electrode (at $z = 0$ mm) is grounded. A homogeneous Neumann boundary condition is applied for the electric potential on the radial boundary. For plasma species densities, homogeneous Neumann boundary conditions are used on all the domain boundaries. However, at the positive high-voltage electrode electron fluxes are absorbed but not emitted.

With the short needle electrode the axial electric field is approximately uniform, except for a small area around the needle tip, as shown in figure 4.1. For z between 0 mm and 32 mm, the electric field differs less than 1% from the average electric field between the plates E_{bg}. We therefore refer to E_{bg} as "the background electric field" in the rest of the chapter.

To initiate the discharges, a neutral Gaussian seed consisting of electrons and positive ions (N$_2^+$) is used. Its density is given by $n_0 \exp(-(d/R)^2)$, with $n_0 = 10^{15}$ m^{-3}, d the distance to the needle tip and $R = 0.5$ mm. Besides this initial seed, no other initial ionization is included.

Adaptive mesh refinement is used as described in equation (2.14). We use $c_0 = 0.5$, $c_1 = 1.25$ and $d_0 = 10\,\mu$m, which leads to a minimal grid spacing of $\Delta x_{\mathrm{min}} = 1.4\,\mu$m.
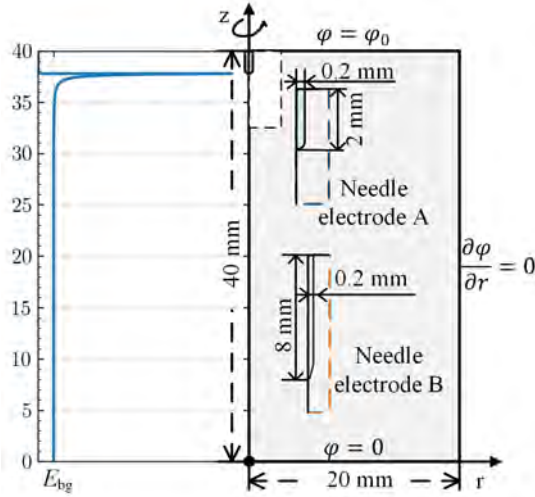
Figure 4.1: The computational domain. Right: electrode geometry and boundary conditions. The needle protrusions used for generating constant-velocity (needle electrode A) and stagnating streamers (needle electrode B) are illustrated. Left: axial electric field distribution with the 2 mm long needle. E_{bg} is the average electric field between the plate electrodes.

4.2.3   Velocity control method

In this chapter, we study steady streamers propagating at a constant velocity. To generate such streamers, we adjust the applied voltage ϕ based on the difference between the present streamer velocity v and a goal velocity v_{goal}. In the simulations, we cannot accurately measure v at every time step. Instead, we take samples v^* after the streamer head has moved more than $8\,\Delta x_{\mathrm{min}}$

$$v^* = \left(z_{\mathrm{head}}^{i} - z_{\mathrm{head}}^{i-1}\right) / \left(t^i - t^{i-1}\right),$$

where z_{head} is the location of the maximum electric field and the superscripts ^{i} and $^{i-1}$ indicate the present and previous sampling time. Since this estimate is still rather noisy, we average it with the four most recent samples of v to obtain a smoothed velocity v^i. The voltage is then updated as

$$\phi^i = \phi^{i-1} + K_p(t^i - t^{i-1})(1 - v^i/v_{\mathrm{goal}}), \tag{4.3}$$

where K_p is a proportionality constant between $5 \times 10^{13}\,\mathrm{V/s}$ and $2 \times 10^{14}\,\mathrm{V/s}$.

Figure 4.2 shows an example of a streamer forced to propagate at $5 \times 10^4\,\mathrm{m/s}$. Corresponding profiles for the streamer velocity and applied voltage are shown in figure 4.3 (the solid line). Initially, the applied voltage is $44\,\mathrm{kV}$, which corresponds to a background electric field of $11\,\mathrm{kV/cm}$. The applied voltage is adjusted after $2\,\mathrm{ns}$, using $K_p = 7 \times 10^{13}\,\mathrm{V/s}$. As the applied voltage is reduced,

the streamer velocity decreases, until it eventually converges to the goal velocity after about 50 ns. The applied voltage then slightly increases, until it stabilizes after about 200 ns.
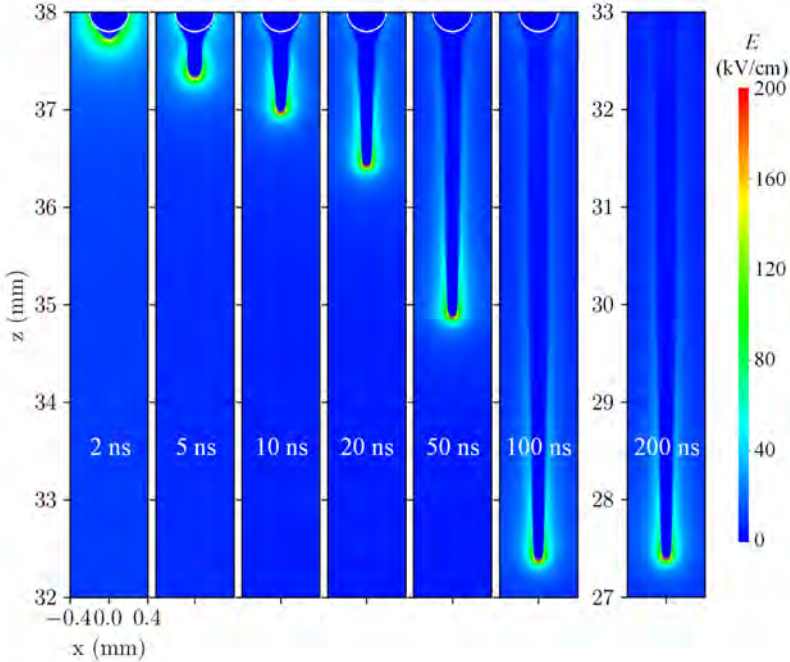

Figure 4.2: Electric field strength between 2 ns and 200 ns for a streamer whose velocity is forced to 5×10^4 m/s by the velocity control method described in section 4.2.3. Note that the rightmost sub-figure has a different z axis. The white curves indicate the tip of the needle electrode.

The initially applied voltage (ϕ_0), the delay until the voltage is first adjusted (T_0) and the coefficient K_p can affect how the streamer velocity approaches the goal value. Figure 4.3 shows the streamer velocities (a) and applied voltages (b) versus time for streamers whose velocities are forced to be 5×10^4 m/s but with different ϕ_0, T_0 and K_p. Note that in the rest of the chapter we will use $\phi_0 = 44$ kV, $T_0 = 2$ ns, and $K_p = 7 \times 10^{13}$ V/s, unless stated otherwise.

Although the initial profiles vary, they eventually converge to the same value, which is also true for the streamer radius and the maximal electric field (which are not shown here). Two additional cases are included in figure 4.3. One is with a wider initial seed ($R = 2$ mm), and the other is with a longer needle electrode (2.5 mm). As shown in figure 4.3, the corresponding applied voltages converge to the same value. These examples therefore suggest that there is a unique propagation mode for a given constant streamer velocity. We have observed that for a steady streamer the charge profile near the streamer head translates with the streamer velocity, so that it remains constant.
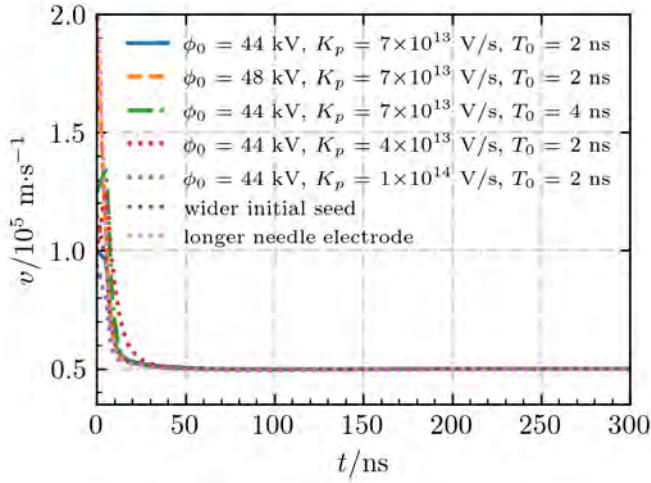
(a) The streamer velocity versus time
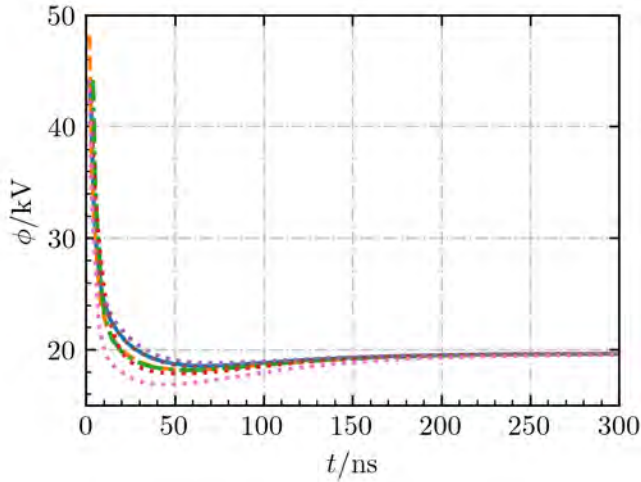
(b) The applied voltage versus time

Figure 4.3: The streamer velocity and applied voltage versus time for streamers whose velocities are forced to be 5×10^4 m/s. The initially applied voltage ϕ_0, the start time of voltage adjustment T_0 and the coefficient K_p in the velocity control method are varied. The cases labeled "wider initial seed" and "longer needle electrode" correspond to a $R = 2$ mm initial Gaussian seed and a 2.5 mm long needle electrode. For these two cases, $\phi_0 = 44$ kV, $T_0 = 2$ ns, and $K_p = 7 \times 10^{13}$ V/s.

4.3   Investigation of steady streamers

In this section, we investigate "steady streamers" at constant velocities. We
remark that these streamers are not actually stable, in the sense that a small
change in their properties would lead to either acceleration or deceleration, as
shown in 4.3.4. The streamers studied here thus demarcate the unstable bound-
ary between acceleration and deceleration.

4.3.1   Background electric fields for steady streamers with different velocities

We simulate streamers at constant velocities from 3×10^4 m/s to 1.2×10^5 m/s,
using the velocity control method described in section 4.2.3. For the two slowest
and two fastest streamers, we use $K_p = 5 \times 10^{13}$ V/s and 2×10^{14} V/s, respectively.
For the streamer at a velocity of 1×10^5 m/s, $K_p = 1 \times 10^{14}$ V/s is used. A
larger K_p is used for faster streamers so that it takes a similar distance for all
streamers to enter a steady propagation mode. Figure 4.4 shows the electric field
and the electron density for these streamers when their heads are at z $=$ 16 mm,
and corresponding on-axis curves are shown in figure 4.5. Furthermore, figure 4.6
shows the evolution of the streamer velocity (v), radius (R), maximal electric field
(E_{max}) and the background electric field (E_{bg}) versus streamer head position.
The streamer radius is here defined as the radial coordinate at which the radial
electric field has a maximum. We remark that there are other definitions of the
streamer radius, such as the optical radius and the electrodynamic radius [18],
which would lead to a different value. When the streamers reach steady states, v,
R, E_{max} and E_{bg} all remain constant. The values corresponding to these steady
states are shown versus each other in figure 4.7.

Faster steady streamers have a larger radius and a lower maximal electric
field, but they require a lower background electric field. For streamer velocities
from 3×10^4 m/s to 1.2×10^5 m/s the corresponding background electric fields
decrease from 5.4 kV/cm to 4.1 kV/cm. This dependence might at first seem
surprising, but can be explained by considering the loss of conductivity in the
streamer channel. Behind the streamer head, electron densities decrease due to
attachment and recombination, and the electric field relaxes back to the back-
ground electric field [48]. This suggests we can define an effective streamer length
as $L_{\mathrm{eff}} = v\tau$, over which the background electric field is screened, where τ is a
typical time scale for the loss of conductivity. A faster streamer thus has a longer
effective length, as can be seen in figure 4.5. A lower background electric field is
therefore sufficient to get a similar amount of electric field enhancement. That
streamers can have a finite conducting length was recently also observed in [48].

With our axisymmetric model, we could not obtain steady streamers faster
than 1.2×10^5 m/s due to streamer branching. Another limitation was the limited
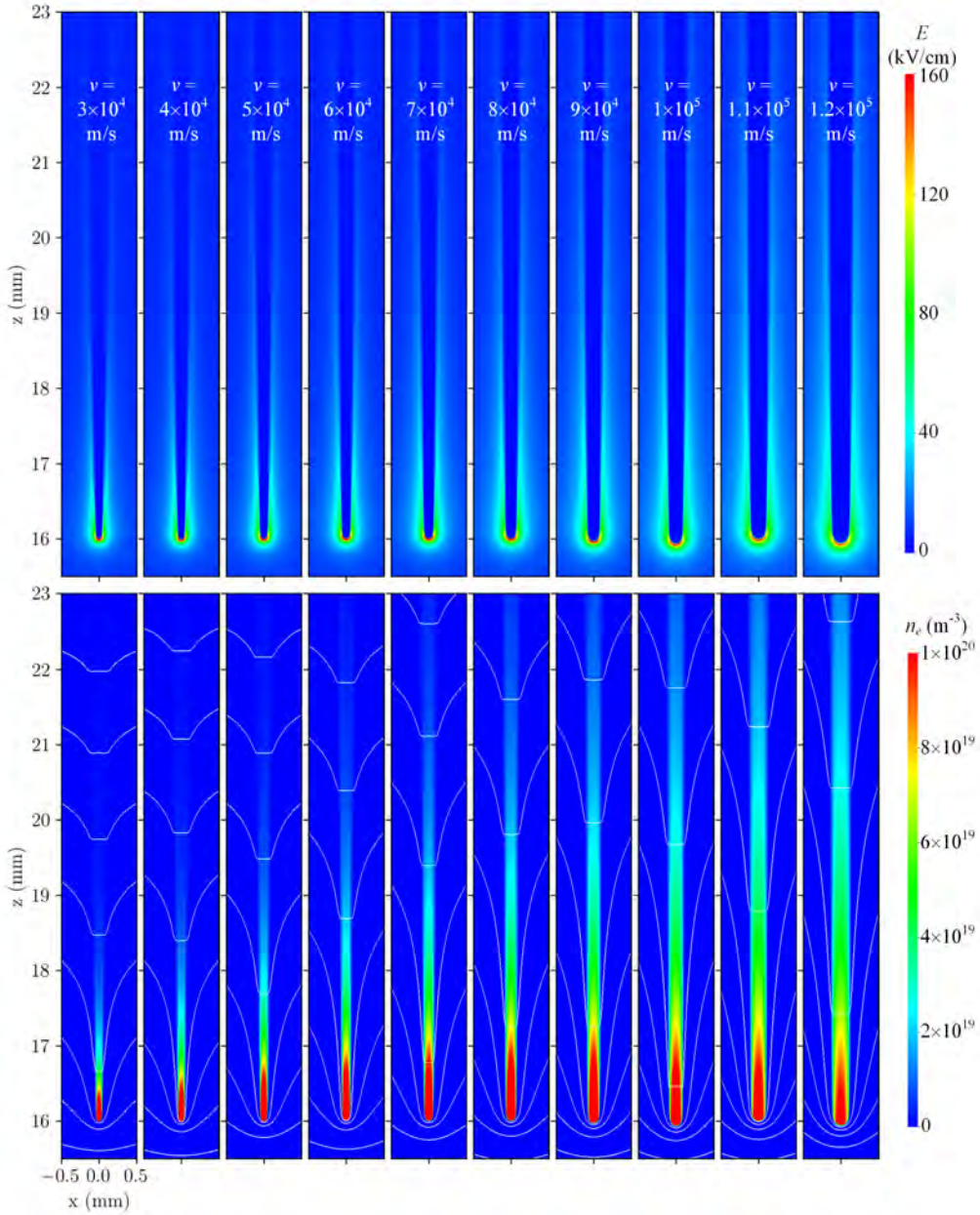domain length, due to which the background electric field for the fastest two

Figure 4.4: The electric field strength and the electron density for streamers in air at velocities of 3×10^4 m/s to 1.2×10^5 m/s, when their heads are at z = 16 mm. All these streamers have reached steady states. The white equipotential lines are spaced by 0.5 kV. Behind the streamer heads, the radius increases due to ion motion.
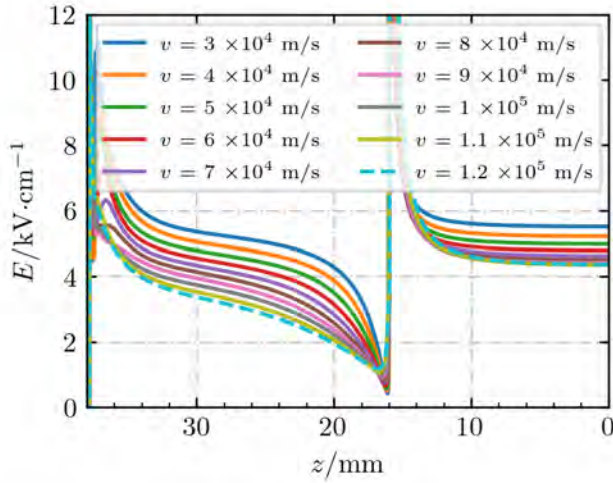
(a) The axial electric field strength
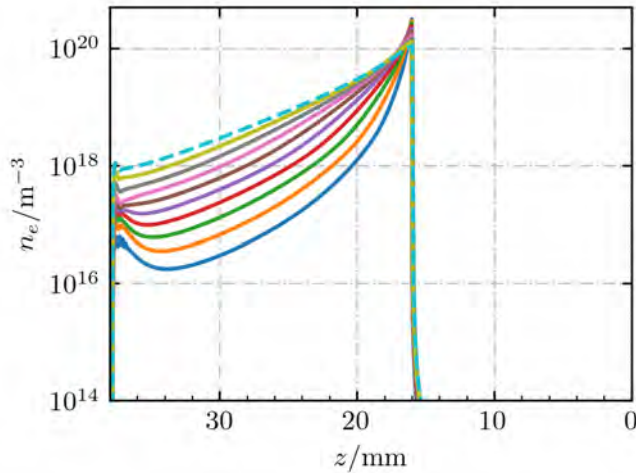
(b) The axial electron density

Figure 4.5: The axial electric field strength and electron density corresponding to figure 4.4.

cases does not become completely constant in figure 4.6(b). Streamers slower than 3×10^4 m/s were also difficult to obtain, because the streamer velocity then becomes comparable to the ion drift velocity at the streamer head, causing the streamers to easily stagnate. However, the range of steady propagation fields in our simulations agrees well with the range of experimental stability fields (from 4.14 kV/cm to 6 kV/cm) in [41, 43, 44].

Our results show that the streamer stability field depends not only on the gas,

(a) Streamer velocity

(b) Background electric field

(c) Streamer radius

(d) The maximal electric field
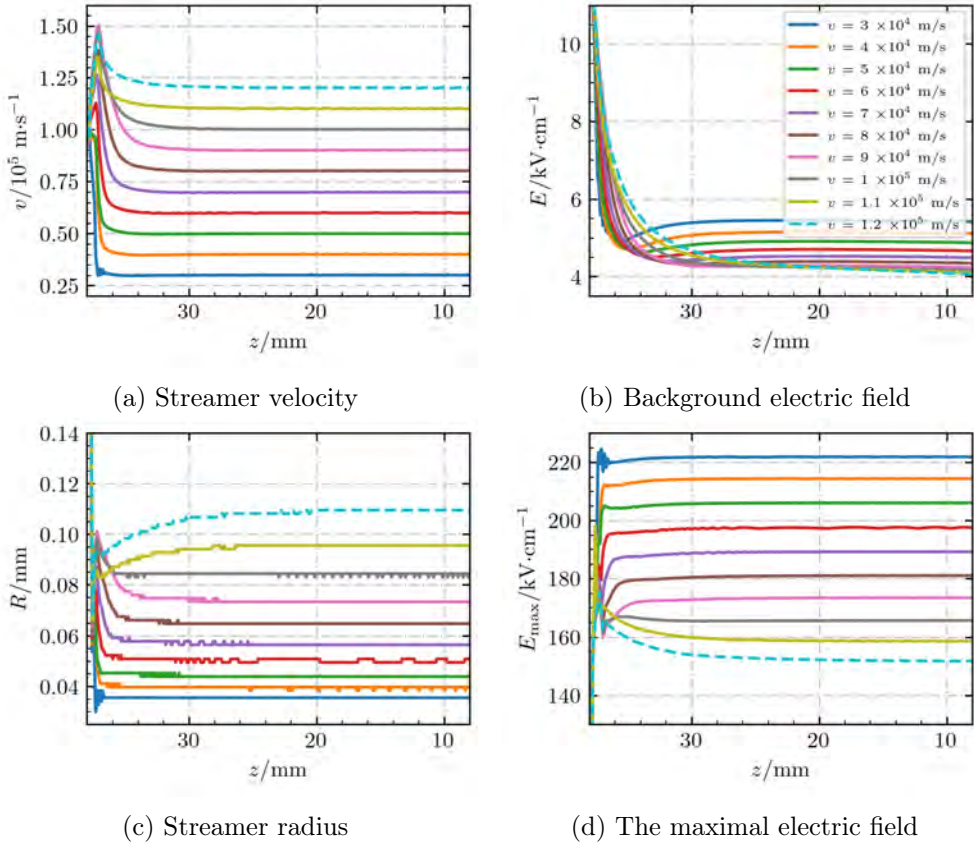
Figure 4.6: Streamer velocity, background electric field, streamer radius and the maximal electric field versus the vertical position of the streamer head for streamers in air at velocities from 3×10^4 m/s to 1.2×10^5 m/s. We take the location of the maximal electric field as the streamer head position, and the radius as the radial coordinate at which the radial electric field has a maximum. The thinnest (and slowest) streamer has a radius of around $35\,\mu$m.

but also on the streamer properties. If a faster and wider streamer is able to form, it can propagate in lower background electric fields, which could explain some of the variation in experimentally determined stability fields in air. For example, in [44] streamers were generated from a needle in a plate-plate geometry. It was found that a higher pulse voltage generated faster streamers, which required a lower background electric field to cross the gap. The minimal steady propagation field in our simulations is about $4.1\,\mathrm{kV/cm}$. This value agrees well with the lowest stability fields in air in previous experimental studies [43, 44, 46].

4.3.2 Analysis of steady streamer properties

Figure 4.7 shows streamer velocities, radii, maximal electric fields and background electric fields corresponding to steady propagation. Two approximately proportional relations between these variables can be observed. The ratio E_{max}/E_{bg} is about 40 ± 2, and the ratio R/v is about (0.95 ± 0.2) ns. Below, we show how these properties can be linked by considering the electric potential difference at the streamer head $\delta\phi$.
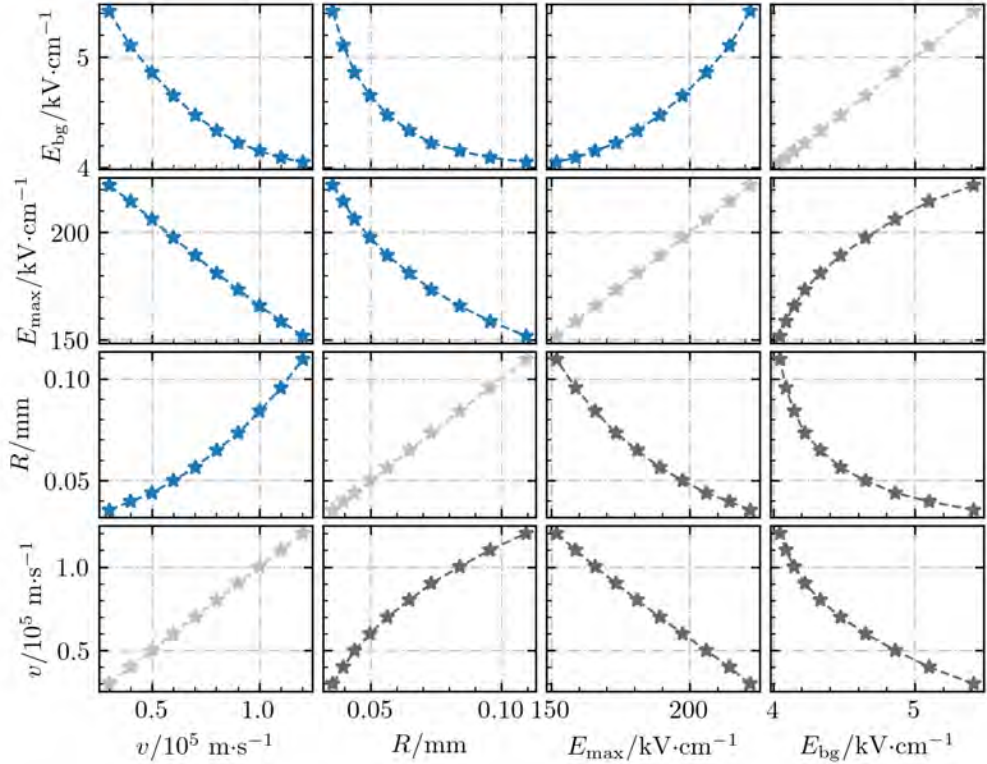

Figure 4.7: Overview of steady streamer properties. The blue curves show streamer velocity v, streamer radius R, maximum electric field E_{max} and background electric field E_{bg}. Each star symbol represents a steady propagation state, by taking the average over the last 30 ns of propagation. The picture shows each variable as a function of each other variable, with rows sharing the same y-axis and columns the same x-axis.

First, the effective streamer length can be written as $L_{eff} = v\tau$, where τ is a characteristic time scale for the loss of conductivity, see section 4.3.1. Just behind the streamer head, the electric field is almost fully screened, and further behind the head it relaxes back to the background field. Assuming that the relaxation occurs exponentially, with a characteristic length scale L_{eff}, the corresponding

potential difference is

$$\delta\phi = v\tau E_{\mathrm{bg}}. \tag{4.4}$$

Second, the electric field in the vicinity of a streamer head decays approximately quadratically, like that of a charged sphere, with the decay depending on the streamer radius. If one assumes that $E_{\mathrm{bg}} \ll E_{\max}$, a simple approximation is given by $E(z) = E_{\max}(1 + z/R)^{-2}$, with $z = 0$ corresponding to the location of $E_{\max}$ at the streamer head. Although this approximation is only justified for $z \lesssim R$, most of the potential drop occurs in this region. It is therefore not unreasonable to integrate up to ∞, giving

$$\delta\phi = \int_0^\infty E(z)dz = E_{\max}R. \tag{4.5}$$

If equations (4.4) and (4.5) are combined, the result is

$$\tau = \frac{E_{\max}R}{vE_{\mathrm{bg}}}. \tag{4.6}$$

Figure 4.8 shows τ, as defined by equation (4.6), versus the background electric field and the streamer velocity. The result lies between 33 and 49 ns, which corresponds well with the electron loss time scales due to recombination and attachment given in [48]. Variation in τ is to be expected, because attachment and recombination rates in the streamer channel can vary, for example due to different electron densities and the electric field profiles. Furthermore, equation (4.6) was derived based on rather simple approximations, and does for example not take the degree of ionization produced by the streamer into account.
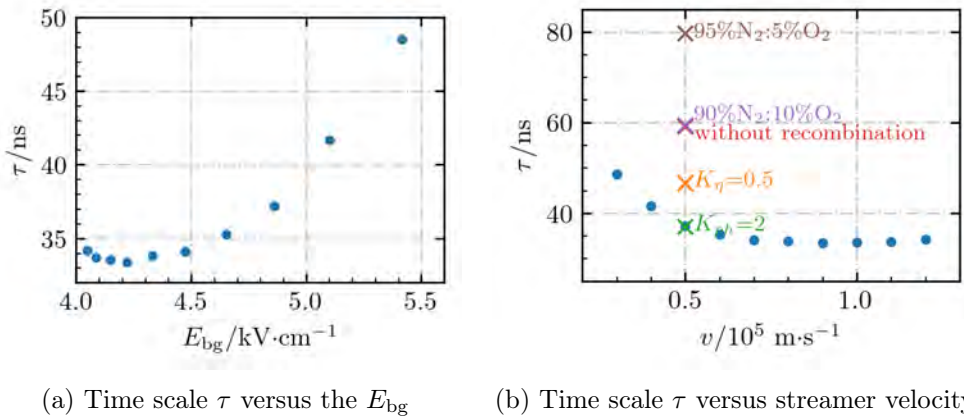
(a) Time scale τ versus the E_{bg} (b) Time scale τ versus streamer velocity

Figure 4.8: The time scale τ given by equation (4.6) versus the background electric field and versus the streamer velocity for the steady streamers in figure 4.6 and 4.9.

4.3.3   Steady streamers in other N$_2$-O$_2$ mixtures

In this section, we study streamers propagating at 5×10^4 m/s in other N$_2$-O$_2$ mixtures, namely 90%N$_2$:10%O$_2$ and 95%N$_2$:5%O$_2$, again using the velocity control method but with $T_0 = 4$ ns. We also consider cases with modified data for air, using either half the attachment rate, double the amount of photoionization or no recombination reactions, to understand the effect of these processes on the steady propagation mode. Figure 4.9 shows the background electric field versus streamer position for these cases. The steady propagation fields for streamers at 5×10^4 m/s are around 4.9 kV/cm in air, 3.5 kV/cm in 90%N$_2$:10%O$_2$ and 2.9 kV/cm in 95%N$_2$:5%O$_2$.
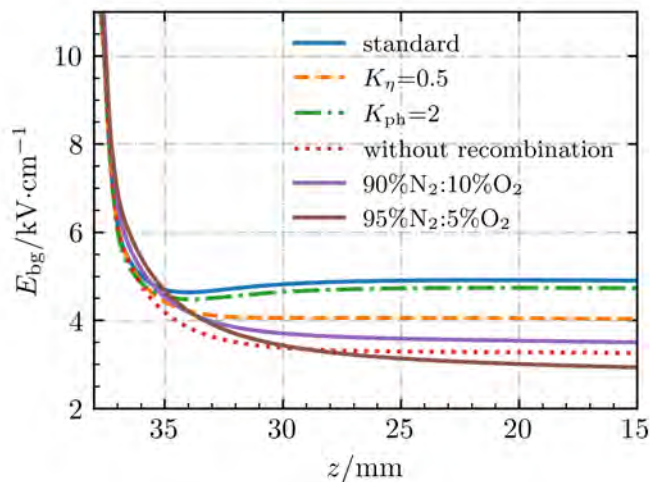
Figure 4.9: Background electric field versus streamer position for different N$_2$-O$_2$ mixtures and for different transport data. The streamers obtain a constant velocity of 5×10^4 m/s. The label "standard" indicates the streamer in artificial air (80%N$_2$:20%O$_2$). The labels "$K_\eta = 0.5$" and "$K_{\mathrm{ph}} = 2$" indicate cases with half the attachment rate and double the amount of photoionization, respectively.

As shown in figure 4.9, the effect of doubling the amount of photoionization is rather small, in agreement with e.g. [38, 106]. However, both the attachment and the recombination rate have a significant effect on the steady propagation field. This explains why steady propagation fields are lower with less O$_2$, as attachment and recombination rates are then reduced, see table 4.1. The dominant recombination process in our simulations is between e and O$_4^+$, as O$_4^+$ is one of the main positive ions in the streamer channel [142]. With less O$_2$, there will also be less O$_4^+$.

The ×-symbols in figure 4.8 show the electron loss time scale τ given by equation (4.6) for these steady streamers. As expected, τ increases when the attachment rate is halved, when recombination reactions are omitted and when

there is less O_2. Note that for the case $K_\eta = 0.5$, only the attachment rates are halved, and the recombination rates remain the same. It is therefore different from the case in $90\%N_2$:$10\%O_2$, in which both attachment and recombination are reduced.

4.3.4   Instability of steady positive streamers

We here illustrate the instability of steady positive streamers. First, a streamer whose velocity is forced to be 5×10^4 m/s. At 250 ns, it reaches a steady state with a E_{bg} of 4.9 kV/cm. We use this steady state as the initial condition and restart the simulation with E_{bg} modified by ± 0.1 kV/cm. Figure 4.10 shows that the streamer velocity then differs about 30% after 200 ns. Similar behavior was previously found in [48] for positive streamers and in [39] for steady negative streamers.
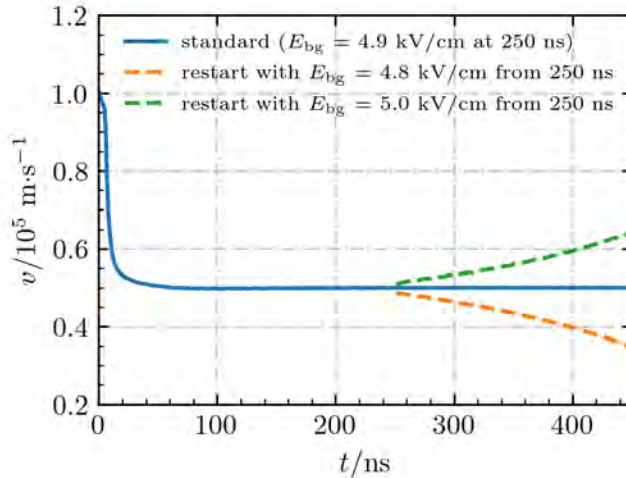
Figure 4.10: Illustration of the instability of steady positive streamers. The solid line represents a streamer whose velocity is forced to be 5×10^4 m/s. The dashed lines represent streamers that continued from the steady case at 250 ns in a background electric field modified by ± 0.1 kV/cm.

4.4   Investigation of stagnating streamers

Being able to predict whether a streamer can cross a given discharge gap is useful for many applications. In section 4.3 we have investigated streamers at constant velocities, which lie at the unstable boundary between acceleration and deceleration. These results help to predict whether a streamer with a certain radius and velocity will accelerate or decelerate, depending on the background field.

However, streamers that decelerate might still propagate a significant distance. To predict how far they will go, we need to better understand their deceleration. In this section we therefore simulate decelerating streamers that eventually stagnate.

4.4.1 The characteristics of stagnating streamers

In this section, stagnating streamers are generated in low background fields, using constant applied voltages. To still get discharge inception, a longer and sharper needle electrode is used, as described in section 4.2. Simulations are performed at constant applied voltages of 11.2, 12 and 12.8 kV, which correspond to background electric fields of 2.8, 3.0 and 3.2 kV/cm, respectively. Figure 4.11 shows the discharge evolution for the 12 kV case. The streamer decelerates and becomes narrower between 50 ns and 250 ns, and it stops after about 250 ns. Note that the electric field and electron density at the streamer head also decay after 250 ns, in agreement with [51].
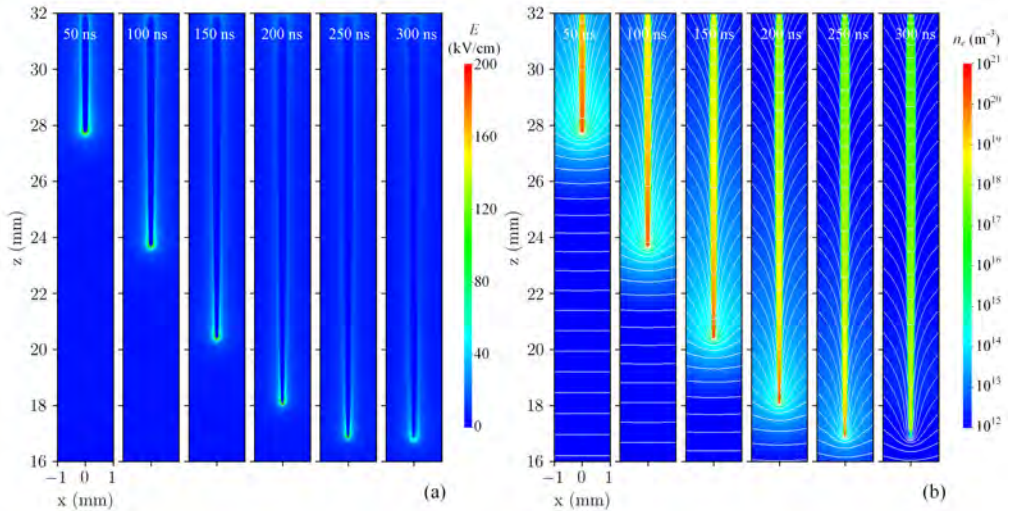

Figure 4.11: Electric field (a) and electron density (b) of the stagnating positive streamer in air with an applied voltage of 12 kV between 50 ns and 300 ns. The white equipotential lines are spaced by 240 V.

Figure 4.12 shows the evolution of the streamer head position, velocity, radius and maximal electric field for the three stagnating streamers. As expected, a streamer stops earlier with a lower applied voltage. Several phases can be identified. First there is acceleration in the high field near the electrode, during which R increases and E_{max} decreases. Then there is a transition period, after which the streamer starts to decelerate, with R decreasing and E_{max} increasing, and the amount of charge in the streamer head decreasing. Eventually, the

streamer velocity becomes similar to the ion velocity at the streamer head, and the streamer stagnates, as was also observed in [51]. The stagnation time and length are defined as the time and the streamer length when the radius again starts to increase, as shown in figure 4.12c.
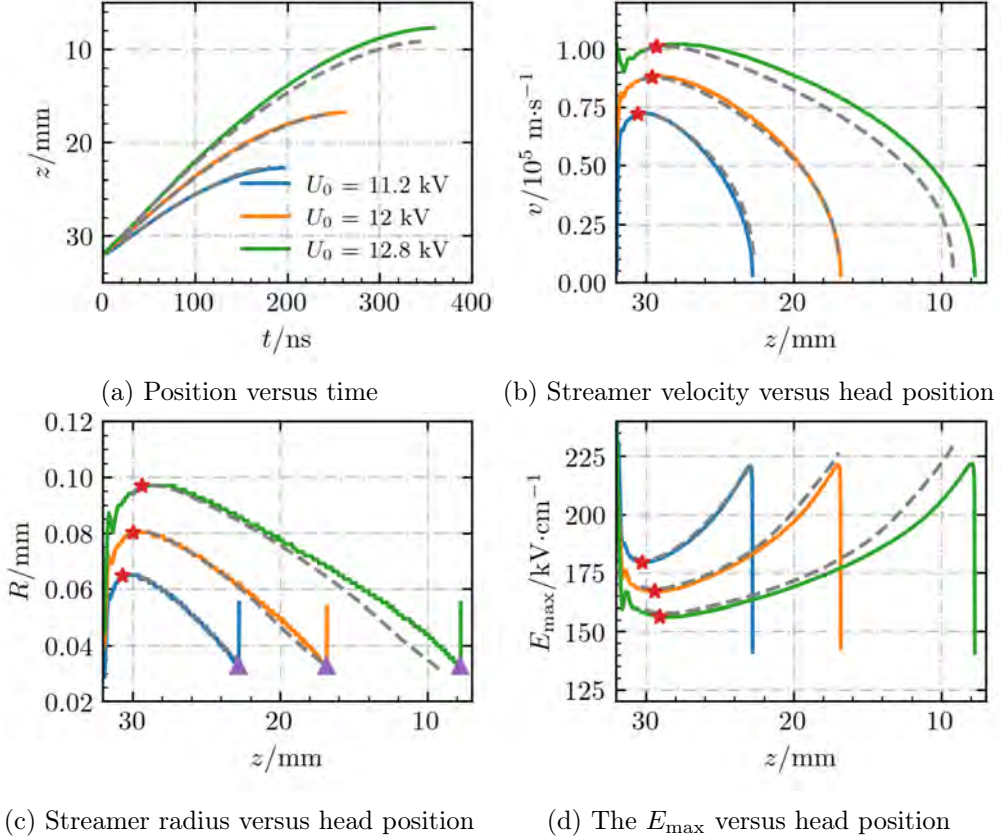

(a) Position versus time

(b) Streamer velocity versus head position

(c) Streamer radius versus head position

(d) The E_{max} versus head position

Figure 4.12: Stagnating streamers in air for applied voltages of 11.2 kV, 12 kV and 12.8 kV. The results of axisymmetric fluid simulations are indicated by solid lines. Solutions of the phenomenological model given by equation (4.10) are indicated by dashed lines, using $\tau = 38.7$ ns, $\tau_r = 2\tau$ and $R_{min} = 26\,\mu$m. The red stars indicate the locations where the background field is equal to $E_{steady}(v)$ (panel b), $E_{steady}(R)$ (panel c) and $E_{steady}(E_{max})$ (panel d). Here $E_{steady}(v)$ is the background field corresponding to steady propagation as a function of v (see figure 4.7), and similarly so for $E_{steady}(R)$ and $E_{steady}(E_{max})$. The purple triangles indicate stagnation points.

With a higher applied voltage, the radius and velocity are larger whereas E_{max} is lower. However, the minimal streamer radii are around $32\,\mu$m for all cases, close to the minimal steady streamer radius in figure 4.7.

In figure 4.13, we compare temporal v, R and E_{max} data for the stagnating

streamers with data for steady states. The relations between v, R and E_{max} are similar, even though the stagnating streamers develop in lower background fields. For each of these quantities, the background field corresponding to steady propagation can be obtained from figure 4.7, so that we have functions $E_{steady}(v)$, $E_{steady}(R)$ and $E_{steady}(E_{max})$. In figure 4.12, we have marked the locations where the actual background field is equal to $E_{steady}(v)$, $E_{steady}(R)$ and $E_{steady}(E_{max})$. Note that at these locations the time derivatives of the respective quantities are approximately zero, as is the case for steady propagation. In conclusion, the results obtained for steady streamers can help to predict whether a streamer with given properties accelerates or decelerates, with continued deceleration leading to stagnation.
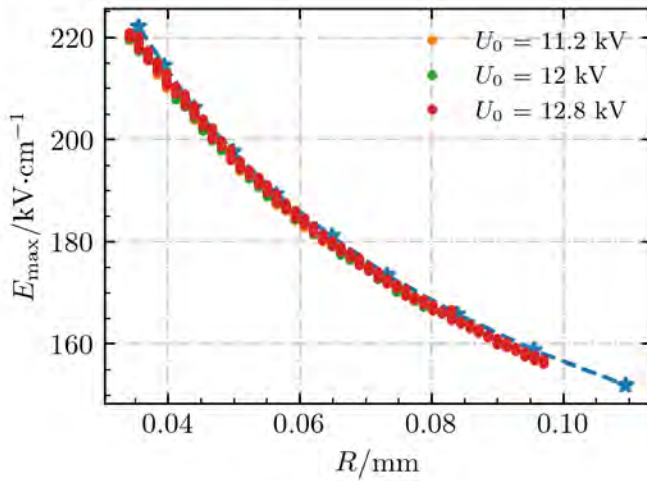
(a) The maximum electric field versus the streamer radius
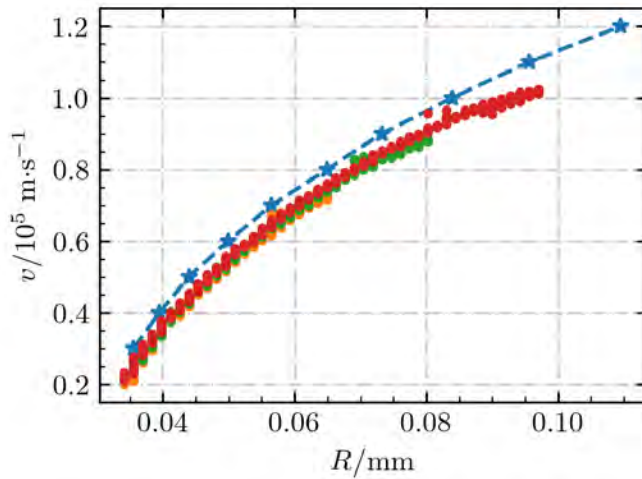
(b) The streamer velocity versus the streamer radius
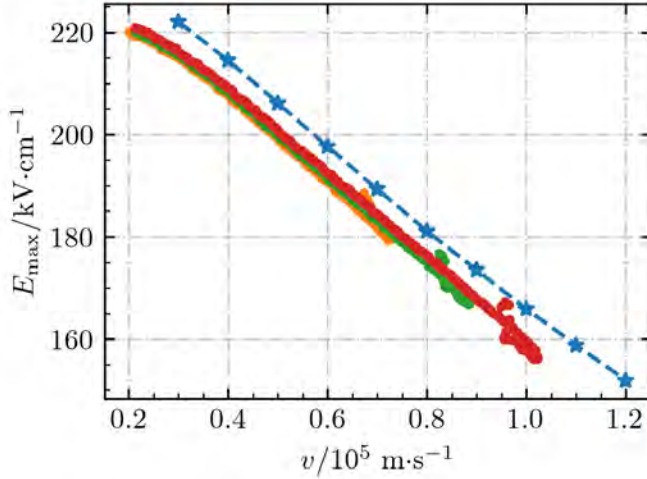
(c) The maximum electric field versus the streamer velocity

Figure 4.13: Data for the stagnating streamers shown in figure 4.12, with each data point corresponding to a different time. Curves for steady streamers (blue dashed lines) are shown for comparison.

4.4.2   A phenomenological model for stagnating streamers

The deceleration of a streamer depends on multiple properties, e.g., its current velocity, radius and the background electric field. To quantify this deceleration, we now construct a fitted model for stagnating streamers. This model is based on their similarity to the steady streamers studied in section 4.3, so we start from equation (4.6). For the data shown in figure 4.7, $E_{\max}$ can empirically be expressed in terms of the streamer radius as

$$E_{\max}(R) = c_0 R^{-1/3} = 7.25 \times 10^5 \left(\frac{1\,\text{m}}{R}\right)^{1/3} \text{V/m}, \tag{4.7}$$

with an error below 1%. Plugging this into equation (4.6) gives $\tau = c_0 R^{2/3}/(v E_{\text{bg}})$. Solving for v and R gives the following expressions

$$v^* = c_0 R^{2/3}/(E_{\text{bg}}\tau), \tag{4.8}$$

$$R^* = (E_{\text{bg}}\tau v/c_0)^{3/2}. \tag{4.9}$$

We know that streamers satisfying these equations, for a certain value of τ, keep the same radius and velocity. A simple coupled differential equation that also satisfies these properties is

$$\partial_t v = (v - v^*)/\tau_r,$$
$$\partial_t R = (\max[R^*, R_{\min}] - R)/\tau_r, \tag{4.10}$$

with v^* and R^* given as above, τ_r a relaxation time scale and $R_{\min}$ a minimal radius. If we fit this model to the stagnating streamer data, rather good agreement is obtained for $\tau = 38.7$ ns, $\tau_r = 2\tau$ and $R_{\min} = 26\,\mu$m, which all seem reasonable. Solutions for these parameters are shown as dashed lines in figure 4.12. These solutions start at $t = 20$ ns and they take the spatial dependence of the background field into account. The relatively good agreement suggests that equation (4.10) can be useful to describe the deceleration of a streamer.

4.4.3 Stability field

We now consider the relation between the streamer length and the concept of a stability field. The streamer stability field is usually defined as $E_{\mathrm{st}} = V_0/d$, where V_0 is the applied voltage at which a streamer is just able to cross a discharge gap of width d [6, 43, 45, 46]. This concept can in principle also be applied to streamers that do not cross the gap, with a length $L_s < d$. A commonly used empirical equation, see e.g. [102, 160], is

$$\int_0^{L_s} (E_{\mathrm{bg}}(z) - E_{\mathrm{st}})\, dz = 0, \tag{4.11}$$

where E_{bg} is the background electric field and the line from $z = 0$ to $z = L_s$ corresponds to the streamer's path. Equation (4.11) can also be written in terms of the background electric potential $\phi_0(z)$ as $E_{\mathrm{st}} = (\phi_0(0) - \phi_0(L_s))/L_s$.

For the stagnating streamers at applied voltages of 11.2, 12.0 and 12.8 kV, the corresponding values of E_{st} are 5.18, 4.54 and 4.27 kV/cm. These values are in the range of typical observed stability fields. For a higher applied voltage E_{st} is lower, because a faster streamer forms, in agreement with the results of section 4.3. By using a lower bound for E_{st}, equation (4.11) can give an upper bound for the streamer length. If we use $E_{\mathrm{st}} = 4.1$ kV/cm, as found in section 4.3, the maximal lengths are 16, 21 and 27 mm for applied voltages of 11.2, 12.0 and 12.8 kV. For comparison, the actual observed lengths are 9.2, 15.1 and 24.2 mm, respectively.

The analysis above was based on the background electric field. In contrast to experimental studies, we can also determine the average electric field inside the streamer channel $\overline{E}_{\mathrm{ch}}$ in our simulations, including space charge effects. We measure $\overline{E}_{\mathrm{ch}}$ as the average field between the electrode and the location where the streamer's electric field has a maximum. In other words, $\overline{E}_{\mathrm{ch}} = (\phi_0(0) - \phi(z,t))/L_s$, where z and t are the stagnation location and time, respectively. This results in average fields of 3.22, 3.36 and 3.52 kV/cm for applied voltages of 11.2, 12.0 and 12.8 kV. These values are significantly lower than the stability fields determined above because they are based on the electrically screened part of the channel. We can relate $\overline{E}_{\mathrm{ch}}$ and E_{st} by considering the potential difference induced by the streamer head, here denoted as $\delta\phi(z,t) = \phi(z,t) - \phi_0(z)$. It then

follows that

$$\delta\phi(z,t) = L_s \left(E_{\mathrm{st}} - \overline{E}_{\mathrm{ch}} \right). \tag{4.12}$$

For applied voltages of 11.2, 12.0 and 12.8 kV, the corresponding values of $\delta\phi$ are 1.81, 1.79 and 1.80 kV. Note that when a streamer crosses a discharge gap, the head potential is zero, so that $E_{\mathrm{st}} = \overline{E}_{\mathrm{ch}}$.

In previous work $\overline{E}_{\mathrm{ch}}$ has been used as a measure of the stability field E_{st}, even for streamers not crossing the gap [6, 7, 161]. Our results show that $\overline{E}_{\mathrm{ch}}$ and E_{st} can differ significantly. However, according to equation (4.12) $\overline{E}_{\mathrm{ch}}$ and E_{st} converge for large streamer length, if one assumes a finite head potential. Finally, we remark that the value of $\overline{E}_{\mathrm{ch}} = (\phi_0(0) - \phi(z,t))/L_s$ depends on z. We have here used the location corresponding to the maximal electric field. Placing z behind the charge layer of the streamer head reduces $\overline{E}_{\mathrm{ch}}$, whereas placing it further ahead increases $\overline{E}_{\mathrm{ch}}$, due to the large field around the streamer head.

4.5   Conclusions

We have studied the properties of steady and stagnating positive streamers in air, using an axisymmetric fluid model. Streamers with constant velocities were obtained by initially adjusting the applied voltage based on the streamer velocity. Our main findings are listed below.

1. Positive streamers with constant velocities between 1.2×10^5 and 3×10^4 m/s could be obtained in background electric fields from 4.1 kV/cm to 5.4 kV/cm. This range corresponds well with experimentally determined stability fields.

2. The steady streamers are not actually stable, in the sense that a small change in their properties will eventually lead to either acceleration or deceleration.

3. The effective length of a streamer can be described by $v\tau$, where v is the streamer velocity and τ a time scale for the loss of conductivity in the streamer channel. A faster streamer has a longer effective length, and can therefore propagate in a lower background electric field than a slower one.

4. For the steady streamers, the ratio between radius and velocity is about $R/v \sim 0.95 \pm 0.2$ ns and the ratio between the maximal field at the streamer head and the background field is about $E_{\mathrm{max}}/E_{\mathrm{bg}} \sim 40 \pm 2$. However, there is no clear linear trend between these variables. To a good approximation, $E_{\mathrm{max}} \propto R^{-1/3}$.

5. The radius, velocity, maximal electric field and background electric field of steady streamers can be related to the conductivity loss time scale τ as $\tau = RE_{max}/vE_{\mathrm{bg}}$. In air, the obtained values of τ range from 33 to 49 ns.

6. In N$_2$-O$_2$ mixtures with less O$_2$ than air, steady streamers require lower background electric fields, due to reduced attachment and recombination rates that result in a longer effective length.

7. By using a correction factor for the impact ionization source term and by including ion motion, it was possible to simulate stagnating streamers without an unphysical divergence in the electric field.

8. If a streamer forms near a sharp electrode and then enters a low background field, it will first accelerate, then decelerate, and eventually stagnate. The transition between acceleration and deceleration occurs close to the background electric field corresponding to steady propagation. The relationships between v, R and E_{max} for decelerating streamers are similar to those of steady streamers.

9. A phenomenological model with fitted coefficients was presented to describe the velocity and radius of decelerating streamers, based on the properties of steady streamers.

10. For a streamer that has stagnated, the average background electric field between the streamer head and tail resembles the empirical stability field. The average electric field inside the streamer channel can be significantly lower, in particular for relatively short streamers.

Chapter 5

A computational study of streamers interacting with dielectrics

We employ numerical simulations to study the dynamics of surface discharges, which are common in high-voltage engineering. Our simulations involve streamer discharges propagating towards a dielectric surface, attaching to it, and then propagating over the surface using a 2D fluid model. Key findings revealed that streamers are mainly attracted to dielectrics through electrostatic forces. Compared to gas streamers, surface streamers exhibited smaller radii, higher electric fields, and greater electron densities, resulting in faster propagation velocities. For positive surface streamers, a cathode sheath with a high electric field and low electron density exists between the streamer head and the dielectric surface, while negative surface streamers can touch the surface, creating a high-field area inside the dielectric. Several parameters were explored, including applied voltage, dielectric permittivity, secondary electron emission, positive ion mobility, and preset surface charges. A higher applied voltage increased streamer velocities for both positive and negative polarities. Positive streamers in dielectrics with higher permittivity showed accelerated formation of surface streamers, while negative streamers in such conditions experienced slower development. Electron emission from dielectric surfaces hardly increases the velocity of positive surface streamers, mainly due to the relatively strong photoionization in air. Preset positive surface charge accelerates the development of negative streamers around dielectrics, whereas negative surface charge delays or inhibits the development of negative surface discharges. Additionally, we performed 3D particle simulations for positive surface discharges to compare with the 2D fluid model. Observations revealed the presence of

both surface and gas-phase streamer components in the 3D model, with the width of the cathode sheath between the surface component and the dielectric being similar in both 3D and 2D simulations.

The content in sections 3 and 4 of this chapter is adapted from:

[1] Xiaoran Li, Anbang Sun, Guanjun Zhang and Jannis Teunissen. A computational study of positive streamers interacting with dielectrics. *Plasma Sources Science and Technology*, 29(6): 065004, 2020.

[2] Xiaoran Li, Anbang Sun and Jannis Teunissen. A computational study of negative surface discharges: Characteristics of surface streamers and surface charges. *IEEE Transactions on Dielectrics and Electrical Insulation*, 27(4): 1178-1186, 2020.

The introduction and simulation methods sections from the two published papers have been merged and included in chapter 1 and chapter 2 of this thesis, as well as sections 1 and 2 of the current chapter.

The content in section 5 of this chapter contains the latest and unpublished results.

5.1 Introduction

Electric discharges in electronic devices and HV (high-voltage) equipment often occur along dielectric materials. In the regions of HV stress around an insulator, electron avalanches and streamer discharges can develop. These partial discharges may eventually result in electrical breakdowns of the insulator. A dielectric present in the vicinity of the electrodes not only modifies the fields between the electrodes, but also serves as a possible source or sink of electrons during the breakdown process. Studying the interaction between dielectrics and streamer discharges is therefore important for understanding breakdown along surfaces.

Our focus is on a specific geometry: a flat dielectric placed between parallel-plate electrodes. This geometry resembles practical HV insulation applications, such as insulators inserted between HV and ground electrodes in gas-insulated switchgears [63, 80]. We simulate streamers interacting with dielectrics, including discharge inception, attachment to the dielectric and propagation over the surface.

The content of this chapter is as follows. The simulation model is described in section 5.2. In sections 5.3 and 5.4, we focus on the interaction between dielectrics and positive streamers and, respectively, negative streamers. In the subsections of section 5.3 and 5.4, we study the characteristics of surface streamers compared to gas-phase streamers, and investigate the effects of several discharge parameters on the streamer's inception time, propagation velocity and morphology. In section 5.5, 3D particle simulations are performed for positive surface discharges to compare with results from 2D fluid simulations.

5.2 Simulation Model

A 2D fluid model based on `afivo-streamer` is used in this chapter. We have made several modifications to be able to simulate surface streamers:

- Electrons, ions and photons can be absorbed by dielectric surfaces.

- Surface densities and fluxes are stored separately from their equivalents in the gas.

- The electric field computation takes into account the nonuniform dielectric permittivities and the surface charge at the interface.

- A new Monte Carlo photoemission module is implemented, and the photoionization routines are adjusted to account for the dielectric.

5.2.1   Fluid Model

We use a 2D drift-diffusion-reaction type fluid model with the local field approximation as introduced in chapter 2. We here use a relatively simple source term

$$S = S_i + S_a + S_{\text{ph}} + S_{\text{se}}, \tag{5.1}$$

where S_i is the electron impact ionization source term, S_a the electron attachment, S_{ph} the photoionization and S_{se} the secondary electron emission due to the impact of both ions and photons. The electron impact ionization and electron attachment terms are given by $S_i = \alpha\mu_e|\mathbf{E}|n_e$ and $S_a = \eta\mu_e|\mathbf{E}|n_e$, respectively, where α and η are the ionization and attachment coefficients. Electron transport and reaction coefficients for air (1 bar, 300 K) were generated with Monte Carlo particle swarm simulations (see e.g. [120]), using Phelps' cross sections [115]. In this chapter, these coefficients are tabulated up to a certain maximum electric field, which is here 35 kV/mm; for higher fields, we use the tabulated value at 35 kV/mm. The positive ion mobility $\mu_i^+ = 3 \times 10^{-4}\,\text{m}^2/\text{Vs}$ is here considered to be constant, but in section 5.3.5 it is varied to investigate its effect on surface discharges. For simplicity, the negative ion mobility is set to zero ($\mu_i^- = 0$) throughout the chapter.

   We assume that electrons and ions attach to the surface when they flow onto a dielectric. They do not move or react on the surface, but secondary electron emission from the surface is taken into account. For the impact of positive ions, a SEE (secondary electron emission) coefficient γ_i is used. When a photon hits a dielectric surface, we assume that the photon is absorbed. A SEE photoemission coefficient γ_{pe} is used to determine the photoemission flux, see section 5.2.2. The effect of these SEE coefficients is studied in section 5.3.4, elsewhere they are set to zero. The secondary electron emission source term S_{se} is non-zero only in cells adjacent to the dielectric surface. In these cells, it is given by

$$S_{\text{se}} = -\nabla \cdot (\tilde{\mathbf{\Gamma}}_{\text{pe}} - \gamma_i\tilde{\mathbf{\Gamma}}_i^+) \tag{5.2}$$

   where $\tilde{\Gamma}_i^+$ is the flux of positive ions onto the surface, and $\tilde{\Gamma}_{\text{pe}}$ is the photoemission flux coming from the surface. By definition, both these fluxes are non-zero only at the surface.

   Secondary emission leaves behind positive surface charge on the dielectric. Therefore, the surface charge density σ_s changes in time as

$$\partial_t\sigma_s = -e(\tilde{\Gamma}_e + \tilde{\Gamma}_i^-) + e(1 + \gamma_i)\tilde{\Gamma}_i^+ + e\tilde{\Gamma}_{pe}, \tag{5.3}$$

where e is the elementary charge and the other terms correspond to the fluxes onto the dielectric surface: $\tilde{\Gamma}_e$ for electrons, $\tilde{\Gamma}_i^-$ for negative ions, $\tilde{\Gamma}_i^+$ for positive ions, and $\tilde{\Gamma}_{pe}$ for photon electrons. We calculate fluxes on the gas-dielectric interface in the same way as fluxes in the bulk gas, which may not always be accurate [162]. However, we expect that this approximation, which was also used

in e.g. [80, 163, 164], has no strong effect on the transient (non-equilibrium) simulations presented here.

For positive streamers, secondary electron emission (SEE) from a dielectric can be important, because these electrons can start avalanches growing towards the streamer head. For negative streamers, electrons move away from the streamer head, so that SEE electrons released from the dielectric would immediately flow back onto it. SEE from dielectrics is therefore neglected for negative streamers in this chapter. We remark that SEE could play a role in the initiation of negative streamers (for example through surface charge accumulation), but that is outside the scope of the present thesis.

5.2.2   Photoionization and Photoemission

Positive streamer discharges need a source of free electrons ahead of them in order to propagate. Photons can generate such free electrons through photoionization in the gas or photoemission from a dielectric surface. In N_2–O_2 mixtures, non-local photoionization can take place when an excited nitrogen molecule emits a UV photon in the 98 to 102.5 nm range, which has enough energy to ionize an oxygen molecule. The role of photoemission in surface discharges is less well understood. Photons can be emitted from several excited states. The probability of photoemission not only depends on the photon energy, but also on the surface properties [69]. For simplicity, we consider only two types of photons here: high-energy photons, which can generate photoionization and photoemission, and low-energy photons, which can only contribute to photoemission and are not absorbed in the gas. These processes are illustrated in figure 5.1.
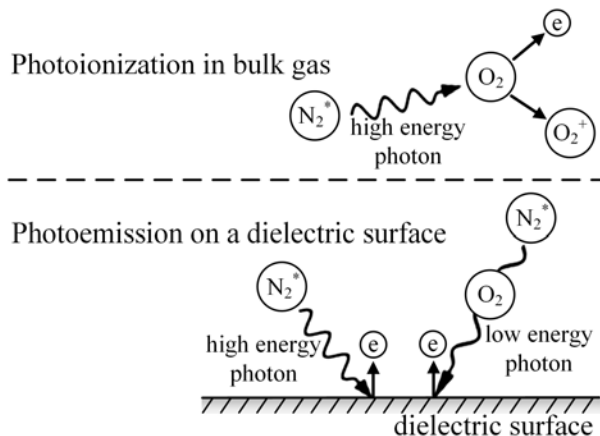
Figure 5.1: Illustration of photoionization and photoemission mechanisms in air. Two types of photons are considered. High-energy photons can generate photoionization and photoemission, whereas low-energy photons are not absorbed by the gas and only contribute to photoemission.

Photoionization and photoemission are here modeled with a Monte Carlo (MC) method. The idea is to approximate the photoionization source term S_{ph} and the photon flux onto the dielectric $\tilde{\Gamma}_{pe}$ by randomly sampling discrete photons. For computational efficiency, these terms are updated every $\Delta t_\gamma = 10\Delta t$, where Δt is the time step used for solving equation (2.1).

First, the number of ionizing (high-energy) photons produced per grid cell during a time Δt_γ is determined. We use Zheleznyak's model [89], in which the number of ionizing photons is proportional to the number of impact ionization events, as shown in equation (2.13). The corresponding proportionality factor is set to $\xi p_q/(p + p_q)$, where We remark that ξ should in principle depend on the electric field [89], but that it is here approximated by a constant $\xi = 0.05$, as in [38]. Per cell, a random number is drawn to determine how many photons are generated, see [139].

Since simulations are here performed in 2D, the discrete photons do not correspond to (single) physical photons. Instead, the total photon number $N_{photons}$ is fixed, so that the MC method always uses 10^5 photons. The weight factor w of these photons is given by $w = \int S_\gamma dV/N_{photons}$, where

$$\int S_\gamma dV = \xi p_q/(p + p_q) \int S_i dV, \tag{5.4}$$

is the volume-integrated production rate of ionizing photons.

For simplicity, the number of produced low-energy photons is assumed to be equal to the number of high-energy photons. As the low-energy photons only contribute to photoemission, their effect can be controlled through the corresponding photoemission coefficient.

Second, an isotropically distributed direction is sampled for each photon. Afterwards, absorption lengths are determined. The absorption length of high-energy photons is sampled from the absorption function for air, see e.g. [38]. Low-energy photons are not absorbed by the gas, so their absorption length is set to a large value, making sure they always end up outside the computational domain.

Third, we determine which photons hit a dielectric surface, and where they do so. These photons are absorbed by the surface, where they contribute to the local photoemission flux $\tilde{\Gamma}_{pe}$. For the low-energy and high-energy photons, photoemission coefficients γ_{peL} and γ_{peH} are used, respectively. If a surface cell of area ΔA is hit by n_L and n_H low-energy and high-energy photons, then

$$\tilde{\Gamma}_{pe} = (\gamma_{peL}n_L + \gamma_{peH}n_H)w/\Delta A. \tag{5.5}$$

The effect of photoemission is investigated in section 5.3.4; elsewhere in this chapter photoemission is not taken into account (so that $\gamma_{peL} = \gamma_{peH} = 0$).

Fourth, the remaining high-energy photons that are absorbed in the gas contribute to photoionization source term S_{ph}. If n_γ photons are absorbed in a grid

cell with volume ΔV, then

$$S_{\mathrm{ph}} = n_\gamma w / \Delta V. \qquad (5.6)$$

Low-energy photons and high-energy photons that are absorbed outside the computational domain have no effect.

5.2.3   Computational domain and initial conditions

The geometry we use consists of a flat dielectric placed between two parallel-plate electrodes, as shown in figure 5.2. This geometry resembles some actual HV insulation applications, and its simplicity makes it suitable for numerically studying surface discharges. The computational domain measures $(40\,\mathrm{mm})^2$, and the dielectric is placed on the left side with a width of 10 mm. A constant high voltage is applied at the upper electrode, and the lower electrode is grounded. Neumann zero boundary conditions are applied on the left and right sides for electric potential.

The gas is artificial air (80% N_2 and 20% O_2) at 1 bar and 300 K. The background densities of electrons and positive ions are set to 10^{10} m^{-3} [165]. Discharges usually start in regions where the electric field is locally enhanced. In actual HV devices, the electric field is often enhanced at a triple junction between gas, dielectric and electrode. A realistic description of discharge inception (due to e.g. partial discharges and surface charge accumulation) is outside the scope of the present chapter. Instead, an ionized seed is placed near the upper triple junction to enhance the electric field locally, as indicated in figure 5.2. The ionized seed is about 2 mm long with a radius of about 0.4 mm. The electron and positive ion density are 5×10^{18} m^{-3} at the center, and they decay at distances above $d = 0.2$ mm with a so-called smoothstep profile: $1 - 3x^2 + 2x^3$ up to $x = 1$, where $x = (d - 0.2\,\mathrm{mm})/0.2\,\mathrm{mm}$. When the electrons from a seed drift upwards, the electric field at the bottom of the seed is enhanced so that a streamer can start.

The minimum grid spacing Δx used for the adaptive mesh is about 1.2 μm. The mesh refinement depends on the local ionization coefficient α, ensuring that $\Delta x < 1/\alpha$.

5.3   Interaction between positive streamers and dielectrics

To investigate the interaction between positive streamers and dielectrics, the following parameter values are used unless indicated otherwise: an applied voltage of 100 kV, a relative permittivity of the dielectric (ε_r) set to 2, a positive ion mobility (μ_i^+) of 3×10^{-4} m$^2 \cdot$V$^{-1} \cdot$s^{-1}, and no electron emission from the dielectric. In section 5.3.1, the initial seed is placed at different distances from the dielectric to study how the streamer-dielectric interaction affected by the streamer inception position. We also point out the main differences between surface and gas
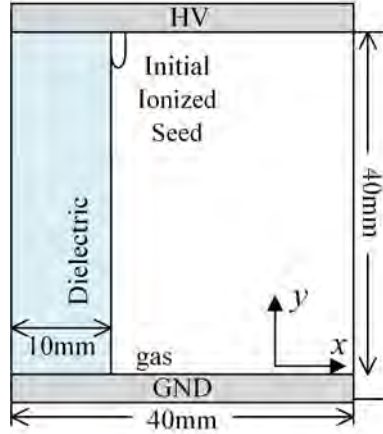
Figure 5.2: The computational domain. A parallel-plate geometry is used, with a flat dielectric present on the left. Discharges start from the ionized seed present close to the top electrode, as described in the text.

streamers. Next, we systematically study the effect of several parameters on the surface discharges: the applied voltage (section 5.3.2), the dielectric permittivity (section 5.3.3), the secondary electron emission coefficients (section 5.3.4), and finally the ion mobility (section 5.3.5). The parameters investigated and their values in each section are shown in table 5.1.

Table 5.1: Investigated parameters and their values in each section. Here d is the distance between the seed center and the dielectric; U the applied voltage; ε_r the relative permittivity of the dielectric; γ_i the ion-induced secondary electron emission coefficient; γ_{pe} the photoemission coefficient and μ_i^+ the positive ion mobility.

Section	d/mm	U/kV	ε_r	γ_i	γ_{pe}	μ_i^+/m^2·V^{-1}s^{-1}
5.3.1	$0.5, 1, 2, 5$	100	2	0	0	3×10^{-4}
5.3.2	0.5	$92, 100, 112$	2	0	0	3×10^{-4}
5.3.3	0.5	100	$2, 3, 5$	0	0	3×10^{-4}
5.3.4.1	0.4	100	2	$0, 0.5$	0	3×10^{-4}
5.3.4.2	$0.5, 1$	100	2	0	$0, 0.5$	3×10^{-4}
5.3.5	0.5	100	2	0	0	$(0, 1, 5, 10) \times 10^{-4}$

5.3.1   Streamer-dielectric interaction

Previous experiments have revealed that dielectrics attract positive streamers, see e.g. [58, 59]. This attraction is also present in our numerical model. Figure

5.3 shows the evolution of the electron density for an initial ionized seed placed 1 mm away from the dielectric. It can be seen that the streamer starts to grow in air and then gradually develops towards the dielectric. After connecting with the dielectric, the streamer propagates down over its surface. The evolution shown here is in qualitative agreement with the discharge photographs in [58].

To study the streamer-dielectric attraction, we have placed the initial ionized seed at different distances from the dielectric. Figures 5.4 a–d show the electron density for seeds placed at 0.5 mm, 1 mm, 2 mm and 5 mm from the dielectric. For comparison, the electron density for a streamer in bulk gas is also shown in figure 5.4e. In this simulation the dielectric was removed, so that the whole computational domain contained gas, and the initial seed was placed at $x = 20$ mm. Figure 5.4a shows the electron density at 15 ns, for the other cases, which develop more slowly, results at 20 ns are shown. The closer the streamer is located to the dielectric, the stronger the attraction to the dielectric becomes. It can also be seen that a nearby dielectric increases the streamer's velocity in the gas, and that streamers here propagate faster on the surface than in the gas.
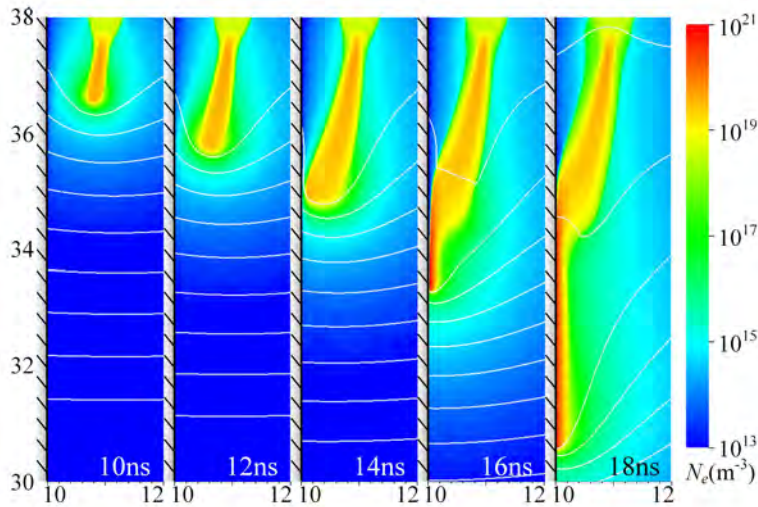
Figure 5.3: The streamer development process between 10 ns and 18 ns for seed placed at 1 mm from the dielectric. White equipotential lines spaced by 2 kV are shown in part of the domain.

Attraction to the dielectric   As photoemission is disabled here (see table 5.1), the attraction of the streamer to the dielectric is purely electrostatic. The net charge in the streamer head polarizes the dielectric, which increases the electric field between the streamer and the dielectric. This effect is illustrated in figure 5.5, which shows the horizontal electric field (E_x) around the streamer heads. With a dielectric present, $|E_x|$ increases on the dielectric side, and it is
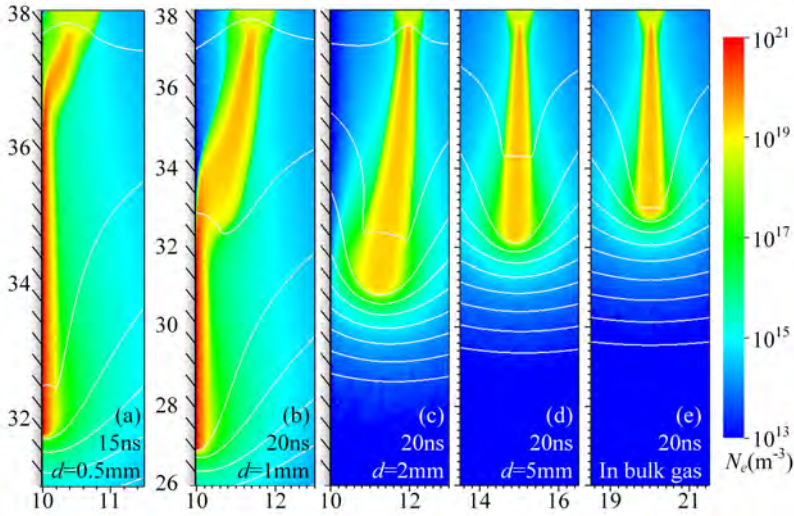
Figure 5.4: The electron density for streamers starting from different locations. For panels a-d, the initial seed was placed at $0.5\,mm$, $1\,mm$, $2\,mm$ and $5\,mm$ from the dielectric. For comparison, a streamer in bulk gas is shown in panel e. Results are shown at $20\,ns$, except for panel a, which has the fastest propagation. White equipotential lines spaced by 2 kV are shown in part of the domain.

reduced on the other side. The closer the streamer is to a dielectric, the stronger this effect becomes. Eventually, the streamer will turn into a surface streamer. As shown in figure 5.4, such a surface streamer is thinner and quite asymmetric compared to a gas streamer.

In past research, the attraction of streamers to dielectrics could often be explained by the enhanced static field between pointed electrodes and dielectrics, see e.g. [58, 60]. In contrast, the attraction to the dielectric is here due to the space charge from the streamer itself, since in our plate-to-plate geometry, the electric field has no horizontal component before a discharge is present. Assuming that streamers propagate approximately along electric field lines [142], we can therefore state that streamers lead themselves to the dielectric: their space charge modifies the background field and causes a horizontal field component that attracts them to the dielectric.

Surface charge on the dielectric could also play a role in attracting streamer discharges, by modifying the background electric field. However, there is negligible surface charge here, as secondary electron emission is disabled in this section and electrons move away from the dielectric. Positive ions do move towards the dielectric, but there are initially few of them near the dielectric, and they drift with a relatively low mobility, so that they hardly contribute to the surface charge.
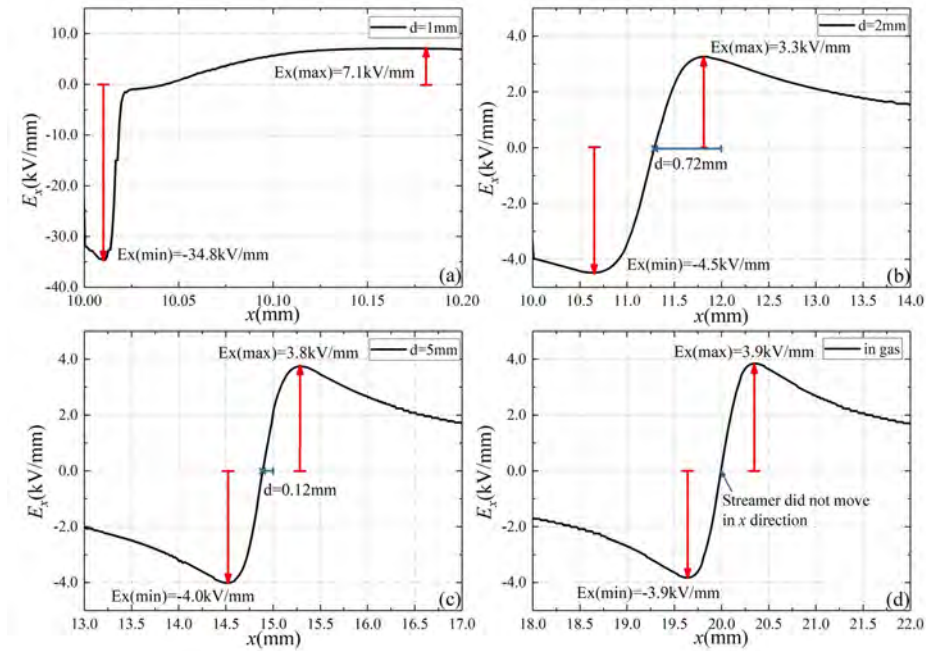
Figure 5.5: Horizontal electric field (E_x) at 20 ns for streamers starting from different locations. The curves are taken at the streamer head, at the height of the maximum electric field.

Effect on streamer velocity Several experimental studies have found that surface discharges are faster than bulk gas streamers [59, 62, 166]. Their increased velocity was attributed to increased ionization rates near the dielectric, accumulated negative charge and electron emission from the dielectric surface. Electron emission from the dielectric is not included here (it is in section 5.3.4), but we still find that the surface streamers are significantly faster. Figure 5.6 shows the streamer velocity and its maximal electric field for the case $d = 1$ mm. Note that both the velocity and the maximal electric field increase when the surface streamer forms, at around $y = 35$ mm. Even though the higher field is mostly in the horizontal direction, see figure 5.5, it still contributes to a faster vertical growth.

As can be seen in figure 5.4, the electron density inside a surface streamer ($\sim 10^{20}$ to 10^{21} m^{-3}) is higher than in a gas streamer ($\sim 10^{19}$ m^{-3}) when the discharge conditions are otherwise similar. This was also observed in for example [82]. We remark that besides the presence of a dielectric, the electron density inside a streamer discharge also depends on other factors, such as the applied voltage, the streamer radius, the gas composition, and the amount of photoionization. Also note that we use a Cartesian 2D model, in which there is less field enhancement around the streamer heads than in full 3D, reducing the electron

density in both surface and gas streamers.
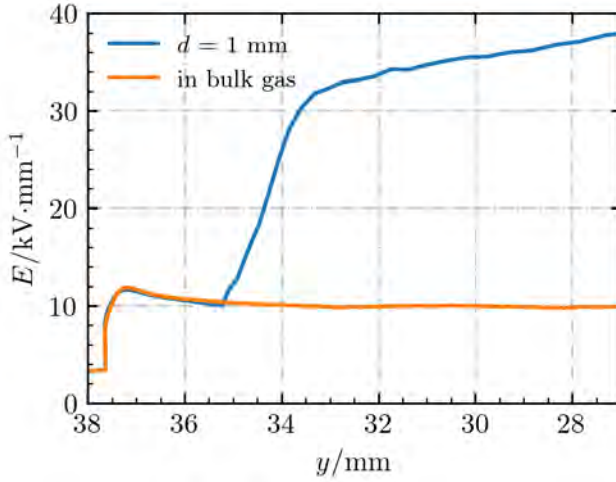
(a) The maximum electric field
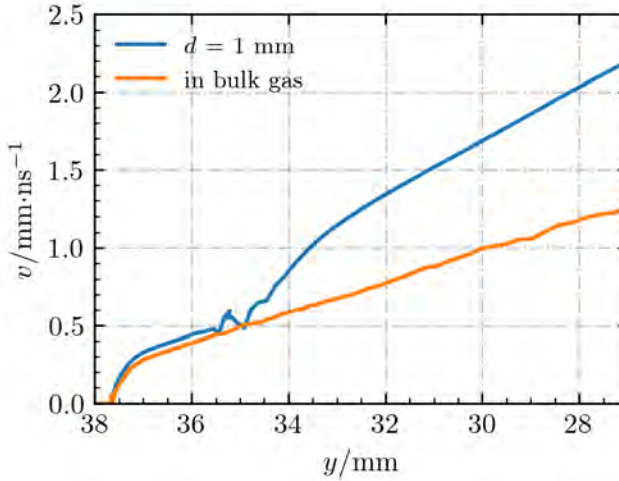
(b) The streamer velocity

Figure 5.6: The maximum electric field and streamer velocity versus the vertical position of the streamer head.

There seem to be several related effects that lead to the increased surface streamer velocity. The strong electric field between a surface streamer and a dielectric pulls the surface streamer towards the dielectric. This reduces their radius (as shown in figure 5.4), and results in an asymmetric streamer head shape, which also leads to stronger electric field enhancement. The result is that the ionization rate is increased, that the streamer has a higher degree of ionization,

and that it propagates faster. This behavior is quite distinct from gas streamers, which typically propagate faster when they have a larger radius [7].

Cathode sheath As shown in figure 5.7, the surface streamer 'hovers' over the dielectric surface without fully connecting to it. This phenomenon was also observed in simulations of dielectric barrier discharges [71, 167–169], and it only occurs for positive streamers. The reason is that positive streamers grow from incoming electron avalanches, but such avalanches require sufficient distance before they reach ionization levels comparable to the discharge. Positive streamers can therefore not immediately connect to the dielectric surface. Due to the net charge in the streamer head, a very high electric field is present in the narrow gap between the streamer and the dielectric. The effect of secondary electron emission on these dynamics is studied in section 5.3.4, and the role of the positive ion mobility is investigated in section 5.3.5.
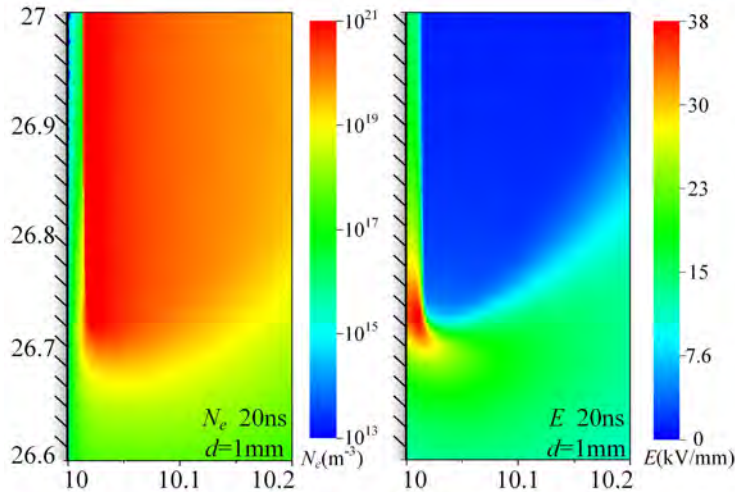
Figure 5.7: The electron density and the electric field around the positive streamer head at 20 ns, for an initial seed at 1 mm from the dielectric. Note the gap between the streamer and the dielectric.

We remark that the maximum electric field of a positive surface streamer can rapidly rise to very high values, as shown in figures 5.6a and 5.7. These high-field areas typically contain a low electron density, but they still pose a problem for plasma fluid simulations. In the present fluid simulations, the transport and reaction coefficients (e.g., the ionization coefficient or the electron mobility) are functions of the local electric field strength. These coefficients are tabulated up to a certain maximum electric field, which is here 35 kV/mm; for higher fields, we use the tabulated value at 35 kV/mm. More generally, the validity of the local field approximation is questionable when there are such high electric fields (and

corresponding strong gradients). For future studies in such ultra-high electric fields, particle-in-cell simulations could therefore be more suitable, as was also observed in [81]. Finally, we remark that a potential physical limitation for this maximum electric field is field emission of electrons from the surface.

5.3.2   Effect of applied voltage

To study the effect of the applied voltage on surface discharges, we have performed simulations for applied voltages of $92\,\mathrm{kV}$, $100\,\mathrm{kV}$ and $112\,\mathrm{kV}$, which correspond to background electric fields of $2.3\,\mathrm{kV/mm}$, $2.5\,\mathrm{kV/mm}$ and $2.8\,\mathrm{kV/mm}$, respectively. In all cases, the initial seed was located at $0.5\,\mathrm{mm}$ from the dielectric, and the evolution up to $15\,\mathrm{ns}$ was simulated. Figure 5.8 shows the maximum electric field versus time, and figure 5.9 shows the electron density for three cases at $7\,\mathrm{ns}$ and $9\,\mathrm{ns}$.
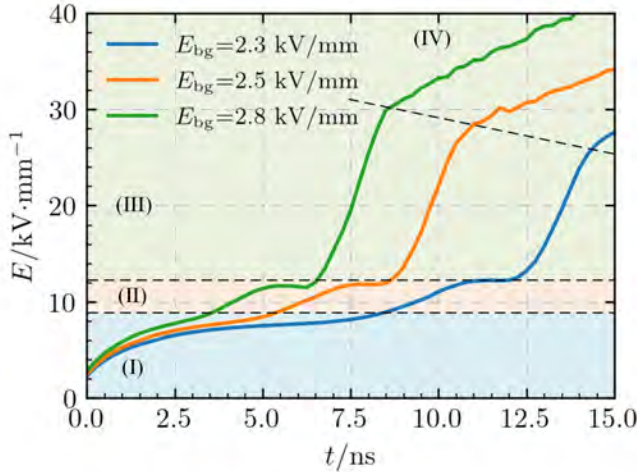
Figure 5.8: The maximum electric field versus time for streamers in background electric fields of $2.3\,\mathrm{kV/mm}$, $2.5\,\mathrm{kV/mm}$ and $2.8\,\mathrm{kV/mm}$ between. The indicated stages are I: initial stage, II: gas propagation, III: transition towards a surface streamer, IV: stable surface propagation.

Both figures reveal the following stages in the streamer's development:

1. The inception stage, in which the maximum electric field is from 0 to about $9\,\mathrm{kV/mm}$ in our setup and the streamer is hardly propagating, as shown in figure 5.9a.

2. The gas-propagation stage, in which streamers propagate in the gas with a maximum electric field below $12.5\,\mathrm{kV/mm}$. This stage is visible in figure 5.9(a) and figure 5.9(b).
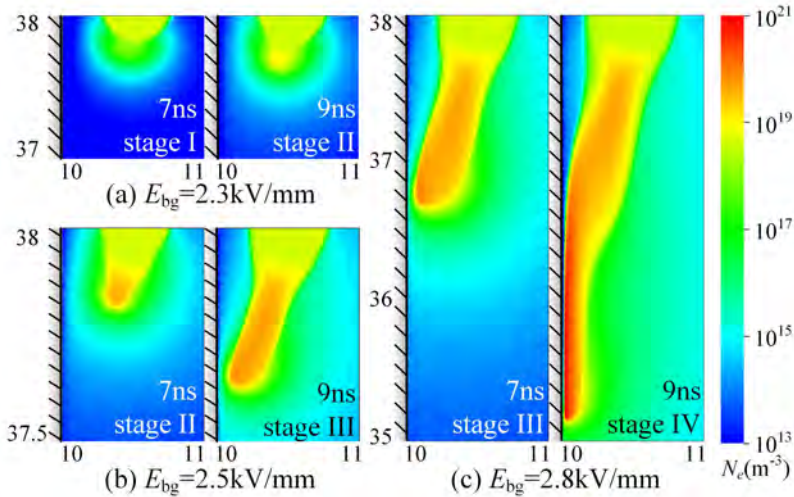
Figure 5.9: The electron density for streamers in different background electric fields (2.3 kV/mm, 2.5 kV/mm and 2.8 kV/mm) at 7 ns and 9 ns.

3. The transition stage from a gas streamer to a surface streamer, in which the maximum electric field increases sharply. The streamer also loses its rounded head shape, as shown in figures 5.9(b) and 5.9(c).

4. The surface propagation stage. The growth of the maximum electric field is slowing down, and the streamer propagates along the dielectric, as shown in figure 5.9(c).

Figure 5.8 shows that when the voltage is changed, the streamers still exhibit similar behavior in these four stages. The main difference is that the inception stage becomes shorter. For background fields of 2.3 kV/mm, 2.5 kV/mm and 2.8 kV/mm, the inception stages last 8.5 ns, 5.5 ns and 3.75 ns, respectively. The second stage also becomes slightly shorter for a higher applied voltage.

Figure 5.10 shows the streamer velocities versus their vertical location for the three applied voltages.

As expected, a higher background electric field leads to a higher streamer velocity for streamers of the same length, in agreement with the experimental results of [63].

5.3.3   Effect of dielectric permittivity

The relative permittivity ε of dielectric materials varies over a wide range. To study how ε affects surface discharges, we have performed simulations with ε set to 2, 3 and 5. As before, the initial seed was placed at 0.5 mm from the dielectric, and simulations were performed up to 15 ns.
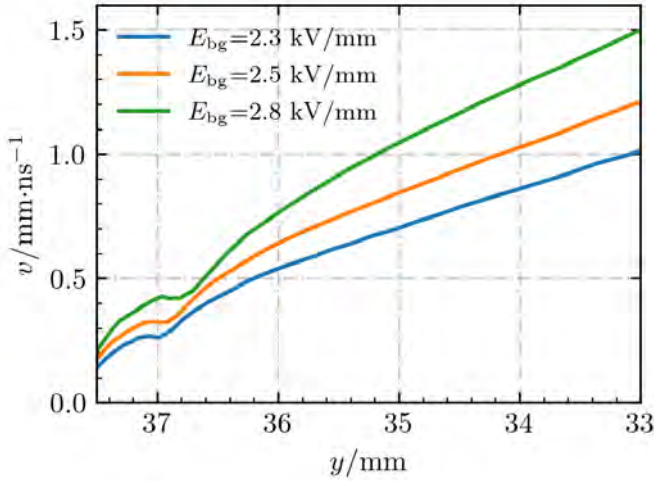
Figure 5.10: Streamer velocities versus their vertical location for different background electric fields.

The maximum electric field versus time for the three permittivities is shown in figure 5.11. The main difference we observe is that the second and third stages are shorter for a higher permittivity. A higher ε means the dielectric polarizes more strongly, which leads to a stronger attraction of streamers to the dielectric. Streamers therefore start the surface propagation stage earlier, and their maximum electric field increases more rapidly. Note that their maximum electric field is also higher during the surface propagation stage. In summary, we can conclude that a higher permittivity leads to a faster transition into a surface streamer, and a higher maximum field during the surface propagation stage.

Figure 5.12 shows the electron density for these three cases when all the streamers are at $y = 36$ mm. It can clearly be seen that the streamers attach more rapidly to the dielectric with a higher permittivity. Notice also that the surface streamer's radius is smaller wither a higher dielectric permittivity, a result of the stronger electrostatic attraction.

Figure 5.13 shows the velocity versus the streamer's vertical position for the different ε_r. The permittivity has only a small effect on the streamer's velocity, in agreement with the experimental observations of [60]. In contrast, a negative correlation between the permittivity and the streamer velocity was found in [63]. The discrepancy could come from the different geometry that was used, in which multiple surface and gas streamers propagated next to a cylindrical dielectric.

5.3.4 Effect of secondary electron emission from dielectrics

Electron emission from dielectrics may influence streamer velocities [170] and affect the high electric field in the dielectric-plasma gap [171]. In this section,
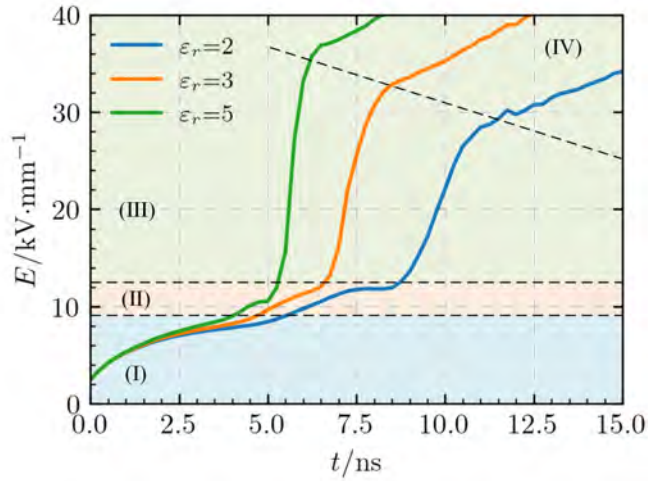
Figure 5.11: The streamers' maximal electric fields versus time for dielectrics with relative permittivities ε_r of 2, 3 and 5.
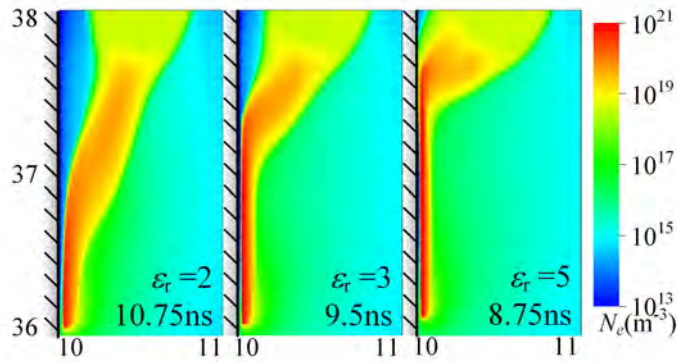
Figure 5.12: The streamers' electron density for dielectrics with relative permittivities ε_r of 2, 3 and 5. Results are shown at different times, at the moment when the streamer heads are at $y = 36$ mm.

we study how secondary electron emission affects surface streamers in our computational geometry. Both ion-induced secondary emission (ISEE) and photoemission are considered.

Ion-induced secondary electron emission

The ion-induced secondary electron emission (ISEE) yield γ_i can vary over a wide range [172–174]. Here we consider two cases, $\gamma_i = 0.5$ and $\gamma_i = 0$ (i.e., no secondary emission). In this section, the initial ionized seed's center is placed 0.4 mm away from the dielectric, so that streamers start directly next to the
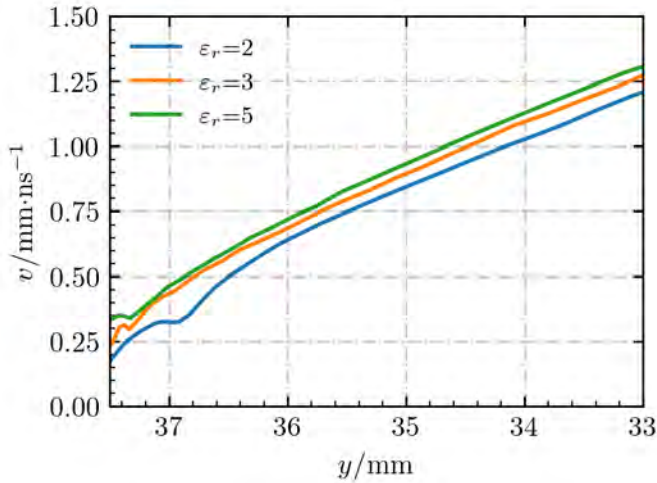
Figure 5.13: Streamer velocities versus their vertical location for different relative dielectric permittivities.

dielectric. Figure 5.14 shows the electron density and electric field distribution at 15 ns for both ISEE coefficients. It can be seen that ISEE here has little effect on the streamer length and the electric field. The electron density in the streamer-dielectric gap is slightly higher behind the head for the streamer with $\gamma_i = 0.5$, but this has negligible influence on the electric field in the gap. We can conclude that the ISEE yield hardly affects the streamer head and its propagation (the latter is mainly determined by the former). The reason for this is that positive ions have a much lower mobility than electrons. Most positive ions are generated close to the streamer head, and they will not reach the dielectric in time to affect the rapidly propagating streamer head. Most ISEE electrons are therefore released after the streamer has passed by.

Photoemission

The photo-emission coefficient γ_{pe} for typical dielectric materials varies between 10^{-4} to 10^{-1} for photon energies of 5–20 eV [175, 176]. This yield can be higher if the material contains stains or defects, or when it is negatively charged [69, 172]. The measurement of γ_{pe} of dielectrics in air is often quite challenging [177]. We here use several values for γ_{pe} to demonstrate how photoemission affects positive streamers.

As discussed in section 5.2.2, we consider low-energy and high-energy photons, with the main distinction that high-energy photons can be absorbed in the gas. The following four cases are considered for the photoemission coefficients γ_{peL} and γ_{peH} for low-energy and high-energy photons:
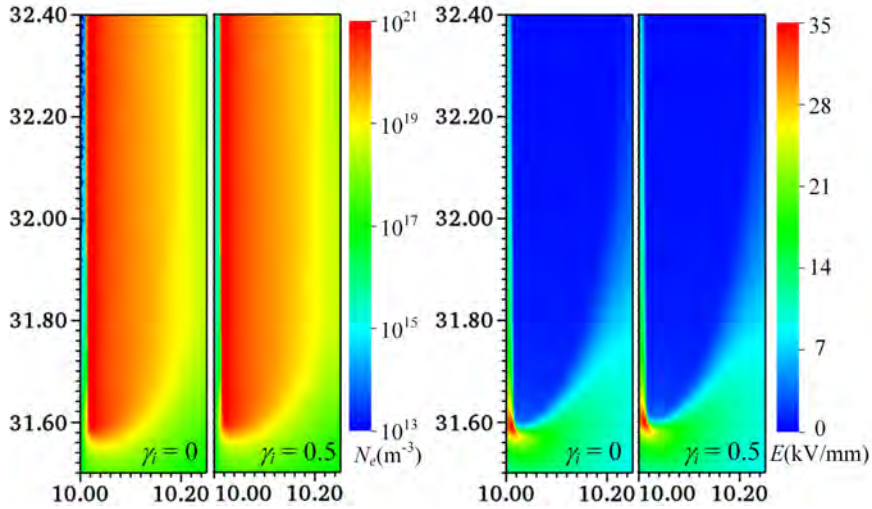
Figure 5.14: The electron density and electric field at 15 ns with the ion-induced secondary electron emission coefficient γ_i set to 0 (left) and 0.5 (right).

1. $\gamma_{\mathrm{peH}}=0$, $\gamma_{\mathrm{peL}}=0$

2. $\gamma_{\mathrm{peH}}=0.5$, $\gamma_{\mathrm{peL}}=0$

3. $\gamma_{\mathrm{peH}}=0$, $\gamma_{\mathrm{peL}}=0.5$

4. $\gamma_{\mathrm{peH}}=0.5$, $\gamma_{\mathrm{peL}}=0.5$

In the simulations, streamers start near the dielectric, with the seed placed at either 0.5 mm or 1 mm from the dielectric.

As shown in figure 5.15, photoemission by low-energy photons helps to start a discharge near a dielectric. At 5.5 ns, the $\gamma_{\mathrm{peL}} = 0.5$ cases show the streamer already bending towards the dielectric with a sharp tip, due to photoemission. However, we remark that the inception time for these four cases is the same when the seeds are placed at 1 mm away from the dielectric. The secondary electrons from the dielectric then need more time to reach the streamer, and the streamers have already started due to the photoionization they generate. We conclude that photoemission can be important for discharges close to dielectrics and for discharges in gases with less photoionization than air.

Figure 5.16a shows the electron density distribution for the above four cases at 11 ns. The streamers with $\gamma_{\mathrm{peL}} = 0.5$ are longer than the other two, since they start earlier. Photoemission also causes them to attach to the dielectric more rapidly. Another difference is that the narrow gap between streamer and dielectric is smaller with more photoemission. This happens because photoemission provides seed electrons in the gap, which allows the streamer to get closer to the dielectric. To see this more clearly, the electron density distributions at
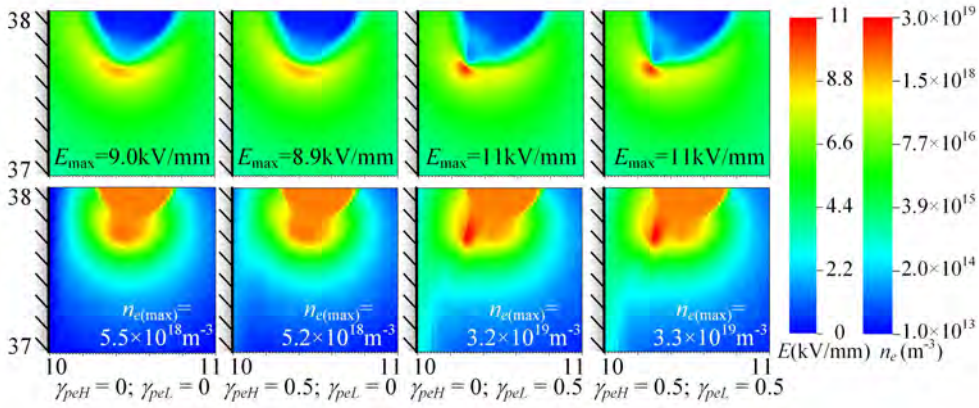
Figure 5.15: The electric field (top) and the electron density (bottom) in simulations with different photoemission coefficients for high-energy (γ_{peH}) and low-energy photons (γ_{peL}). Results are shown at 5.5 ns, when the streamer discharges start to grow.

$y = 36.4$ mm (the dashed line in figure 5.16(a) are shown for these four cases in figure 5.16(b). Without photoemission, the electron density has a wider profile with a lower maximum, and it is located farther from the dielectric. When photoemission is included, the effect of the low-energy photons (i.e., $\gamma_{\mathrm{peL}} = 0.5$) is most important here.

Figure 5.17 shows the streamer velocities versus their vertical position for all four cases. The photoemission coefficients have only a small effect on the velocity, which is a little higher with $\gamma_{\mathrm{peL}} = 0.5$. We think this is somewhat surprising. A possible explanation is that photoemission mostly leads to growth towards the dielectric, whereas photoionization in the gas contributes most of the free electrons that cause growth parallel to the dielectric. Another effect in the simulations presented here is that high-energy photons contribute less to a streamer's growth very close to a dielectric. There are two reasons for this. First, these photons are absorbed at shorter distances if they hit a dielectric. Second, their photoemission coefficient is here less than one ($\gamma_{\mathrm{peH}} = 0.5$), whereas in the gas they always lead to photoionization.

5.3.5   Effect of positive ion mobility

The positive ion mobility μ_i^+ can affect surface streamers in two ways. First, a higher ion mobility increases the amount of ion-induced secondary electron emission (ISEE). However, since ISEE was found to play a negligible role in section 5.3.4, its role is not further studied here, and we set the ISEE yield to zero (i.e., $\gamma_i = 0$).

A second effect is that a higher ion mobility increases the conductivity of
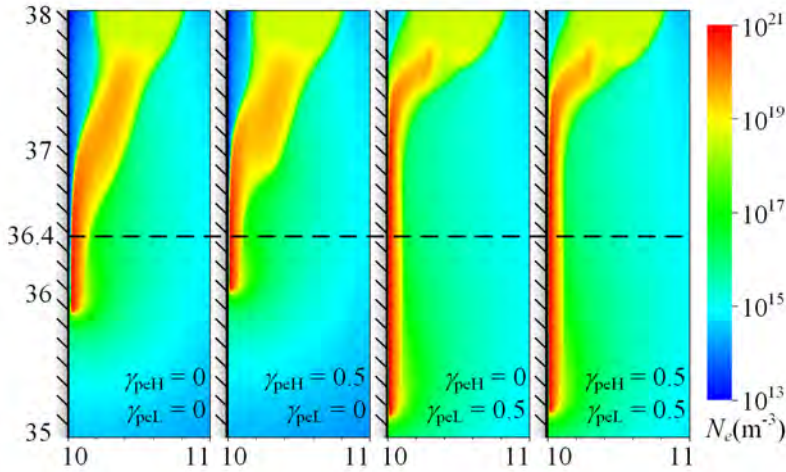
(a) The electron density at 11 ns
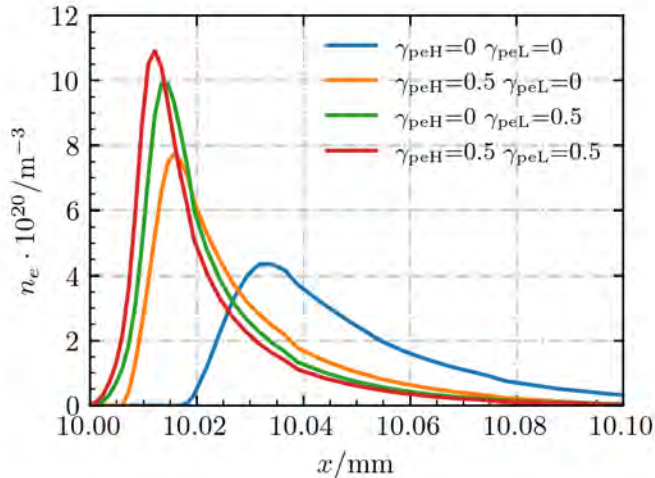
(b) Zoom of the electron density at $y = 36.4\,\text{mm}$

Figure 5.16: The electron density for simulations with different photoemission coefficients.

the discharge, in particular in regions where the ion density is high compared to the electron density. For positive surface streamer discharges, such a region is present in the streamer-dielectric gap. This gap typically contains a high electric field, especially close to the streamer head, see section 5.3.1. Electrons rapidly drift away from the surface, whereas positive ions move from the high-density discharge region towards the surface, as illustrated in figure 5.18.

To investigate how the positive ion mobility (μ_i^+) affects the decay of the high electric field in the streamer-dielectric gap, we have performed simulations with
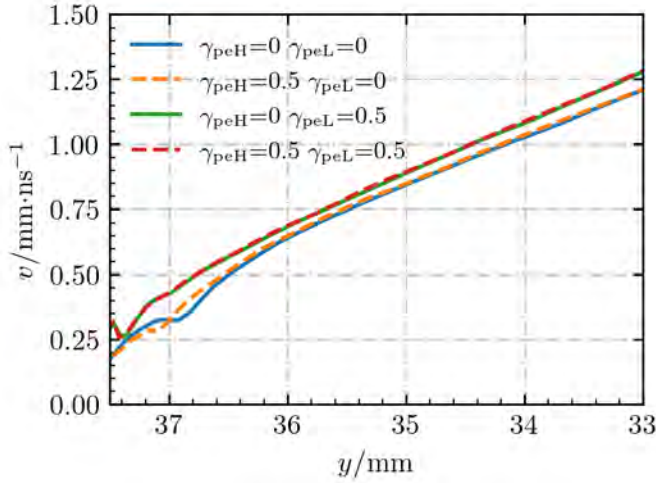
Figure 5.17: Streamer velocities versus their vertical location for different photoemission coefficients.
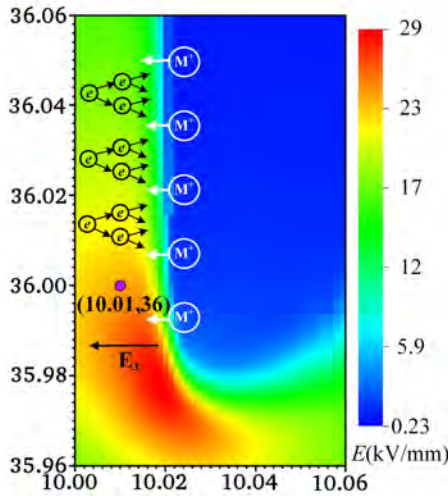
Figure 5.18: The electric field at 5.5 ns after streamer inception for a positive ion mobility of $3\times10^{-4}\,\mathrm{m^2/Vs}$. The electron and positive ion dynamics in the streamer-dielectric gap are illustrated.

positive ion mobilities of 0, $1\times10^{-4}\mathrm{m^2/Vs}$, $5\times10^{-4}\mathrm{m^2/Vs}$ and $1\times10^{-3}\ \mathrm{m^2/Vs}$, using a seed placed 0.5 mm from the dielectric. For these simulations, we have recorded E_x in the middle of the gap at the point indicated in figure 5.18. The recorded fields are shown versus time in figure 5.19. The maximum electric field occurs when the streamer heads pass by the observation point indicated in figure 5.18. The decay of the peak in E_x is faster for higher μ_i^+, which is most clearly
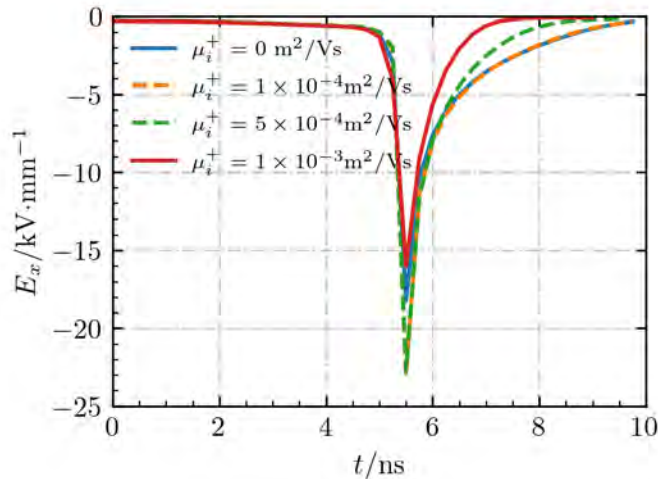
Figure 5.19: The E_x field at the point $(x, y) = (10.01\,\mathrm{mm}, 36\,\mathrm{mm})$ versus time for streamers with different positive ion mobilities. Here $t = 0$ corresponds to the streamers' respective inception times, which vary by less than a nanosecond for the four cases.

visible for the $\mu_i^+ = 5 \times 10^{-4}\,\mathrm{m^2/Vs}$ and $\mu_i^+ = 1 \times 10^{-3}\,\mathrm{m^2/Vs}$ cases. Note that the field also decays when the ions are immobile. This mainly happens because the amount of net space charge is lower behind the streamer head, but electron avalanches in the gap (due to e.g. photoionization) also contribute.

5.4 Interaction between negative streamers and dielectrics

To investigate the interaction between negative streamers and dielectrics, the following parameter values are used unless otherwise specified: an applied voltage of 120 kV, a relative permittivity of the dielectric (ε_r) set to 2, and a positive ion mobility (μ_i^+) set to $3 \times 10^{-4}\,\mathrm{m^2 \cdot V^{-1} s^{-1}}$. Electron emission from the dielectric is neglected, as elaborated in section 5.2.1.

The distance d between the initial seed and the dielectric is slightly varied in this section, see table 5.2. In section 5.4.1, we use $d = 1\,\mathrm{mm}$ to study the attraction of streamers towards the dielectric. In section 5.4.2 and 5.4.3, we use $d = 0.5\,\mathrm{mm}$, and in section 5.4.4 we use $d = 0\,\mathrm{mm}$ so that discharges directly start at the interface. When the initial seed is placed farther away from the dielectric, it will take longer for the streamer to reach the dielectric, but the further discharge evolution is similar, as was also observed in section 5.3.

The applied voltage, dielectric permittivity and pre-set surface charge are varied in sections 5.4.2, 5.4.3 and 5.4.4, see table 5.2. We study how these

parameters affect negative streamers, in particular their inception, propagation, morphology and surface charge characteristics. The simulations are performed up to 20 ns. In all considered cases, streamers have reached the dielectric and propagated over it within 20 ns. We do not consider later stages, in which the discharge has reached the other electrode.

Table 5.2: Investigated parameters and their values in each section. Here d is the distance between the seed center and the dielectric surface; U the applied voltage; ε_r the relative permittivity of the dielectric and σ_s the initial surface charge.

Section	d/mm	U/kV	ε_r	σ_s/pC·mm^{-2}
5.4.1	1	-120	2	0
5.4.2	0.5	$-112, -120, -128$	2	0
5.4.3	0.5	-120	$2, 3, 5$	0
5.4.4	0	-120	2	$-5, -1, 0, 1, 5$

5.4.1 Streamer-dielectric interaction

Comparison with positive streamers   The attraction of positive streamers to dielectrics has been demonstrated in several experiments (e.g. [170])) and simulations (e.g. section 5.3). In our simulations, we observe a similar attraction for negative streamers. Figure 5.20a shows the development of a negative streamer between 4 ns and 14 ns for an initial seed placed 1 mm away from the dielectric surface. For comparison, the development of a positive streamer under the same conditions (but with a different voltage polarity) is shown in Figure 5.20b.

The electron density in the positive streamer channel ($\sim 10^{19}$ m^{-3}) is higher than in the negative channel ($\sim 10^{18}$ m^{-3}). This can be explained as follows. Electrons drift away from negative streamers, whereas they drift towards positive streamers. The charge layer around positive streamers is therefore formed by positive ions, which are less mobile than electrons, so that positive streamer channels are more concentrated [19]. However, for both polarities, the electron densities of surface streamers ($\sim 10^{21}$ m^{-3}) are higher than those of gas streamers, which we also observed in section 5.3. This is primarily due to the enhanced electric field of surface streamers, shown in Figure 5.21 and discussed below. Surface streamers have a higher field due to electrostatic effects and due to their reduced radius compared to gas streamers.

Another distinguishing feature is that the negative streamer starts earlier. At 4 ns, its length is about 2 mm, whereas the positive streamer just starts. However, afterwards positive streamers have a higher velocity, especially when propagating over the surface. This is illustrated in Figure 5.21, which shows the streamer velocity and its maximal electric field versus streamer length.

From figures 5.20 and 5.21, we find that both negative and positive streamers reach the dielectric at around y = 35 mm. The negative surface streamer forms at around y = 29 mm and the positive surface streamer forms at about y = 33 mm. For both polarities, the maximum electric field and streamer velocity increase when propagating over the surface. The maximum electric field for the negative surface streamer is about $20 \sim 25$ kV/mm; for the positive one, it is over 30 kV/mm.

For both polarities, the dielectric's polarization strengthens the electric field between the streamer and the dielectric, which attracts the streamer to the dielectric. However, the negative streamer propagates along the surface for 6 mm before a surface streamer forms, whereas this distance is only 2 mm for the positive streamer. There can be two reasons for this. First, for negative streamers, electrons move away from the streamer channel, which leads to the accumulation of negative surface charge on the dielectric. This surface charge lowers the electric field between the streamer and the dielectric. Second, the negative streamer has a larger radius and a lower electric field. This means it has lower and more spread out charge density at its head, which leads to weaker electrostatic attraction to the surface.

Figure 5.22 shows the streamer velocity versus maximum electric field for the positive and negative streamers in figure 5.20. Compared to streamers in bulk gas [7, 19], the relation between v and E_{max} is more complicated for streamers interacting with dielectrics. Three stages with different slopes can be distinguished. When $v < 0.9$ mm/ns, streamers are propagating towards the dielectric. For v between 0.9 mm/ns and 1.6 mm/ns, a surface streamer forms, and for $v > 1.6$ mm/ns a surface streamer is propagating over the dielectric. Note that for the same velocity, negative streamers have a lower maximum electric field, but that the three stages occur at similar streamer velocities for both polarities.

Surface charge characteristics As mentioned before, electrons from a negative surface discharge move outwards, so towards the dielectric it is propagating over. Figure 5.23 shows the evolution of the surface charge for the negative streamer shown in Figure 5.20a. Up to 12 ns, the surface charge only increases, which happens most rapidly near the streamer head. Afterwards, a reduction in surface charge behind the streamer head is visible. This happens when the back of the negative streamer becomes more positively charged, so that the field between the back of the streamer and the negatively charged surface reverses. Positive ions then flow to the surface and partially neutralize it.

The increasing surface charge near the streamer head can produce a high electric field inside the dielectric, which was also observed in [71]. Figure 5.24 shows the electric field distribution for the streamer in Figure 5.20a at 14 ns. A high electric field is present around y = 37.43 mm, which corresponds to the location of the peak of the surface charge at 14 ns in Figure 5.23.

We remark that for positive surface streamers [71, 146], a streamer-dielectric
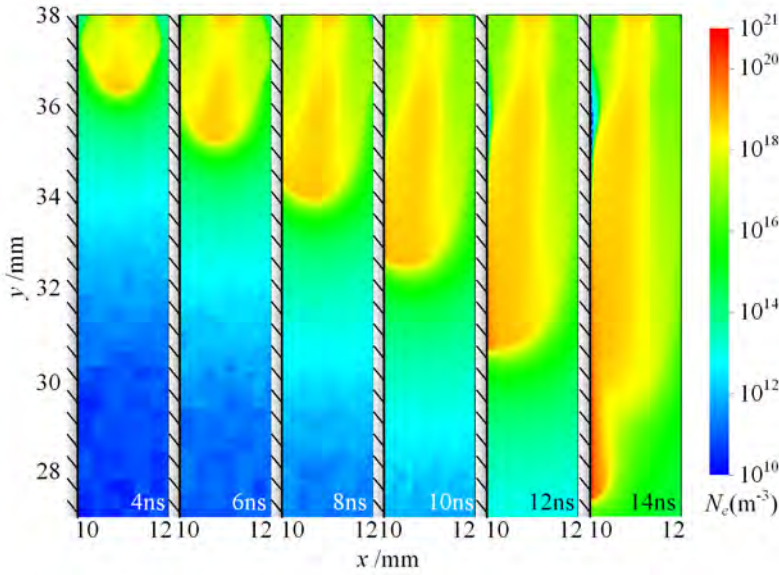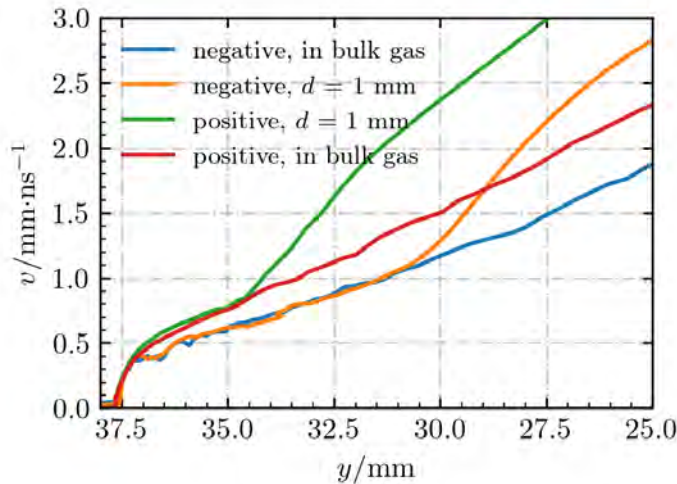
(a) Negative streamers
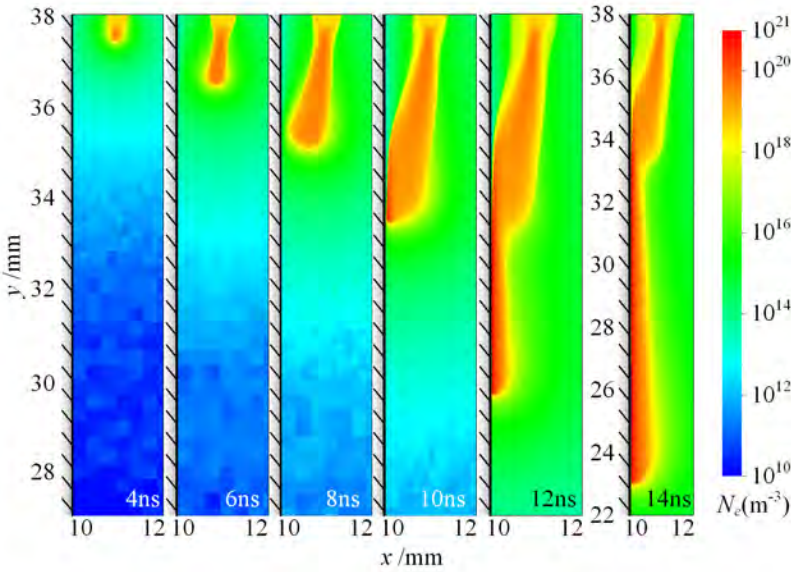
(b) Positive streamers

Figure 5.20: Evolution of negative (a) and positive (b) streamers between 4 ns and 14 ns, for an initial seed located at 1 mm from the dielectric surface on the left. The applied voltage is -120 kV for negative streamers and 120 kV for positive streamers. The dielectric permittivity is 2. Note that only part of the computational domain is shown in this figure.
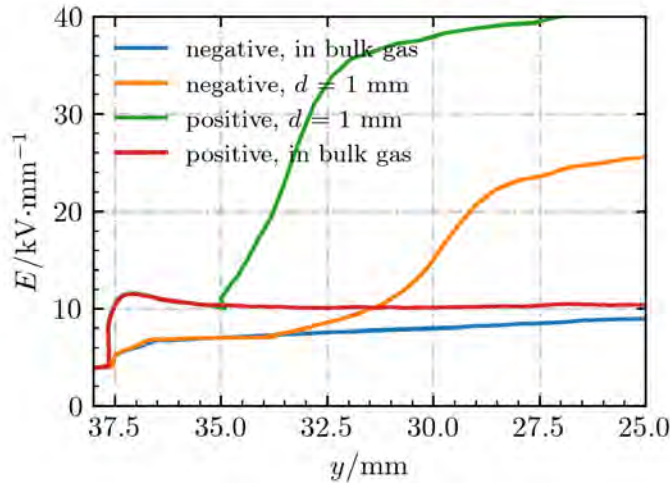
(a) The maximal electric field

(b) Streamer velocity

Figure 5.21: Streamer maximal electric field (a) and velocity (b) versus y-location of the electric field maximum. Results are shown for the negative and positive streamers in figure 5.20 (labeled "negative, d=1mm" and "positive, d=1mm", respectively) and for corresponding cases in bulk gas without a dielectric. The streamer velocity v is calculated by dividing the distance the streamer head moves between two consecutive outputs by the output time interval.

gap with a high electric field but a low electron density has been observed. For negative surface streamers no such gap is present, and the streamers can fully connect to the dielectric surface, as shown in figure 5.24.
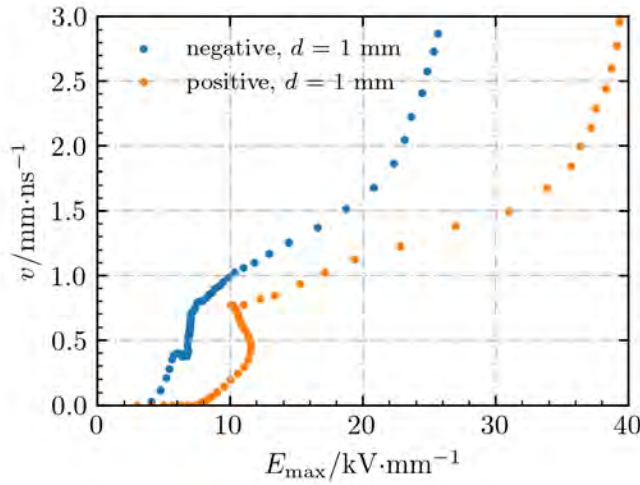
Figure 5.22: Streamer velocity versus maximum electric field at the streamer head. Results are shown for the negative and positive streamers in figure 5.20.
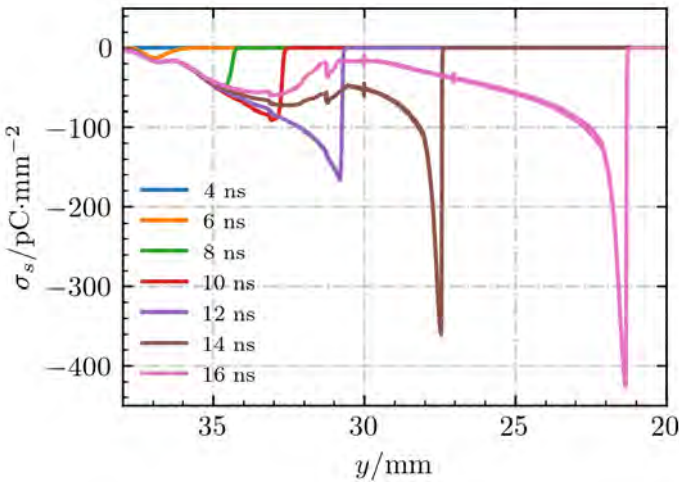
Figure 5.23: The evolution of the dielectric surface charge from 4 ns to 16 ns for the negative streamer from figure 5.20a.

5.4.2   Effect of applied voltage

To study the effect of the applied voltage on negative surface discharges, we have performed several simulations for applied voltages of 100 kV to 128 kV, which correspond to background electric fields of 2.5 kV/mm to 3.2 kV/mm. In all cases, the initial seed was located at 0.5 mm from the dielectric, and the evolution up to 20 ns was simulated. Negative streamers usually require a higher background
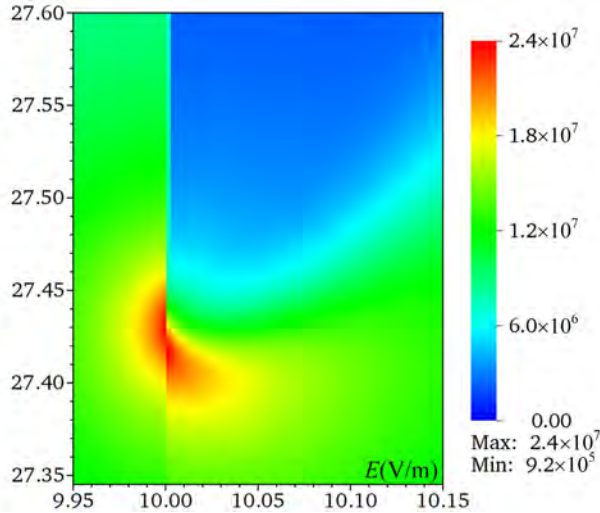
Figure 5.24: Electric field distribution for the negative surface streamer of figure 5.20a at 14 ns.

electric field than positive streamers [7]. With the geometry and initial seed used here, the formation of negative streamers required a background electric field of 2.6 kV/mm, which is a little bit lower than the breakdown threshold, whereas positive streamers could start in a field of 2.3 kV/mm. We remark that with a different initial seed or with a pointed electrode streamers can also form in lower background fields.

Figure 5.25 shows electron densities for negative streamers in background electric fields of 2.8 kV/mm, 3.0 kV/mm and 3.2 kV/mm. When compared at the same time, streamers are longer in a higher background electric field. Whereas the differences are initially small, they increase at later times, because the streamers accelerate. This is consistent with our findings for positive streamers. Similar behavior was also observed experimentally, e.g. in [68]. Although the background electric field affects the streamer velocity, the overall development for these three cases is similar. Surface streamers form at about y = 32 mm, and when compared at the same length they have a similar shape.

The streamer velocity versus y-position of the streamer head is shown in figure 5.26. With time, the velocities as well as the differences between them increase. Note that the negative streamer velocity does not start at zero, which is the case for positive streamers. The difference is that negative streamers propagate with at least the electron drift velocity [19], whereas positive streamers can only grow due to ionization.

Figure 5.27 shows the surface charge distribution when the streamer heads are located close to y = 28 mm. The profiles are similar, so the background electric field has only a small effect on the amount of surface charge deposited
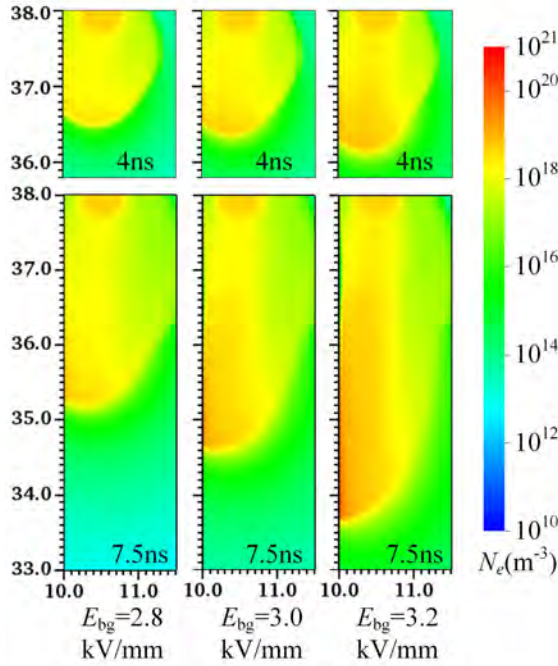
Figure 5.25: Electron densities for negative streamers in a background electric field of 2.8, 3.0 and 3.2 kV/mm, at 4 ns and 7.5 ns.
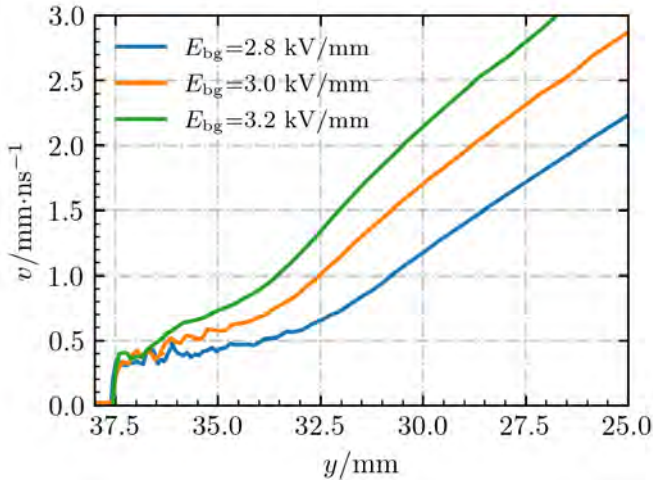

Figure 5.26: The streamer velocity versus the y-position of the streamer head in several background electric fields.
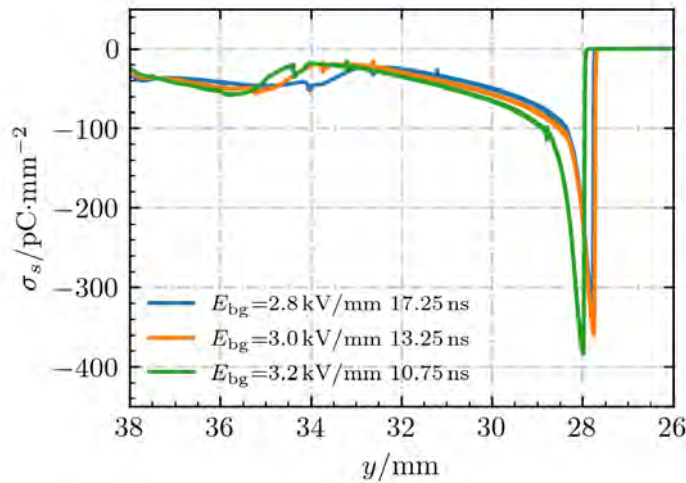
at a certain length.

Figure 5.27: The dielectric surface charge for streamers in different background electric fields. Curves are shown at the moment the streamer heads are close to y = 28 mm.

5.4.3 Effect of dielectric permittivity

To study the effect of the dielectric permittivity on negative surface discharges, we have performed simulations with relative permittivities of 2, 3 and 5. The initial seeds were again located at 0.5 mm from the dielectric, and simulations ran up to 20 ns.

Figure 5.28 shows the electron density at 4 ns and 9 ns. At 4 ns, the streamer lengths are still similar to each other. However, at 9 ns, the streamer velocity is clearly higher with a lower permittivity. The same can be seen in figure 5.29, which shows the streamer velocity versus the y-location of the streamer head. Initially, the streamer velocities are similar, but afterwards streamers are slower with a higher dielectric permittivity. The velocity difference (compared at the same length) becomes smaller as the streamers grow longer. The slower velocity can be explained from the following two aspects. A higher permittivity, which enhances the electric field between streamers and dielectrics, leads to stronger attraction of electrons to the surface. This directly leads to increased negative surface charge, which *reduces the electric field at the streamer head*. The other effect is that free electrons are more strongly attracted towards the dielectric. This can *reduce the amount of impact ionization taking place in front of the streamer*, as electron avalanches end up at the dielectric surface. We remark that positive streamers behave differently: a larger permittivity led to faster discharge inception, but had almost no effect on the streamer velocity.

Figure 5.30 shows the surface charge distribution when the streamers are close to y = 30 mm and y = 28 mm. For streamers of the same length, there is more
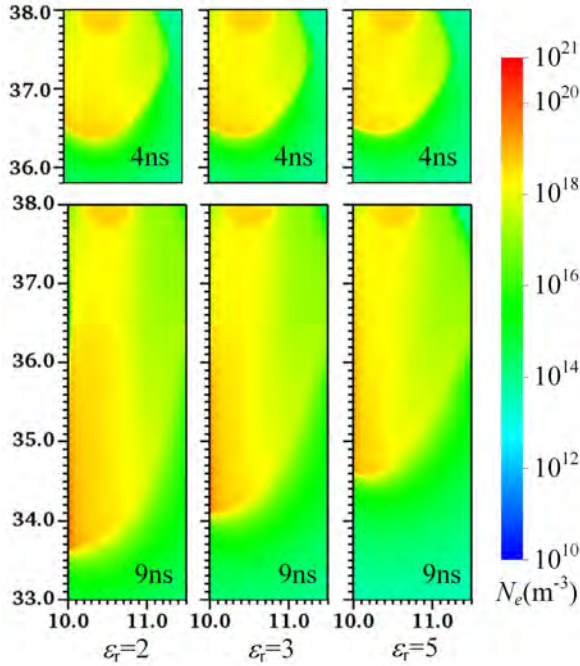
Figure 5.28: Streamer electron densities for dielectrics with relative permittivities ε_r of 2, 3 and 5, shown at 4 ns and 9 ns.
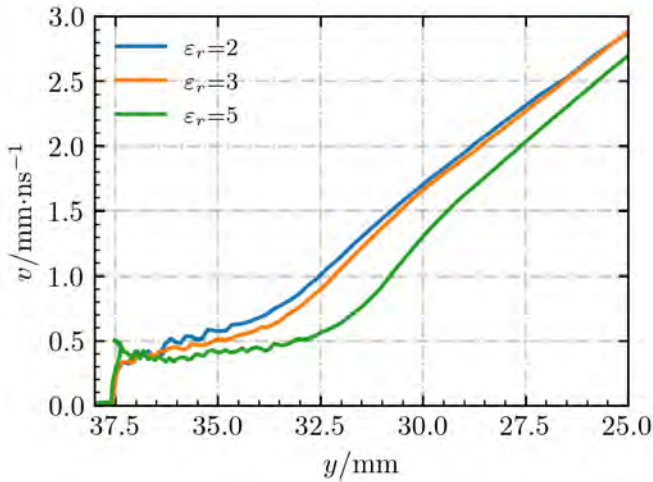

Figure 5.29: Streamer velocity versus y-location for different dielectric permittivities.

negative surface charge near the streamer head with a higher permittivity. After the streamer head has passed by, the surface charge profiles are similar for the

three cases. We can deduce that the amount of surface charge remaining after flashover is not sensitive to the dielectric permittivity. This is consistent with the discharge simulations reported in [80], in which the amount of surface charge was similar for different dielectric materials. On the other hand, the rate at which surface charge builds up before flashover could be sensitive to the permittivity.
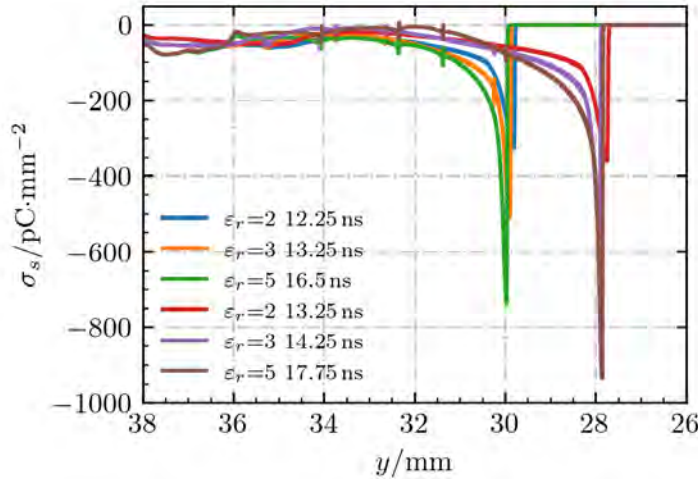
Figure 5.30: The dielectric surface charge for different dielectric permittivities, shown when the streamer heads are close to y = 28 mm and y = 30 mm. A higher permittivity leads to more negative charges close to the streamer head.

5.4.4   Effect of preset surface charge

Surface charge accumulation is considered to be a tough problem for HVDC spacers [178]. There have been quite a few experimental studies on how surface charge affects subsequent discharges. Two cases can be considered: 'same-polarity' surface charge, which has the same polarity as the surface discharge, and 'opposite-polarity' surface charge. In two studies [64, 67], same-polarity surface charge increased flashover resistance, whereas opposite-polarity surface charge reduced flashover voltage levels. In contrast, another study found almost no effect of same-polarity surface charge [65], and in [66] both unipolar and mixed-polarity surface charge reduced flashover resistance. Therefore, the effect of preset surface charge on surface discharges remains inconclusive.

The different experimental results mentioned above could be caused by different charge deposition methods. The experimental surface charge deposition methods also create ionization (electrons and ions) in the gas. Since this ionization affects the formation of surface discharges [179], it is hard to single out the effect of the deposited surface charge. Differences could also be caused by the fact that experimental charge deposition methods usually lead to a non-uniform

charge distribution. A non-uniform surface charge distribution can enhance the electric field near some parts of the dielectric, while reducing it in others.

Here we use numerical simulations to investigate the effect of preset surface charge on negative surface discharges. Compared to experiments, simulations allow full control over the initial surface charge distribution without affecting the background ionization level. Different amounts of surface charge (both positive and negative) are added at the beginning of the simulation. We place the initial seed so that its center coincides with the dielectric surfaces. This ensures that discharges start at the interface, which is also likely to happen in actual HV equipment. The simulations are performed up to 20 ns.

Figure 5.31 shows the maximum electric field versus time for preset surface charge densities of -5, -1, 0, 1 and 5 pC/mm². The surface charge is placed uniformly. An enhancement of the maximum electric field indicates the development of negative surface streamers, see figure 5.21. Figure 5.31 therefore shows that preset positive surface charge accelerates the development of negative streamers around dielectrics, while negative surface charge delays or inhibits negative surface discharges. Negative surface charges reduce the electric field ahead of the initial ionized seed, while positive charges enhance it. Our results agree with the experimental measurements in [64] and [67]. They are also in agreement with [68], in which it was found that residual surface charge with the same polarity as the applied high-voltage suppressed the development of surface discharges.
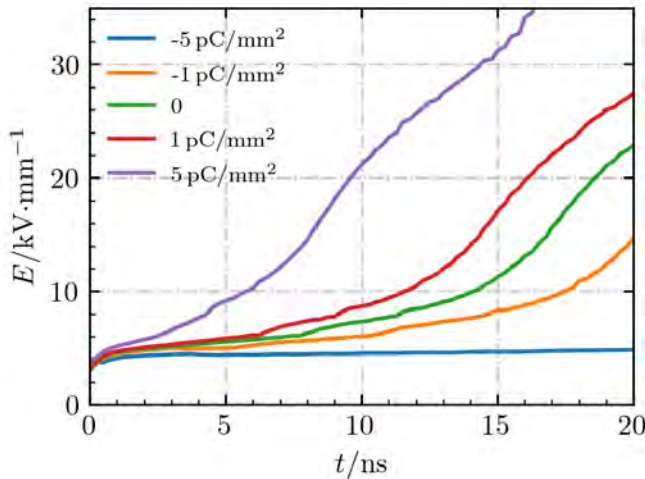

Figure 5.31: The maximum electric field versus time for simulations with preset surface charge densities of -5, -1, 0, 1 and 5 pC/mm². Enhanced electric fields indicate a negative surface streamer has formed.

Figure 5.32 shows the electric field along the dielectric surface for the above simulation cases, measured 1 μm away from the dielectric (in the gas) at t = 1

ns. At this time, the streamers start to form at the tip of the initial seed, located at 37.5 mm. Note that the uniform surface charge leads to a non-uniform change in the electric field, with the largest differences occurring near the electrodes. With a negative surface charge, the electric field near the negative HV electrode is reduced, whereas the field near the grounded electrode is enhanced. A positive surface charge has the opposite effect. These changes in the electric field have a strong effect on the development of surface discharges, as shown in figure 5.31.
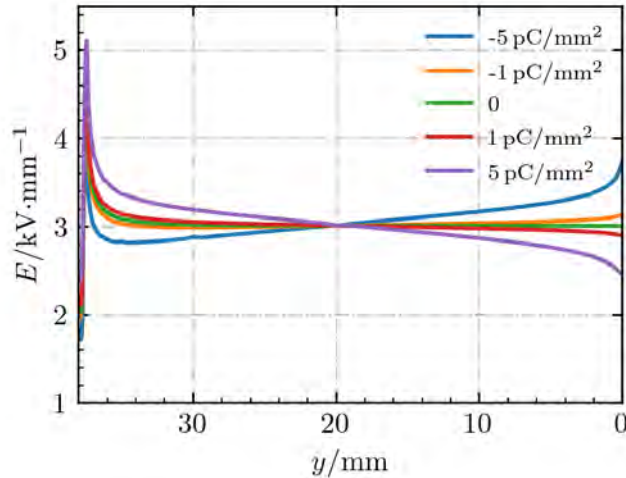
Figure 5.32: The initial electric field along the dielectric surface for simulations with preset surface charge densities of -5, -1, 0, 1 and 5 pC/mm^2. The values were measured at 1 μm outside the dielectric (in the gas) at t = 1 ns, when streamers start to form.

In section 5.4.1, we presented results in which negative streamers deposited negative surface charge on dielectrics. Such inhomogeneous surface charge may not increase discharge resistance. In actual devices, the effects of surface conduction and volume conduction should also be taken into account [178]. Further work is required to understand the role of these different mechanisms.

5.5   Comparing with 3D particle simulations

With our 2D model, we effectively simulate planar surface discharges. This leads to some differences compared to a full 3D description. First, the electric fields and charge densities in 3D are typically higher, as the streamer heads have a stronger curvature. Second, it is often observed that both surface and gas streamers are present in experiments [62, 180]. We do not observe these two components with our 2D model. Furthermore, as we mentioned in section 5.3.1, Fluid simulations may be unreliable for modeling the cathode sheath, which exhibits a high electric

field but contains a low electron density.

Based on the reasons stated above, preliminary 3D particle simulations are conducted in this section. Due to the high computational cost associated with 3D particle simulations, a smaller computational domain is utilized compared to that used in 2D fluid simulations, and the simulation time is also reduced. The electric field and electron density at the streamer head are qualitatively compared between 2D fluid simulations and 3D particle simulations.

5.5.1   Simulation settings

The computational domain for 3D particle simulations is shown in figure 5.33. It consists of a cube with a length of 8 mm for each Cartesian coordinate. The dielectric with a relative permittivity of 2 is placed on the left side with a width of 3 mm. The rest of the domain is filled with artificial air of 300 K and 1 bar.
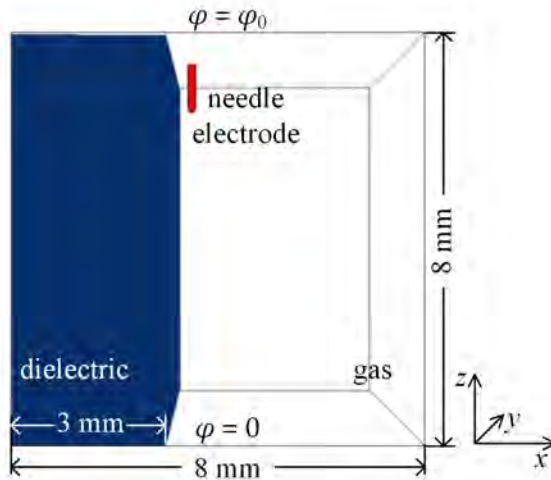
Figure 5.33: The computational domain for 3D particle simulations. A parallel-plate geometry with a needle protrusion is used, with a flat dielectric present on the left. Discharges start from the needle electrode.

We consider a plate-to-plate geometry with a needle protrusion connected to the high voltage electrode. The length of the needle electrode is 1.1 mm and it has a radius of 0.1 mm. The tip of the needle electrode is a hemisphere with the same radius. The center line of the needle electrode is placed at x=3.4 mm and y=4 mm, which is 0.4 mm away from the dielectric surface. The bottom electrode is grounded. A constant high voltage of 16 kV is applied on the upper electrode (including the needle electrode), which corresponds to a background electric field of 2 kV/mm between the plates. The boundary conditions of the potential on the sides of the domain are given by homogeneous Neumann conditions. The boundary conditions of the potential at the dielectric-gas interface

are described in section 2.4. The particles are removed from the simulation if they move into the needle-electrode or out of the domain. If a particle impacts the dielectric surface, surface charge is accumulated on the dielectric according to the particle's weight. The particle is then removed from the simulation. In this section, electron emission from the dielectric surface is disregarded.

The initial seed consists of 1000 electron-ion pairs at coordinates that are drawn from a Gaussian distribution centered at R_0 with a standard deviation of 20 μm. And R_0 corresponds to the point (x=3.4 mm, y=4 mm, z=6.8 mm) located 0.1 mm below the needle tip. The weight of each initial particle is set to 100.

The cross sections for N_2 and O_2 are taken from Phelps' database [123]. Super-particles are used to represent multi physical electrons. The desired particle number in one cell is set to 50. Adaptive mesh refinement is used to control the cell size, which leads to a minimal grid size of around 1 μm.

5.5.2   Morphology of surface streamers in 3D

We ran the codes on a super computer with 4 AMD Opteron 6344 12-core processors and 120 GB of RAM was used. With a computing time of 10 days, the simulation time reaches 4.2 ns. The electron density evolution of the streamer which starts at 0.4 mm away from a dielectric surface between 1 ns and 4 ns is shown in figure 5.34.
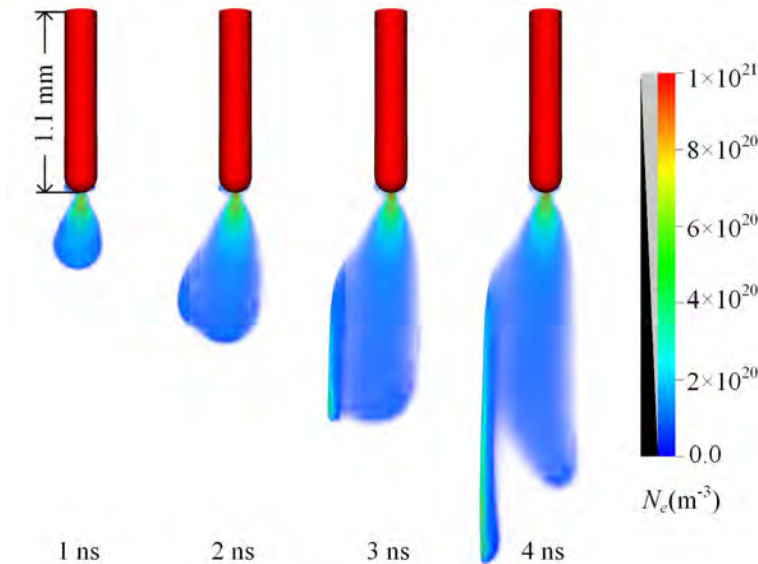

Figure 5.34: The electron density of a streamer which starts at 0.4 mm away from a dielectric surface between 1 ns and 4 ns. Front view. The dielectric is on the left side.

The evolution of the streamer follows a similar pattern as depicted in figure 5.3. Initially, the streamer initiates in the air and is subsequently attracted by the dielectric, propagating along its surface. This behavior is consistent with the findings from 2D fluid simulations. However, there is a notable difference that a gas-phase streamer component emerges alongside the surface component, which aligns with observations made in experiments [62, 63]. The gas-phase streamer component exhibits a slower velocity compared to the surface component, which is also in line with experimental observations [62, 63]. Furthermore, the surface streamer component exhibits a higher electron density and propagates at a faster speed, consistent with the results of the 2D fluid simulations.

In figure 5.35, we present the electron density at 4.2 ns from different views. The surface streamer appears narrower than the gas-phase component in the x direction while extending in the y direction, resulting in a pancake-like shape. On the other hand, the gas-phase component maintains a finger-like shape and propagates away from the surface component.
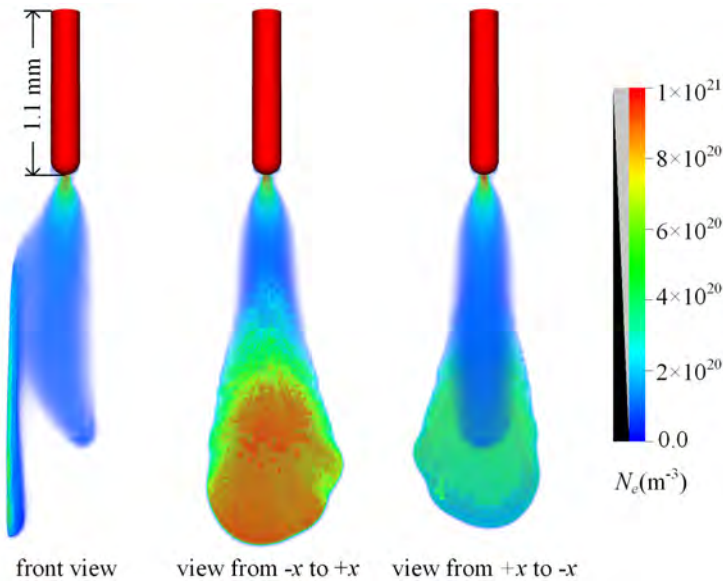

Figure 5.35: The electron density of the streamer in figure 5.34 at 4.2 ns in different views. The directions referenced in the figure are indicated in figure 5.33.

5.5.3 Comparison between 2D fluid simulations and 3D particle simulations

Figure 5.36 shows the electron density and the electric field around the streamer head of the streamer in figure 5.35, sliced at $y=4$ mm. The displayed region sizes and the color bar of figure 5.36 are the same as figure 5.7. Comparing figure 5.7

and figure 5.36, it is evident that the results from 2D fluid simulations exhibit similar characteristics to those observed in 3D particle simulations regarding the streamer head. In both cases, a cathode sheath with a low electron density and a high electric field is present in the gap between the surface streamer and the dielectric. Notably, the width of the cathode sheath is similar between the 2D fluid and 3D particle simulations. However, one distinction is that the width of the streamer head in the x direction is approximately 0.15 mm in 3D, which is narrower than the width observed in 2D (around 0.22 mm, as shown in figure 5.14). The particle simulation exhibits a lower electron density in the gap between the streamer and the dielectric compared to the fluid simulation, but this difference does not significantly impact the electric field profile.
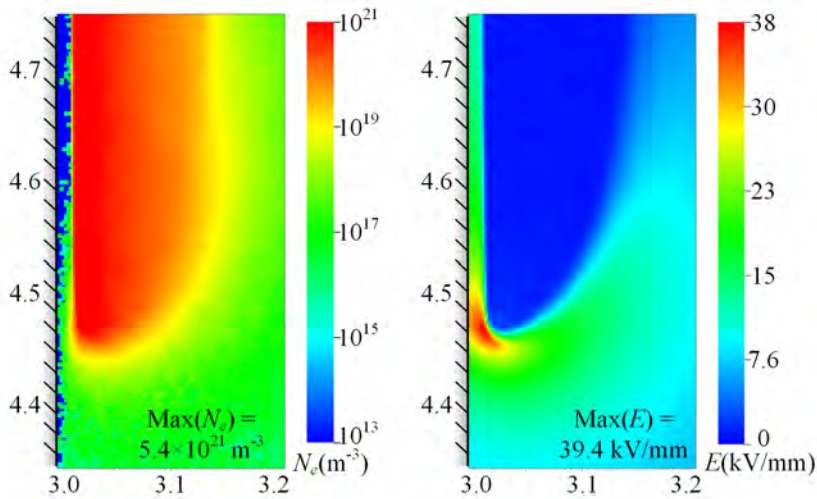

Figure 5.36: The electron density and the electric field around the streamer head of the streamer in figure 5.35, sliced at $y=4$ mm.

Although similar characteristics of streamer heads have been observed between 2D fluid and 3D particle simulations, we note that these two simulations were performed in different background electric fields ($E_{\mathrm{bg}}=2.5\,\mathrm{kV/mm}$ for the 2D fluid simulation and $E_{\mathrm{bg}}=2.0\,\mathrm{kV/mm}$ for the 3D particle simulation). In a preliminary test, the electric field at the streamer head is up to $50\,\mathrm{kV/mm}$ with a E_{bg} of $2.5\,\mathrm{kV/mm}$, since the streamer head has a stronger curvature in 3D than in 2D. Therefore, it is hard to run a relatively longer 3D particle simulation with a E_{bg} of $2.5\,\mathrm{kV/mm}$. We do observe that the streamer head shape is similar in different E_{bg} in 3D simulations as we observed in section 5.3.2. A higher E_{bg} would lead to higher electric fields and electron densities at the streamer heads.

5.6 Conclusions

In this chapter, we have studied both positive and negative surface streamers with numerical simulations. A 2D fluid model for surface discharges based on the Afivo-streamer code [111] was developed. The model includes a Monte Carlo procedure for photoemission from a dielectric surface. These new features are compatible with the adaptive mesh refinement and the parallel multigrid solver provided by the underlying Afivo framework [109].

We have used the new model to investigate the interaction of streamers and dielectrics. We considered a parallel-plate geometry, with a flat dielectric between the two electrodes. The characteristics of positive and negative surface discharges were compared. The effect of several parameters was investigated: the applied voltage, the dielectric permittivity, secondary electron emission caused by ions and photons, the mobility of positive ions and the preset surface charges. Our main findings are summarized below:

1. The attraction of streamers to the dielectric was found to be mostly electrostatic. In our geometry, this attraction was caused by the net charge in the streamer head, which polarized the dielectric, increasing the field between the streamer and the dielectric. A higher dielectric permittivity led to a more rapid attachment of the streamer to the dielectric.

2. Compared to gas streamers, both positive and negative surface streamers have a smaller radius, a higher electric field, and a higher electron density. In our simulations, this gave surface streamers a higher propagation velocity than gas streamers. The maximum electric field and propagation velocity of negative surface streamers are slightly lower than that of positive surface streamers.

3. A narrow gap forms between positive streamers and dielectrics, as was also observed in earlier work [71, 168, 169]. A very high electric field can be present in this so-called 'cathode sheath'. When negative surface streamers propagate along a dielectric, the negative surface streamer could touch the dielectric and the dielectric becomes negatively charged. The peak charge density occurs around the streamer head, and it produces a high electric field inside the dielectric.

4. A higher applied voltage caused the positive surface discharges to start earlier, but they behaved qualitatively similarly. A higher streamer velocity was observed with a higher applied voltage for both positive and negative polarities.

5. For a positive streamer, a higher dielectric permittivity also accelerated the formation of surface streamers. But for a negative streamer, a higher dielectric permittivity slows down the development of negative surface stream-

ers. This could be due to an increase in negative surface charge near the streamer head, which reduces the streamer's electric field. The effect becomes weaker for longer streamers.

6. For positive streamers, photoemission can accelerate streamer inception near dielectrics. However, photoemission hardly increases the velocity of surface streamers. A possible reason is that photoemission mostly leads to growth towards the surface, whereas photoionization contributes more to the growth parallel to the surface.

7. The positive ion mobility affects the decay of the high electric field in the streamer-dielectric gap for positive streamers.

8. Preset positive surface charge accelerates the development of negative streamers around dielectrics, whereas negative surface charge delays or inhibits negative surface discharges.

Furthermore, the results of the 2D fluid simulations of a positive streamer were compared with 3D particle simulations. We have observed the presence of both a surface streamer component and a gas-phase streamer component. Additionally, similar cathode sheath structures were found between the surface component and the dielectric in 3D and 2D simulations.

Chapter 6

The effect of photoionization on positive streamers in CO_2 studied with 2D particle-in-cell simulations

We investigate the effect of photoionization on positive streamer propagation in CO_2 with 2D particle-in-cell simulations. Positive streamers require free electrons ahead of them to sustain their propagation, which in air are typically provided by photoionization. Photoionization in CO_2 is much weaker than it is in air, because fewer ionizing photons are produced and their typical absorption distance is orders of magnitude smaller. Our results show that even a small amount of photoionization is possible to sustain positive streamer propagation, but that requires a higher electric field around the streamer head than in air. Furthermore, we propose a self-sustaining criterion for streamer discharges in CO_2 and we discuss the uncertainties in the photoionization model.

This chapter is adapted from an electronic publication with a reduced introduction and model description:

6.1 Introduction

Discharges can occur in a wide range of gases. The properties of the gas have a direct influence on the discharge characteristics in it. The discharges in a single gas atmosphere exhibit distinct characteristics compared to in air, such as more branches [7]. CO$_2$ is increasingly used as an insulating gas [93, 102] in high-voltage equipment, and it is the main component of many alternatives to SF$_6$ [181, 182]. Electric breakdown properties of CO$_2$ have been measured in many previous studies [94–100]. We here focus on streamer discharges in CO$_2$, which play an important role in the early stages of electric breakdown [6].

Positive streamers require a source of free electrons ahead of them to sustain their propagation [6], as illustrated in figure 6.1. In air, such electrons are typically provided by photoionization, but in CO$_2$ photoionization is much weaker, since fewer ionizing photons are produced and because their typical absorption distance is orders of magnitude smaller [92, 107]. In this chapter, we focus on a particular question that was raised in [105]: can positive streamers propagate due to photoionization in CO$_2$? A quantitative photoionization model for CO$_2$ is proposed. We use 2D particle-in-cell simulations to study whether such weak photoionization in CO$_2$ can sustain positive streamer growth. Furthermore, we present a criterion for self-sustained propagation due to photoionization. And we discuss how the assumption of a 2D Cartesian geometry affects our results compared to a fully 3D description.
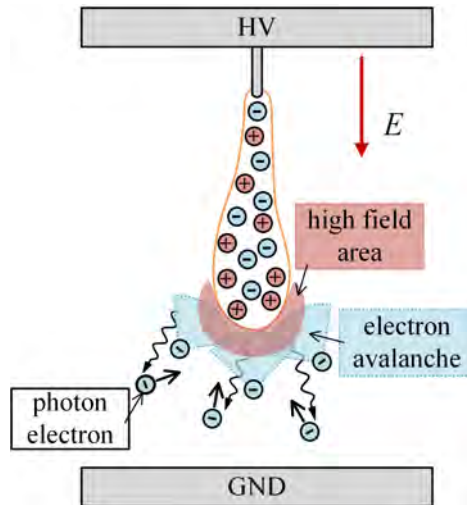

Figure 6.1: Schematic illustration of self-sustained positive streamer propagation due to photoionization. The streamer grows due to incoming electron avalanches, which should generate a sufficient number of photo-electrons ahead of the streamer so that the process is sustained.

6.2   Simulation method

We simulate positive streamer discharges in CO_2 using `afivo-pic` [112, 140], an open-source parallel AMR code for particle-in-cell discharge simulations with Monte-Carlo collisions (PIC-MCC).

6.2.1   PIC-MCC model

We provide a brief summary of the model below, for a more detailed description see [112, 140]. Ions as tracked as densities, and they are assumed to be immobile on the nanosecond time scales considered in this chapter. Electrons are tracked as particles. They are accelerated by the electric field and stochastically collide with a background of neutral gas molecules. The electron coordinates and velocities are advanced with the 'velocity Verlet' scheme, and isotropic scattering is assumed for collisions. Electron-neutral scattering cross sections for CO_2 were taken from the IST-Lisbon database [183] on LXCat. This database contains an effective momentum transfer cross section, accounting for the combined effect of elastic and inelastic processes [184]. We subtracted the sum of the inelastic cross sections to obtain an approximate elastic cross section that can be used in the particle model.

To make the particle-in-cell simulation computationally feasible, super-particles are used to represent several physical particles. The weights of super-particles (how many physical particles they stand for) are adaptively controlled to obtain a desired number of simulated particles per cell, which is here set to 75. Details of the weight control method can be found in [112] and [140].

For simplicity and efficiency the simulations are performed in a 2D Cartesian geometry, as full 3D simulations would be very costly. These 2D simulations can be interpreted as taking place in a 3D slab of dimension $L_x \times L_y \times L_z$, periodic in the z dimension, where $L_x \times L_y$ is the size of the computational domain and L_z is a finite length. Particle densities are computed by averaging over the z coordinate. The length L_z controls the amount of particle noise, and is here set to $1\,\mathrm{mm}$, as further discussed in section 6.4.2.

For computational efficiency, adaptive mesh refinement is used [109]. The mesh is refined if $\alpha(E)\Delta x > 0.5$, where α is the ionization coefficient. This leads to a minimal grid size of around $1\,\mu\mathrm{m}$ in our simulations.

6.2.2   Possible electron sources for positive streamers in CO_2

Positive streamers require a source of free electrons in front of them for their propagation [6]. Below, we discuss two common sources of such electrons: background ionization and photoionization.

Background Ionization Background ionization levels in ambient air (by radioactivity and cosmic rays) were reported to be 10^9 - $10^{10}\,\mathrm{m^{-3}}$ at ground

level [152]. The background ionization level in an experimental vessel filled with CO_2 from a high-pressure gas cylinder is probably significantly lower, as the gas would contain less radon than ambient air. Experimentally, large statistical time lags have been observed for the inception of positive streamers in CO_2 [102, 103], which suggests that there are typically few free electrons.

For positive streamer propagation, the composition of the background ionization also matters. In electro-negative gases such as air, background ionization is mostly present in the form of positive and negative ions. However, in pure CO_2, electron attachment is always dissociative $CO_2 + e \rightarrow CO + O^-$ [185], which means that it only occurs for electrons with energies above 3 to 4 eV. In the absence of an electric field, we therefore expect the main electron loss processes to be wall losses, electron-ion recombination and electron attachment due to gas impurities. Depending on the type of impurity, it might be possible to detach electrons from negative ions when an electric field is later applied.

There is considerable uncertainty in all the above processes, which makes it difficult to provide generic estimates for background ionization levels in CO_2. We therefore focus on the effect of photoionization in this chapter, and assume there is negligible background ionization.

Photoionization in CO_2 Compared to air, there is relatively little information about photoionization in CO_2 [92]. We implement a Monte Carlo photoionization model in CO_2 based on the results of Przybylski [107]. In [107] the ratio $\xi\omega/\alpha_{\text{eff}}$ was measured at pressures of about 1 to 3 Torr, with values between 0.6×10^{-4} and 4.8×10^{-4}. This ratio indicates how many photoionization events are generated (on average) per net electron-impact ionization, with α_{eff} being the effective ionization coefficient, ω the photon production coefficient (with the same units as α_{eff}), and ξ the probability of ionization after photon absorption. The value of $\xi\omega/\alpha_{\text{eff}}$ depends on the reduced electric field, and we follow the assumption made in [92] that the pressure range in [107] to corresponds to reduced electric fields between 260-1000 Td, resulting in the field-dependence shown in figure 6.2. Note that we extrapolated the ratio to zero for E/N = 200 Td, and that the ratio $\xi\omega/\alpha = \xi\omega/\alpha_{\text{eff}} \cdot (\alpha_{\text{eff}}/\alpha)$ is also shown.

We use photon absorption coefficients from [92, 186]. According to [92], photons with wavelengths of 83-89 nm can contribute to the photoionization of CO_2. For these photons, the absorption coefficients range from 0.34 to 2.2 $cm^{-1}Torr^{-1}$, which corresponds to absorption lengths in the range of 6.1-40 μm at standard temperature and pressure.

There are several uncertainties in the above photoionization model, which are discussed in section 6.4.1.

Monte Carlo photoionization procedure We use a Monte Carlo photoionization procedure similar to the one described in [112, 137]. The basic steps
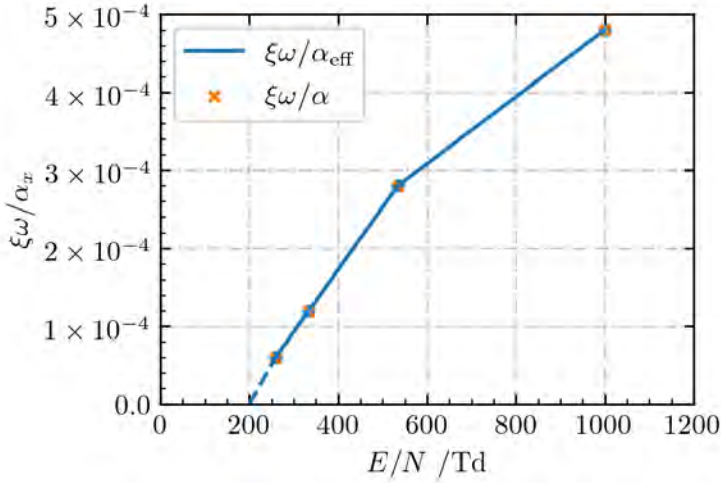
Figure 6.2: Coefficients $\xi\omega/\alpha_{\mathrm{eff}}$ [92, 107] and $\xi\omega/\alpha$ (nearly identical), describing how many photoionization events are generated on average per (net) electron-impact ionization. We extrapolated $\xi\omega/\alpha_{\mathrm{eff}}$ to zero for $E/N = 200\,\mathrm{Td}$.

are as follows. For each electron impact ionization event, an ionizing photon is generated with probability $\xi\omega/\alpha$. Such a photon starts at the location of the ionization, and its direction is sampled from an isotropic distribution. Absorption coefficients μ are sampled as

$$\mu = \mu_{\min}(\mu_{\max}/\mu_{\min})^{U_1}, \tag{6.1}$$

where U_1 is a (0,1) uniform random number, $\mu_{\max}/p = 2.2\,\mathrm{cm}^{-1}\mathrm{Torr}^{-1}$ and $\mu_{\min}/p = 0.34\,\mathrm{cm}^{-1}\mathrm{Torr}^{-1}$ are the maximum and minimum absorption coefficients [92, 186]. Note that this sampling follows from the linear approximation in figure 24 of [92]. Afterwards, absorption distances are sampled from the exponential distribution as

$$l = -\ln(1 - U_2)/\mu, \tag{6.2}$$

where U_2 is another (0,1) uniform random number. Finally, a photoionization event is generated at the location where the photon is absorbed, generating a free electron and a positive ion.

6.2.3   Simulation domain and initial conditions

We simulate positive streamers in CO_2 at $300\,\mathrm{K}$ and $1\,\mathrm{bar}$, using the 2D Cartesian computational domain illustrated in figure 6.3. The computational domain measures $8\,\mathrm{mm}$ (width) times $16\,\mathrm{mm}$ (height). We use a parallel-plate electrode geometry with a needle protrusion. A $2.1\,\mathrm{mm}$ long needle electrode is inserted at the center of the HV electrode, with a $0.1\,\mathrm{mm}$ radius and a rounded tip.
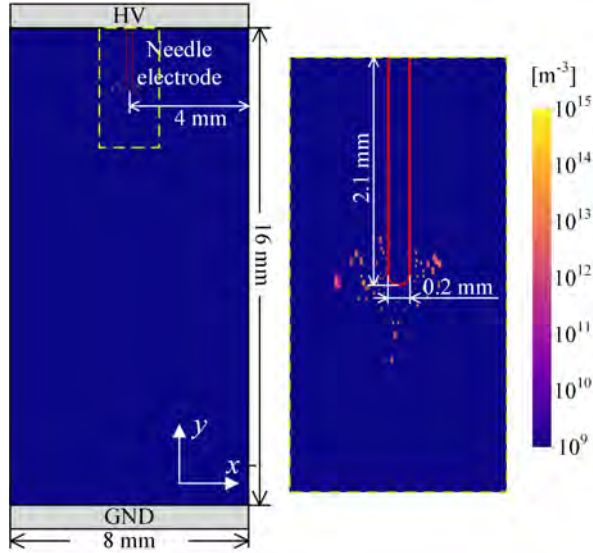
Figure 6.3: The computational domain and an example of the electron density
due to the initial seed.

A high voltage of 32 kV is applied on the upper electrode while the lower
electrode is grounded. The background electric field $E_{bg} = 2\,\text{kV/mm}$ is defined
as the applied voltage divided by the gap length (16 mm). Note that E_{bg} is below
the breakdown electric field $E_{bd} = 2.2\,\text{kV/mm}$ [105].

Homogeneous Neumann boundary conditions are applied for the electric po-
tential on the left and right sides. Electrons are absorbed at electrodes, but not
emitted.

To initiate the discharges, a neutral seed is used. The seed consists of 100
electron–CO$_2^+$ pairs at coordinates that are drawn from a Gaussian distribution
centered at the tip of the needle electrode with a standard deviation of 0.2 mm.
The corresponding initial electron density is shown in figure 6.3.

6.3   Results

6.3.1   A positive streamer in CO$_2$ with photoionization

We simulate streamer discharges in pure CO$_2$ with an applied voltage of 32 kV
using the model and conditions described in section 6.2. We run the simulation 7
times since the simulation results are stochastic when using a Monte Carlo model.
The first line of figure 6.4 shows the electron density profiles for these different
runs when the streamer heads locate approximately at y = 6 mm. The labels
on the figures indicate the time when each reaches the location. The average
time is 33 ns with a standard deviation of 1.41 ns. The streamer velocities are

similar across multiple runs and this is also the case for the electron density in the
streamer channel and the streamer radius. The electron density and electric field
of the streamer in the first row (first line) between 5 ns and 32.5 ns are presented
in the last two lines of figure 6.4. The streamer continuously propagates in the
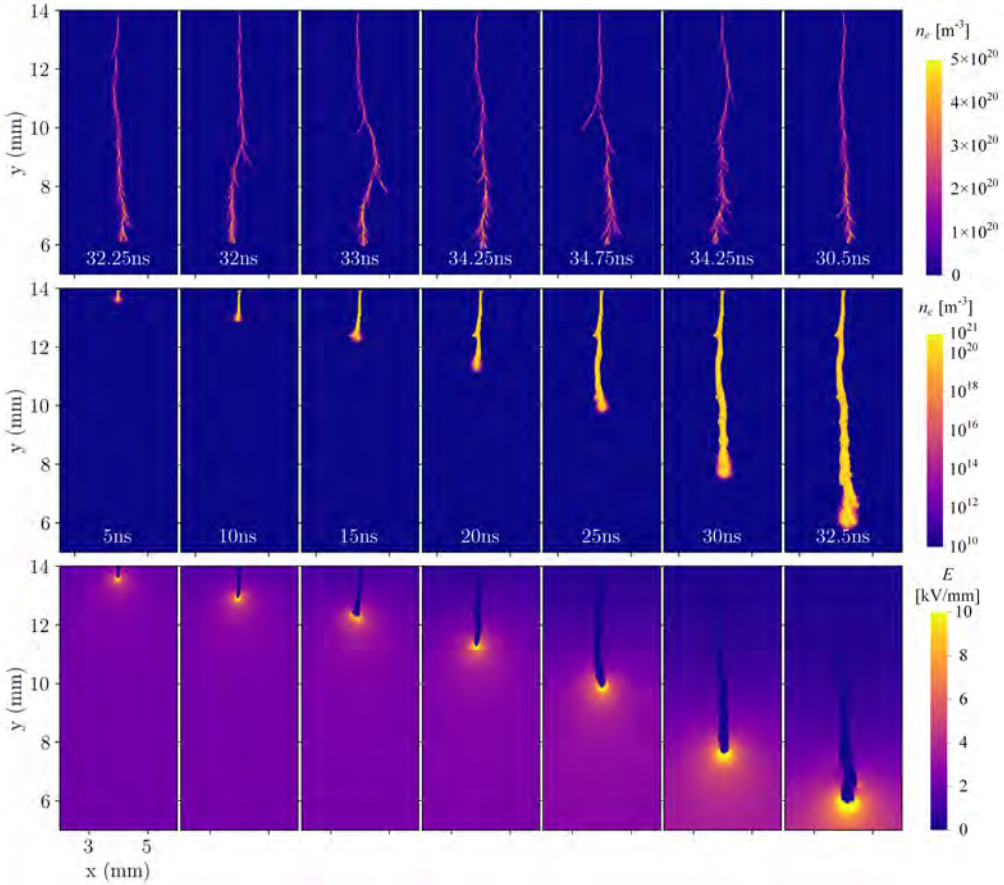gap, sustained by the photoionization it produces.

Figure 6.4: Top row: electron density in linear scale for several positive streamers
in CO_2, with the streamer heads located approximately at y = 6 mm. Bottom
two rows: time evolution of the electron density in logarithmic scale and electric
field of the streamer in the upper-left corner between 5 ns and 32.5 ns.

In these simulations, photoionization is much weaker than it is in air, mostly
due to the short absorption distance of ionizing photons. This results in a steeper
electron density gradient around the streamer edge than in air, as was also ob-
served to a lesser extent in simulations in air-methane mixtures [187]. Another
effect is that the discharge develops more stochastically, with streamer branch-
ing, and in particular many small branches. This happens because there are
relatively few photons that are absorbed at a sufficient distance to contribute to

discharge growth.

The electron density in the streamer channel is around $10^{21}\,\mathrm{m^{-3}}$ and the maximum electric field at the streamer head is around 16-20 kV/mm during the entire evolution, which is much higher than typical electron density and maximum electric field of positive streamers in air [105]. Although the channel develops stochastically, the streamer radius increases in a relatively stable way as the streamer bridges the gap.

6.3.2 A self-sustaining criterion for streamer discharges in CO$_2$

Self-sustained positive streamer growth requires $N_{\mathrm{sp}} \geq 1$, where N_{sp} is the number of new photoionization events that will on average be produced due to a single initial photoionization event. We present an approximate criterion for such self-sustained growth based on the work of Naidis [188], in which criteria for discharge inception in air near spherical and cylindrical electrodes were presented. Our criterion has the following form:

$$N_{\mathrm{sp}} = f_{\mathrm{g}}\,\xi\omega/\alpha_{\mathrm{eff}} \int_0^{r_c} p(r)N_e(r)\mathrm{d}r \geq 1, \tag{6.3}$$

where $r = 0$ corresponds to the streamer head position (the location of its charge layer), r_c is the distance at which the electric field equals the critical field, $p(r)$ is the probability of photon absorption at a distance r and $N_e(r)$ is the final size of an electron avalanche starting at location r traveling to $r = 0$. Furthermore, f_{g} is a geometric factor, and $\xi\omega/\alpha_{\mathrm{eff}}$ is the factor given in figure 6.2. The underlying idea is that a photoionization event produces an electron avalanche growing towards the streamer head.

Equation (6.3) is a simplified version of an equation given in [188]. As in [188], we assume that new photons are produced at $r = 0$, since the number of electrons grows exponentially in an avalanche. The factor $\xi\omega/\alpha_{\mathrm{eff}}$ therefore depends on the field at the streamer head. The probability of photon absorption is given by [89]

$$p(r) = \frac{\exp(-\mu_{\mathrm{min}}pr) - \exp(-\mu_{\mathrm{max}}pr)}{r \log(\mu_{\mathrm{max}}/\mu_{\mathrm{min}})}, \tag{6.4}$$

where μ_{min} and μ_{max} are the pressure-reduced absorption coefficients given in section 6.2.2.

A simplification made here is the geometric factor f_{g}. Since streamers have no spherical or cylindrical geometry, we use a simple line integral along their axial direction. We roughly correct for geometric effects by assuming only photons within an opening angle $\theta_{\mathrm{max}} = 20°$ contribute, so that $f_{\mathrm{g}} = \sin(\theta_{\mathrm{max}}/2)^2 \approx 0.03$.

Another modification is that we limit the size of avalanches to N_{max}, so that

$$N_e(r) = \min\left[N_{\mathrm{max}}, \exp\left(\int_0^r \alpha_{\mathrm{eff}}(r')\mathrm{d}r'\right)\right]. \tag{6.5}$$

As mentioned in [188], the exponential growth of avalanches stops when space charge effects become important, see e.g. [189]. The number of electrons in a streamer will depend on its length, radius and degree of ionization, but for simplicity, we use a single value $N_{max} = 10^8$. Without such a limitation, there would be contributions of unrealistically large avalanches to equation (6.3), due to the strong field around a streamer. Note that equation (6.5) is equivalent to limiting the α-integral to a value $\log(N_{max}) \approx 18.4$.

Figure 6.5 illustrates the criterion of equation (6.3). For several electric field profiles, the value of $\log(N_e)$ and the integrand $p(r)N_e(r)$ of equation (6.3) are shown, and the resulting values for N_{sp} are given. The electric field profiles were extracted from the simulations shown in figure 6.4 in the vertical direction, starting from the streamer head, at 5 ns, 10 ns, 15 ns and 20 ns. The values of N_{sp} suggest that the streamer is initially barely self-sustained ($N_{sp} \sim 1$), whereas at later times there are more photons available. However, we emphasize that there is quite some uncertainty in equation (6.3), mostly due to the assumptions about the geometric factor f_g and due to the simple assumption of a maximum avalanche size N_{max}.

6.4   Discussion

6.4.1   Uncertainties of photoionization in CO_2

As mentioned in [92], the only direct measurements of photoionization parameters in CO_2 (photon production and absorption) were performed in the sixties by Przybylski [107] and Teich [108], at pressures of about 1 to 3 Torr. Our photoionization model is based on these measurements, and it contains several uncertainties. Most importantly, there appears to be no information on the collisional quenching of emitting states, which could play a major role at atmospheric pressure (as it does in air). Furthermore, measurements obtained at different pressures and a constant current were converted into an E/N dependence in [92]. It is unclear how accurate this E/N dependence is, in particular when used in a streamer discharge model in which fields vary rapidly in space and time. Other uncertain aspects are that a factor 4π might have to be included in $\xi\omega/\alpha_{eff}$, as discussed in [92], and that the purity of the CO_2 used in the experiments was not reported.

Another option could be to directly use cross sections to model photoionization in CO_2. The first ionization limit of CO_2 is 13.77 eV, which corresponds to a photon wavelength of 90 nm. According to Pancheshnyi [92], photons in the spectral range of 83-89 nm can contribute to the photoionization of CO_2. Such photons can be produced by transitions of O_{II}, C_{II} and O_I after the dissociation of a CO_2 molecule. Dissociation cross sections contributing to VUV emission were reported in [190]. These cross sections peak at energies of 100 eV to 200 eV, and they require a typical threshold energy of about 50 eV.
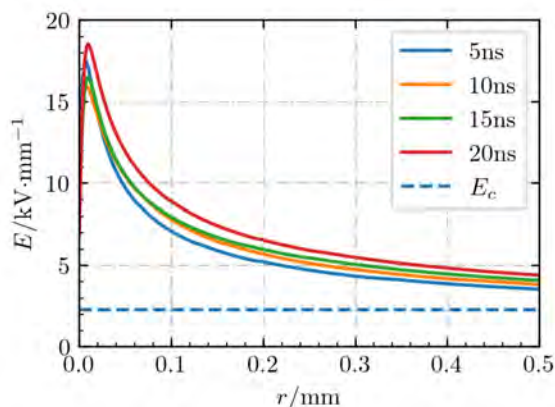
(a) Vertical electric field profiles near the streamer head of the streamer in figure 6.4
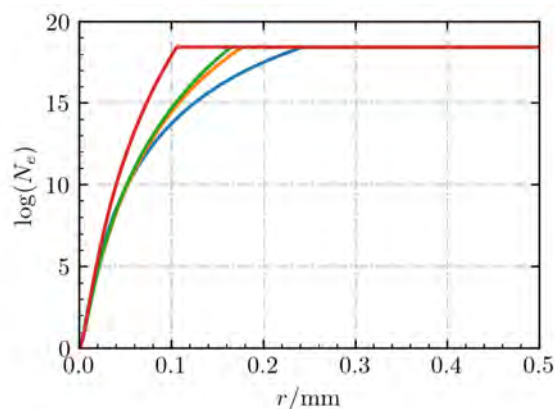
(b) Logarithm of electron avalanche size $N_e(r)$ according to equation (6.5) versus the start position of the avalanche
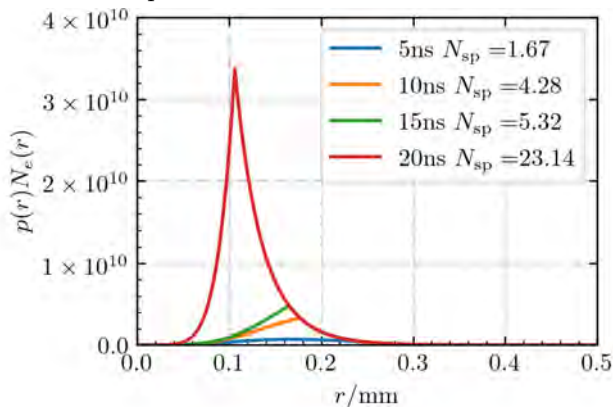
(c) The integrand $p(r)N_e(r)$ of equation (6.3), where $p(r)$ denotes the probability of photon absorption at a distance r

Figure 6.5: Illustration of the criterion in equation (6.3) with electric fields extracted from the simulations shown in figure 6.4.

In preliminary tests with these cross sections, they led to a significantly smaller production of photoionization than expected from the measurements of Przybylski and Teich [107, 108]. To more accurately model photoionization in CO_2 at atmospheric pressure would thus probably require new measurements.

6.4.2   Effects of 2D Cartesian geometry

For computational reasons, we have performed simulations in a 2D Cartesian geometry. Below, we discuss the effect of this geometry on our results.

One major difference is that in a Cartesian 2D geometry field enhancement is significantly weaker, and it decays less rapidly in space, since streamer heads in 2D have no curvature in the third dimension. However, the criterion for self-sustained growth derived in section 6.3.2 is generic, and can also be applied in 3D. For example, if we assume that the electric field (E_{3D}) ahead of a streamer is given by

$$E_{3D} = (1 + r/R)^{-2}(E_{max} - E_{bg}) + E_{bg}, \tag{6.6}$$

where $r = 0$ corresponds to the location of E_{max} at the streamer head, $R = 0.1\,\text{mm}$, $E_{max} = 22\,\text{kV/mm}$ and $E_{bg} = 2\,\text{kV/mm}$, then the result is $N_{sp} = 13.5$, indicating that self-sustained growth is possible. The more rapid decay of the field in 3D has no strong effect, since most photons are absorbed close to the streamer head. Self-sustained growth is thus probably more easily obtained in 3D, due to the stronger field enhancement.

Although streamer branching can only be accurately studied in 3D, we can qualitatively study the effect of stochastic fluctuations in 2D as well. As discussed in section 6.2.1, the amount of particle noise in a 2D simulation can be controlled by a parameter L_z, which indicates the 'depth' over which particle densities are averaged in the third dimension. To investigate how L_z affects the simulation results, we ran four cases with L_z set to $100\,\text{mm}$, $10\,\text{mm}$, $1\,\text{mm}$ and $0.1\,\text{mm}$, which are shown in figure 6.6. Propagation velocities are similar in all cases. The electron density around the streamer is smoother with a larger L_z, as expected. A smaller value of L_z leads to a more irregular and thinner channel, with a somewhat higher electron density.

We speculate that in 3D, positive streamers in CO_2 would develop in a highly irregular manner with many thin branches, similar to the evolution illustrated in figure 6.6. Such stochastic growth has experimentally been observed in other gases with weak or no photoionization [88].

6.4.3   Voltage dependence and inception behavior

We have studied the effect of the applied voltage by varying it with steps of $0.8\,\text{kV}$. For voltages between $28.8\,\text{kV}$ and $31.2\,\text{kV}$, we observed the formation of a local ionized cloud around the needle tip, which did not result in streamer propagation. Short positive streamers have also been observed in experiments [102]. In this
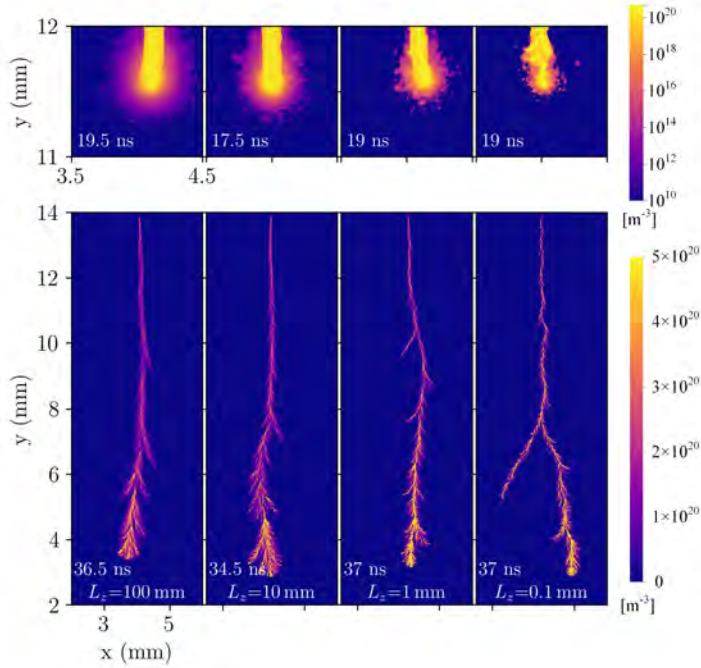
Figure 6.6: The effect of the parameter L_z on 2D particle simulations. L_z controls the amount of particle noise, see section 6.2.1. Electron densities are shown when streamer heads are approximately at y = 11.5 mm (top, logarithmic scale) and at y = 3 mm (bottom, linear scale).

regime, the streamer is not self-sustained by photoionization, so there is only limited growth due to a number of background free electrons.

The lowest voltage for the streamer to cross the gap was 31.2 kV, which corresponds to a background field $E_{bg} = 1.95$ kV/mm close to the breakdown field $E_{bd} = 2.2$ kV/mm. This is consistent with the experimental observation in [102] that the positive streamers in CO_2 could only cross the gap when E_{bg} was close to E_{bd}, using a quasi-uniform field setup. However, we emphasize that we cannot quantitatively compare our results against experiments since we use a 2D Cartesian model in which field enhancement is significantly lower than in 3D, see section 6.4.2.

6.5   Conclusions

We have performed 2D PIC-MCC simulations of positive streamer discharges in CO_2, in which we included photoionization based on the measurements of Przybylski [107] and Teich [108]. In our simulations photoionization was able to sustain positive streamer growth in CO_2. Such self-sustained growth only

occurred in background fields close to the breakdown threshold, which can be attributed to two main causes: first, the short absorption distance of ionizing photons, and second, the use of a 2D Cartesian model, in which electric field enhancement is weaker than in 3D. We have presented an approximate criterion for self-sustained discharge growth due to photoionization, based on the idea that a single photoionization event should produce on average at least one additional photoionization event. We have also discussed the significant uncertainties in photoionization parameters for CO_2.

Chapter 7

Conclusions and outlook

7.1 Conclusions

This thesis is centered around simulations of streamer discharges, encompassing four key aspects. Firstly, it involves the comparison between simulations and experimental observations of positive streamers in air, aiming at validating our fluid model. Secondly, it explores the characteristics of steady and stagnating positive streamers, delving into how their propagation relates to the background electric fields. Thirdly, it investigates the dynamics of streamer discharges interacting with dielectrics, aiming to unravel the complex influences of different physical mechanisms. Lastly, it examines the effect of photoionization on the propagation of positive streamers in CO_2 through particle simulations, and proposes a self-sustaining criterion for streamer discharges in CO_2. By addressing these four aspects, this thesis contributes to the comprehensive understanding of streamer discharge phenomena.

Macroscopic properties of streamers, such as their velocities and radii, are determined by the movement and collisions of charged particles. The behavior of these particles is influenced by external factors, such as applied voltages, as well as the properties of the surrounding medium, including gas compositions, temperatures, pressures, and the presence of nearby dielectrics. Consequently, these factors also influence streamer properties. The above notion has been demonstrated throughout the individual chapters of this thesis. Chapter 3 specifically shows the effect of applied voltages and gas temperatures on streamer properties. Chapter 5 demonstrates that the presence of a nearby dielectric can significantly influence the propagation of streamers by altering the electric field profile around the streamer head. Chapter 6 highlights that the morphology of streamers in CO_2 can differ significantly from those in air, suggesting that the gas composition plays a crucial role in determining streamer properties. Additionally, chapter 4 exhibits a complex relationship between the background electric field and the streamer properties, including velocity, radius and the maximum electric field,

addressing the nonlinear response of streamer properties to external conditions. After the general conclusion above, we summarize the most important findings from each chapter below:

- **Chapter 3:** The comparison between simulations and experiments of single positive streamer discharges in air revealed good qualitative agreement in terms of optical emission profiles, streamer velocity, and radius during the entire evolution. Quantitatively, the simulated streamer velocity was approximately 20-30% lower at the same streamer length, and the simulated radius was about 1 mm (20-30%) smaller. The study investigated the influence of various parameters, such as transport data, background ionization levels, photoionization rates, gas temperatures, voltage rise time, and voltage boundary conditions, on the agreement between the model and experiment. It was noted that the observed discrepancies might be partially attributed to an increase in gas temperature due to the experimental repetition frequency of 50 Hz.

- **Chapter 4:** Steady positive streamers at different constant velocities were obtained in background electric fields ranging from $4.1\,\text{kV/cm}$ to $5.4\,\text{kV/cm}$, which corresponds well with experimental stability fields. Faster steady streamers have a larger radius, a lower maximal electric field, a longer effective length and can propagate in a lower background electric field, indicating that there is no unique stability field. Behind the streamer head, electron densities decrease due to attachment and recombination, and the electric field relaxes back to the background electric field. A faster streamer thus has a longer conductive length. A lower background electric field is therefore sufficient to get a similar amount of electric field enhancement. This is supported by the observation that steady streamers in N_2-O_2 mixtures with lower O_2 content than air require lower background electric fields. In the case of a stagnated streamer, the average background electric field measured between the streamer head and tail resembles the empirically determined stability field.

- **Chapter 5:** A 2D fluid model for surface discharges was developed based on the Afivo-streamer code. The characteristics of positive and negative surface discharges were studied in a parallel-plate geometry, with a flat dielectric between the two electrodes. The attraction of streamers to the dielectric was mainly electrostatic. Compared to gas streamers, both positive and negative surface streamers have a smaller radius, a higher maximum electric field, a higher electron density and a higher propagation velocity. A narrow gap with a high field and a low electron density occurs between positive streamer heads and dielectrics, while the negative surface streamer can touch the dielectric. Photoemission can accelerate the inception of positive streamers near dielectrics. Nevertheless, the increase

in streamer velocities due to ion-induced and photo-induced electron emission from the dielectric is limited, as photoionization plays a dominant role in streamer growth. Additionally, the presence of preset opposite-polarity surface charge promotes the development of streamers around dielectrics, whereas same-polarity surface charge delays or inhibits surface discharges.

- **Chapter 6:** Photoionization in CO_2 is significantly weaker compared to air because fewer ionizing photons are produced and because their absorption distance is much shorter. To investigate the effect of photoionization in CO_2, a Monte Carlo photoionization model was developed. By conducting PIC-MCC simulations incorporating this novel photoionization model, we found even a small amount of photoionization was able to sustain positive streamer growth in CO_2, but this required a higher electric field around the streamer head than in air.

7.2 Outlook

Improving simulation accuracy through new measurements of cross-sections and photoionization parameters: The need for new measurements on cross-sections and photoionization parameters arises from the dependence of simulation accuracy on accurate input data. Existing cross-section databases for gases like N_2 and O_2 were mostly obtained decades ago, while data for popular insulating gases such as CO_2, SF_6, and C_4F_7N are limited. Furthermore, there is a lack of available data on photoionization parameters of gases other than N_2-O_2 mixtures. Evaluating the accuracy and uncertainty of the existing data poses challenges. Obtaining more accurate input data would enhance the validation of simulation models and enable streamer simulations in a broader range of gases.

Considerations for three-dimensional simulations: Three-dimensional simulations should be considered if they are feasible within reasonable cost for the following reasons. Firstly, branching streamers and non-axisymmetric streamers, such as surface discharges, are more prevalent in nature and laboratory settings than single-filament streamers. Accurate depiction of these streamers requires the use of 3D models. Secondly, studying branching streamers can lead to new insights and findings that go beyond the understanding of single-filament streamers. For example, it could be possible that due to repeated branching, streamers in moderately high background fields will not continually accelerate, but on average obtain a certain velocity and radius. Another interesting aspect is how the presence of multiple streamers changes the background field required for their collective propagation, i.e., the stability field. Furthermore, in a surface discharge, the interaction between surface streamers and gas-phase streamers can

only be described in 3D. Hence 3D simulations are essential for investigating surface discharges.

Choosing proper boundary conditions in streamer simulations: Boundary conditions are essential for solving partial differential equations. The selection of boundary conditions in streamer simulations can impact the computational results. In section 3.4.9, it was observed that using different boundary conditions, such as homogeneous Neumann or Dirichlet conditions, on the radial boundary of a 2D asymmetric configuration led to slight variations in streamer velocities. Additionally, the selection of boundary conditions becomes critical for specific scenarios. For instance, for surface discharges, the boundary condition at the gas-dielectric interface directly influences the accumulation of surface charge on the dielectric surface and consequently affects the accuracy of electric field calculations. However, how to properly set the boundary condition remains unclear due to lack of the secondary emission data. New measurements are required regarding this aspect. Numerically, boundary conditions for the electron flux from the gas side towards a dielectric surface in a fluid model can be refined by comparing fluid and particle simulations.

Bibliography

[1] Yuri P Raizer. Gas Discharge Physics. Springer-Verlag, Berlin; New York, 1991. ISBN 978-0-387-19462-2 978-3-540-19462-0.

[2] H. Raether. Die entwicklung der elektronenlawine in den funkenkanal. Zeitschrift für Physik, 112(7):464–489, Jul 1939. doi:10.1007/BF01340229.

[3] Leonard B. Loeb and Arthur F. Kip. Electrical discharges in air at atmospheric pressure the nature of the positive and negative point-to-plane coronas and the mechanism of spark propagation. Journal of Applied Physics, 10(3):142–160, Mar 1939. doi:10.1063/1.1707290.

[4] Leonard B. Loeb and John M. Meek. The mechanism of spark discharge in air at atmospheric pressure. i. Journal of Applied Physics, 11(6):438–447, Jun 1940. doi:10.1063/1.1712792.

[5] Leonard B. Loeb. Streamer breakdown and sparking thresholds. Physical Review, 81(2):287–287, Jan 1951. doi:10.1103/PhysRev.81.287.

[6] Sander Nijdam, Jannis Teunissen, and Ute Ebert. The physics of streamer discharge phenomena. Plasma Sources Science and Technology, 29(10): 103001, November 2020. doi:10.1088/1361-6595/abaa05.

[7] T M P Briels, J Kos, G J J Winands, E M van Veldhuizen, and U Ebert. Positive and negative streamers in ambient air: Measuring diameter, velocity and dissipated energy. Journal of Physics D: Applied Physics, 41 (23):234004, December 2008. doi:10.1088/0022-3727/41/23/234004.

[8] S V Pancheshnyi, S M Starikovskaia, and A Yu Starikovskii. Role of photoionization processes in propagation of cathode-directed streamer. Journal of Physics D: Applied Physics, 34(1):105, jan 2001. doi:10.1088/0022-3727/34/1/317.

[9] Ningyu Liu and Victor P. Pasko. Effects of photoionization on propagation and branching of positive and negative streamers in sprites. Journal of Geophysical Research: Space Physics, 109(A4), 2004. doi:https://doi.org/10.1029/2003JA010064.

[10] Ute Ebert, Sander Nijdam, Chao Li, Alejandro Luque, Tanja Briels, and Eddie van Veldhuizen. Review of recent results on streamer discharges and discussion of their relevance for sprites and lightning. Journal of Geophysical Research: Space Physics, 115(A7), 2010. doi:10.1029/2009JA014867.

[11] N. A. Popov. Kinetics of plasma-assisted combustion: Effect of non-equilibrium excitation on the ignition and oxidation of combustible mixtures. Plasma Sources Science and Technology, 25(4):043002, May 2016. doi:10.1088/0963-252/25/4/043002.

[12] L. Bárdos and H. Baránková. Cold atmospheric plasma: Sources, processes, and applications. Thin Solid Films, 518(23):6705–6713, September 2010. doi:10.1016/j.tsf.2010.07.044.

[13] Mounir Laroussi. From Killing Bacteria to Destroying Cancer Cells: 20 Years of Plasma Medicine. Plasma Processes and Polymers, 11(12):1138–1141, 2014. doi:10.1002/ppap.201400152.

[14] P. J. Bruggeman, M. J. Kushner, B. R. Locke, J. G. E. Gardeniers, W. G. Graham, D. B. Graves, R. C. H. M. Hofman-Caris, D. Maric, J. P. Reid, E. Ceriani, D. Fernandez Rivas, J. E. Foster, S. C. Garrick, Y. Gorbanev, S. Hamaguchi, F. Iza, H. Jablonowski, E. Klimova, J. Kolb, F. Krcma, P. Lukes, Z. Machala, I. Marinov, D. Mariotti, S. Mededovic Thagard, D. Minakata, E. C. Neyts, J. Pawlat, Z. Lj Petrovic, R. Pflieger, S. Reuter, D. C. Schram, S. Schröter, M. Shiraiwa, B. Tarabová, P. A. Tsai, J. R. R. Verlet, T. von Woedtke, K. R. Wilson, K. Yasui, and G. Zvereva. Plasma–liquid interactions: A review and roadmap. Plasma Sources Science and Technology, 25(5):053002, September 2016. doi:10.1088/0963-0252/25/5/053002.

[15] Natalia Yu Babaeva and George V Naidis. Universal nature and specific features of streamers in various dielectric media. Journal of Physics D: Applied Physics, 54(22):223002, June 2021. doi:10.1088/1361-6463/abe9e0.

[16] Ryo Ono. Optical diagnostics of reactive species in atmospheric-pressure nonthermal plasma. Journal of Physics D: Applied Physics, 49(8):083001, jan 2016. doi:10.1088/0022-3727/49/8/083001.

[17] Patrick J. Roache. Verification and Validation in Computational Science and Engineering. Hermosa Pub, Albuquerque, N.M, 0 edition edition, August 1998. ISBN 978-0-913478-08-0.

[18] S. Pancheshnyi, M. Nudnova, and A. Starikovskii. Development of a cathode-directed streamer discharge in air at different pressures: Exper-

iment and comparison with direct numerical simulation. Physical Review
E, 71(1), January 2005. doi:10.1103/PhysRevE.71.016407.

[19] Alejandro Luque, Valeria Ratushnaya, and Ute Ebert. Positive and
negative streamers in ambient air: Modelling evolution and velocities.
Journal of Physics D: Applied Physics, 41(23):234005, December 2008.
doi:10.1088/0022-3727/41/23/234005.

[20] Atsushi Komuro, Ryo Ono, and Tetsuji Oda. Numerical simulation for
production of O and N radicals in an atmospheric-pressure streamer dis-
charge. Journal of Physics D: Applied Physics, 45(26):265201, July 2012.
doi:10.1088/0022-3727/45/26/265201.

[21] Atsushi Komuro, Ryo Ono, and Tetsuji Oda. Effects of pulse voltage
rise rate on velocity, diameter and radical production of an atmospheric-
pressure streamer discharge. Plasma Sources Science and Technology, 22
(4):045002, Jun 2013. doi:10.1088/0963-0252/22/4/045002.

[22] Atsushi Komuro, Shuto Matsuyuki, and Akira Ando. Comparison of
simulations and experiments on the axial distributions of the electron
density in a point-to-plane streamer discharge at atmospheric pressure.
Journal of Physics D: Applied Physics, 51(44):445204, November 2018.
doi:10.1088/1361-6463/aae1ea.

[23] O. Eichwald, O. Ducasse, D. Dubois, A. Abahazem, N. Merbahi, M. Ben-
henni, and M. Yousfi. Experimental analysis and modelling of positive
streamer in air: Towards an estimation of O and N radical production.
Journal of Physics D: Applied Physics, 41(23):234002, November 2008.
doi:10.1088/0022-3727/41/23/234002.

[24] S Nijdam, J Teunissen, E Takahashi, and U Ebert. The role of
free electrons in the guiding of positive streamers. Plasma Sources
Science and Technology, 25(4):044001, August 2016. doi:10.1088/0963-
0252/25/4/044001.

[25] E Marode, Ph Dessante, and P Tardiveau. 2D positive streamer mod-
elling in NTP air under extreme pulse fronts. What about runaway elec-
trons? Plasma Sources Science and Technology, 25(6):064004, October
2016. doi:10.1088/0963-0252/25/6/064004.

[26] Alexandra Brisset, Kristaq Gazeli, Lionel Magne, Stéphane Pasquiers, Pas-
cal Jeanney, Emmanuel Marode, and Pierre Tardiveau. Modification of the
electric field distribution in a diffuse streamer-induced discharge under ex-
treme overvoltage. Plasma Sources Science and Technology, 28(5):055016,
May 2019. doi:10.1088/1361-6595/ab1989.

[27] Yifei Zhu, Xiancong Chen, Yun Wu, Jinbo Hao, Xiaoguang Ma, Pengfei Lu, and Pierre Tardiveau. Simulation of the ionization wave discharges: A direct comparison between the fluid model and E–FISH measurements. Plasma Sources Science and Technology, 2021. doi:10.1088/1361-6595/ac0714.

[28] Fabien Tholin, Diane L. Rusterholtz, Deanna A. Lacoste, David Z. Pai, Sebastien Celestin, Julien Jarrige, Gabi D. Stancu, Anne Bourdon, and Christophe O. Laux. Images of a Nanosecond Repetitively Pulsed Glow Discharge Between Two Point Electrodes in Air at 300 K and at Atmospheric Pressure. IEEE Transactions on Plasma Science, 39(11):2254–2255, November 2011. doi:10.1109/TPS.2011.2158855.

[29] Franois Pechereau, Pierre Le Delliou, Jaroslav Jánský, Pierre Tardiveau, Stéphane Pasquiers, and Anne Bourdon. Large Conical Discharge Structure of an Air Discharge at Atmospheric Pressure in a Point-to-Plane Geometry. IEEE Transactions on Plasma Science, 42(10):2346–2347, October 2014. doi:10.1109/TPS.2014.2309981.

[30] Ryo Ono and Atsushi Komuro. Generation of the single-filament pulsed positive streamer discharge in atmospheric-pressure air and its comparison with two-dimensional simulation. Journal of Physics D: Applied Physics, 53(3):035202, January 2020. doi:10.1088/1361-6463/ab4e65.

[31] M. Yousfi, O. Eichwald, N. Merbahi, and N. Jomaa. Analysis of ionization wave dynamics in low-temperature plasma jets from fluid modeling supported by experimental investigations. Plasma Sources Science and Technology, 21(4):045003, June 2012. doi:10.1088/0963-0252/21/4/045003.

[32] Marlous Hofmans, Pedro Viegas, Olivier van Rooij, Bart Klarenaar, Olivier Guaitella, Anne Bourdon, and Ana Sobota. Characterization of a kHz atmospheric pressure plasma jet: comparison of discharge propagation parameters in experiments and simulations without target. Plasma Sources Science and Technology, 29(3):034003, March 2020. doi:10.1088/1361-6595/ab6d49. Publisher: IOP Publishing.

[33] Pedro Viegas, Marlous Hofmans, Olivier van Rooij, Adam Obrusník, Bart L M Klarenaar, Zdenek Bonaventura, Olivier Guaitella, Ana Sobota, and Anne Bourdon. Interaction of an atmospheric pressure plasma jet with grounded and floating metallic targets: simulations and experiments. Plasma Sources Science and Technology, 29(9):095011, Sep 2020. doi:10.1088/1361-6595/aba7ec.

[34] Chao Li, Jannis Teunissen, Margreet Nool, Willem Hundsdorfer, and Ute Ebert. A comparison of 3D particle, fluid and hybrid simulations for negative streamers. Plasma Sources Sci. Technol., page 15, 2012.

[35] Aram H Markosyan, Jannis Teunissen, Saša Dujko, and Ute Ebert. Comparing plasma fluid models of different order for 1D streamer ionization fronts. Plasma Sources Science and Technology, 24(6):065002, October 2015. doi:10.1088/0963-0252/24/6/065002.

[36] S Dujko, A H Markosyan, R D White, and U Ebert. High-order fluid model for streamer discharges: I. Derivation of model and transport data. Journal of Physics D: Applied Physics, 46(47):475202, November 2013. doi:10.1088/0022-3727/46/47/475202.

[37] B Bagheri, J Teunissen, U Ebert, M M Becker, S Chen, O Ducasse, O Eichwald, D Loffhagen, A Luque, D Mihailova, J M Plewa, J van Dijk, and M Yousfi. Comparison of six simulation codes for positive streamers in air. Plasma Sources Science and Technology, 27(9):095002, September 2018. doi:10.1088/1361-6595/aad768.

[38] B Bagheri and J Teunissen. The effect of the stochasticity of photoionization on 3D streamer simulations. Plasma Sources Science and Technology, 28(4):045013, April 2019. doi:10.1088/1361-6595/ab1331.

[39] Baohong Guo, Xiaoran Li, Ute Ebert, and Jannis Teunissen. A computational study of accelerating, steady and fading negative streamers in ambient air. Plasma Sources Science and Technology, 31(9):095011, Sep 2022. doi:10.1088/1361-6595/ac8e2e.

[40] I. Gallimberti. The mechanism of the long spark formation. Le Journal de Physique Colloques, 40(C7):C7–193–C7–250, July 1979. doi:10.1051/jphyscol:19797440.

[41] C. T. Phelps. Field-enhanced propagation of corona streamers. Journal of Geophysical Research (1896-1977), 76(24):5799–5806, 1971. doi:10.1029/JC076i024p05799.

[42] R. F. Griffiths and C. T. Phelps. The effects of air pressure and water vapour content on the propagation of positive corona streamers, and their implications to lightning initiation: CORONA STREAMERS. Quarterly Journal of the Royal Meteorological Society, 102(432):419–426, April 1976. doi:10.1002/qj.49710243211.

[43] N.L. Allen and M. Boutlendj. Study of the electric fields required for streamer propagation in humid air. IEE Proceedings A Science, Measurement and Technology, 138(1):37, 1991. doi:10.1049/ip-a-3.1991.0005.

[44] N L Allen and A Ghaffar. The conditions required for the propagation of a cathode-directed positive streamer in air. Journal of Physics D: Applied Physics, 28(2):331–337, February 1995. doi:10.1088/0022-3727/28/2/016.

[45] E. M. van Veldhuizen and W. R. Rutgers. Pulsed positive corona streamer propagation and branching. Journal of Physics D: Applied Physics, 35(17): 2169–2179, August 2002. doi:10.1088/0022-3727/35/17/313.

[46] Martin Seeger, Torsten Votteler, Jonas Ekeberg, Sergey Pancheshnyi, and Luis Sánchez. Streamer and leader breakdown in air at atmospheric pressure in strongly non-uniform fields in gaps less than one metre. IEEE Transactions on Dielectrics and Electrical Insulation, 25(6):2147–2156, December 2018. doi:10.1109/TDEI.2018.007246.

[47] Jianqi Qin and Victor P. Pasko. On the propagation of streamers in electrical discharges. Journal of Physics D: Applied Physics, 47(43):435202, October 2014. doi:10.1088/0022-3727/47/43/435202.

[48] Hani Francisco, Jannis Teunissen, Behnaz Bagheri, and Ute Ebert. Simulations of positive streamers in air in different electric fields: Steady motion of solitary streamer heads and the stability field. Plasma Sources Science and Technology, 30(11):115007, November 2021. doi:10.1088/1361-6595/ac2f76.

[49] S. V. Pancheshnyi and A. Yu Starikovskii. Stagnation dynamics of a cathode-directed streamer discharge in air. Plasma Sources Science and Technology, 13(3):B1–B5, July 2004. doi:10.1088/0963-0252/13/3/B01.

[50] A. Yu. Starikovskiy, N. L. Aleksandrov, and M. N. Shneider. Simulation of decelerating streamers in inhomogeneous atmosphere with implications for runaway electron generation. Journal of Applied Physics, 129(6):063301, February 2021. doi:10.1063/5.0037669.

[51] Mojtaba Niknezhad, Olivier Chanrion, Joachim Holbøll, and Torsten Neubert. Underlying mechanism of the stagnation of positive streamers. Plasma Sources Science and Technology, October 2021. doi:10.1088/1361-6595/ac3214.

[52] G. V. Naidis. Positive and negative streamers in air: Velocity-diameter relation. Physical Review E, 79(5), May 2009. doi:10.1103/PhysRevE.79.057401.

[53] A. H. Cookson. ELECTRICAL BREAKDOWN FOR UNIFORM FIELDS IN COMPRESSED GASES. Proceedings of the Institution of Electrical Engineers-London, 117(1):269–+, 1970. doi:10.1049/piee.1970.0058.

[54] A. H. Cookson. REVIEW OF HIGH-VOLTAGE GAS-BREAKDOWN AND INSULATORS IN COMPRESSED GAS. Iee Proceedings-a-Science Measurement and Technology, 128(4):303–312, 1981. doi:10.1049/ip-a-1.1981.0045.

[55] T. S. Sudarshan and R. A. Dougal. Mechanisms of Surface Flashover Along Solid Dielectrics in Compressed Gases: A Review. IEEE Transactions on Electrical Insulation, EI-21(5):727–746, 1986. doi:10.1109/TEI.1986.348922.

[56] Xiao-Ran Li, Zhe Liu, Wen-Dong Li, Guang-Yu Sun, Jian-Yi Xue, Chao Wang, and Guan-Jun Zhang. 3D printing fabrication of conductivity non-uniform insulator for surface flashover mitigation. IEEE Transactions on Dielectrics and Electrical Insulation, 26(4):1172–1180, August 2019. doi:10.1109/TDEI.2019.007938.

[57] Chuanyang Li, Chuanjie Lin, Geng Chen, Youping Tu, Yao Zhou, Qi Li, Bo Zhang, and Jinliang He. Field-dependent charging phenomenon of HVDC spacers based on dominant charge behaviors. Applied Physics Letters, 114(20):202904, May 2019. doi:10.1063/1.5096228.

[58] A. Sobota, E. M. van Veldhuizen, and W. W. Stoffels. Discharge Ignition Near a Dielectric. IEEE Transactions on Plasma Science, 36(4):912–913, August 2008. doi:10.1109/TPS.2008.924614.

[59] D. J. M. Trienekens, S. Nijdam, and U. Ebert. Stroboscopic Images of Streamers Through Air and Over Dielectric Surfaces. IEEE Transactions on Plasma Science, 42(10):2400–2401, October 2014. doi:10.1109/TPS.2014.2335615.

[60] A Sobota, A Lebouvier, N J Kramer, E M van Veldhuizen, W W Stoffels, F Manders, and M Haverlag. Speed of streamers in argon over a flat surface of a dielectric. Journal of Physics D: Applied Physics, 42(1):015211, January 2009. doi:10.1088/0022-3727/42/1/015211.

[61] A Dubinova, D Trienekens, U Ebert, S Nijdam, and T Christen. Pulsed positive discharges in air at moderate pressures near a dielectric rod. Plasma Sources Science and Technology, 25(5):055021, September 2016. doi:10.1088/0963-0252/25/5/055021.

[62] N. L. Allen and P. N. Mikropoulos. Streamer propagation along insulating surfaces. IEEE Transactions on Dielectrics and Electrical Insulation, 6(3): 357–362, 1999. doi:10.1109/94.775623.

[63] X. Meng, H. Mei, C. Chen, L. Wang, Z. Guan, and J. Zhou. Characteristics of streamer propagation along the insulation surface: Influence of dielectric

material. *IEEE Transactions on Dielectrics and Electrical Insulation*, 22 (2):1193–1203, 2015. doi:10.1109/TDEI.2015.7076822.

[64] S. Kumara, S. Alam, I. R. Hoque, Y. V. Serdyuk, and S. M. Gubanski. DC Flashover Characteristics of a Polymeric Insulator in Presence of Surface Charges. *IEEE Transactions on Dielectrics and Electrical Insulation*, 19 (3):1084–1090, June 2012. doi:10.1109/tdei.2012.6215116.

[65] Chuanyang Li, Jun Hu, Chuanjie Lin, Boya Zhang, Guixin Zhang, and Jinliang He. Surface charge migration and dc surface flashover of surface-modified epoxy-based insulators. *Journal of Physics D: Applied Physics*, 50(6):065301, January 2017. doi:10.1088/1361-6463/aa5207.

[66] Tao Shao, Fei Kong, Haofan Lin, Yiyang Ma, Qing Xie, and Cheng Zhang. Correlation between surface charge and DC surface flashover of plasma treated epoxy resin. *IEEE Transactions on Dielectrics and Electrical Insulation*, 25(4):1267–1274, August 2018. doi:10.1109/TDEI.2017.007132.

[67] Yanqin LIU, Guangning WU, Guoqiang GAO, Jianyi XUE, Yongqiang KANG, and Chaoqun SHI. Surface charge accumulation behavior and its influence on surface flashover performance of Al2O3-filled epoxy resin insulators under DC voltages. *Plasma Science and Technology*, 21(5):055501, March 2019. doi:10.1088/2058-6272/aafdf7.

[68] Bangdou Huang, Cheng Zhang, Igor Adamovich, Yuri Akishev, and Tao Shao. Surface ionization wave propagation in the nanosecond pulsed surface dielectric barrier discharge: The influence of dielectric material and pulse repetition rate. *Plasma Sources Science and Technology*, 29(4):044001, March 2020. doi:10.1088/1361-6595/ab7854.

[69] Roy E Jorgenson, Larry K Warne, Andreas A Neuber, John Krile, James Dickens, and Hermann Krompholz. Effect of Dielectric Photoemission on Surface Breakdown: An LDRD Report. Technical Report SAND2003-1731, 811483, May 2003.

[70] Jaroslav Jánský, Fabien Tholin, Zdeněk Bonaventura, and Anne Bourdon. Simulation of the discharge propagation in a capillary tube in air at atmospheric pressure. *Journal of Physics D: Applied Physics*, 43(39):395201, October 2010. doi:10.1088/0022-3727/43/39/395201.

[71] Natalia Yu Babaeva, Dmitry V Tereshonok, and George V Naidis. Fluid and hybrid modeling of nanosecond surface discharges: Effect of polarity and secondary electrons emission. *Plasma Sources Science and Technology*, 25(4):044008, July 2016. doi:10.1088/0963-0252/25/4/044008.

[72] G E Georghiou, A P Papadakis, R Morrow, and A C Metaxas. Numerical modelling of atmospheric pressure gas discharges leading to plasma production. Journal of Physics D: Applied Physics, 38(20):R303–R328, October 2005. doi:10.1088/0022-3727/38/20/R01.

[73] Guang-Yu Sun, Bao-Hong Guo, Bai-Peng Song, Guo-Qiang Su, Hai-Bao Mu, and Guan-Jun Zhang. Simulation on the dynamic charge behavior of vacuum flashover developing across insulator involving outgassing. Physics of Plasmas, 25(6):063502, June 2018. doi:10.1063/1.5025209.

[74] Wenxia Sima, Chunxiang Liu, Ming Yang, Qianqiu Shao, Hang Xu, and Sanwei Liu. Plasma model of discharge along a dielectric surface in N_2/O_2 mixtures. Physics of Plasmas, 23(6):063508, June 2016. doi:10.1063/1.4949767.

[75] G. Zhang, G. Su, B. Song, and H. Mu. Pulsed flashover across a solid dielectric in vacuum. IEEE Transactions on Dielectrics and Electrical Insulation, 25(6):2321–2339, December 2018. doi:10.1109/TDEI.2018.007133.

[76] Anbang Sun, Markus M Becker, and D Loffhagen. PIC/MCC simulation of capacitively coupled discharges in helium: Boundary effects. Plasma Sources Science and Technology, 27(5):054002, May 2018. doi:10.1088/1361-6595/aac30a.

[77] S. Celestin, Z. Bonaventura, O. Guaitella, A. Rousseau, and A. Bourdon. Influence of surface charges on the structure of a dielectric barrier discharge in air at atmospheric pressure: Experiment and modeling. The European Physical Journal Applied Physics, 47(2):22810, August 2009. doi:10.1051/epjap/2009078.

[78] Hans Kristian Meyer, Frank Mauseth, Robert Marskar, Atle Pedersen, and Andreas Blaszczyk. Streamer and surface charge dynamics in non-uniform air gaps with a dielectric barrier. IEEE Transactions on Dielectrics and Electrical Insulation, 26(4):1163–1171, Aug 2019. doi:10.1109/tdei.2019.007929.

[79] T. N. Tran, I. O. Golosnoy, P. L. Lewin, and G. E. Georghiou. Numerical modelling of negative discharges in air with experimental validation. Journal of Physics D: Applied Physics, 44(1):015203, December 2010. doi:10.1088/0022-3727/44/1/015203.

[80] Wenxia Sima, Chunxiang Liu, Ming Yang, Hang Xu, and Qianqiu Shao. Study of a Nonequilibrium Plasma Model of Surface Discharge and the Influencing Factors. IEEE Trans. Plasma Sci., 45(6):906–912, June 2017. doi:10.1109/TPS.2017.2690901. WOS:000403486500001.

[81] Natalia Yu Babaeva. Hot secondary electrons in dielectric barrier discharges treated with monte carlo simulation: implication for fluxes to surfaces. Plasma Sources Science and Technology, 24(3):034012, Jun 2015. doi:10.1088/0963-0252/24/3/034012.

[82] Weizhuo Hua and Koji Fukagata. Near-surface electron transport and its influence on the discharge structure of nanosecond-pulsed dielectric-barrier-discharge under different electrode polarities. Physics of Plasmas, 26(1): 013514, January 2019. doi:10.1063/1.5058189.

[83] Natalia Yu Babaeva and Mark J Kushner. Reactive fluxes delivered by dielectric barrier discharge filaments to slightly wounded skin. Journal of Physics D: Applied Physics, 46(2):025401, January 2013. doi:10.1088/0022-3727/46/2/025401.

[84] Wei Tian and Mark J Kushner. Atmospheric pressure dielectric barrier discharges interacting with liquid covered tissue. Journal of Physics D: Applied Physics, 47(16):165201, Apr 2014. doi:10.1088/0022-3727/47/16/165201.

[85] Olga Stepanova, Mikhail Pinchuk, Alexander Astafiev, and Zhaoquan Chen. A streamer behavior evolution during an applied voltage cycle in helium and argon atmospheric pressure plasma jets fed by dbd. Japanese Journal of Applied Physics, 59(SH):SHHC03, mar 2020. doi:10.35848/1347-4065/ab75b4.

[86] Junhong Chen, Jinshu Li, Junhao Dong, Peng Sun, Junbo Deng, Yuan Li, and Guan-Jun Zhang. Surface discharge propagation in c 4 f 7 n/co 2 mixture under positive impulse voltages. Applied Physics Letters, 120(6): 061601, Feb 2022. doi:10.1063/5.0081032.

[87] Zheng Zhao, Zhifeng Dai, Anbang Sun, and Jiangtao Li. Streamer-to-precursor transition in n2–sf6 mixtures under positive repetitive submicrosecond pulses. High Voltage, 7(2):382–389, 2022. doi:https://doi.org/10.1049/hve2.12119.

[88] S Nijdam, F M J H van de Wetering, R Blanc, E M van Veldhuizen, and U Ebert. Probing photo-ionization: Experiments on positive streamers in pure gases and mixtures. Journal of Physics D: Applied Physics, 43(14): 145204, April 2010. doi:10.1088/0022-3727/43/14/145204.

[89] Mb Zheleznyak, Ak Mnatsakanyan, and Sv Sizykh. Photo-Ionization of Nitrogen and Oxygen Mixtures by Radiation from a Gas-Discharge. High Temperature, 20(3):357–362, 1982.

[90] Yulin Guo, Yanru Li, Yifei Zhu, and Anbang Sun. A numerical and experimental study on positive diffusive ionization waves in different n2/o2 mixtures: the role of photoionization. Plasma Sources Science and Technology, 32(2):025003, feb 2023. doi:10.1088/1361-6595/acb813.

[91] Xiancong Chen, Yifei Zhu, Yun Wu, Jinbo Hao, Xiaoguang Ma, and Pengfei Lu. Modeling of fast ionization waves in pure nitrogen at moderate pressure. Plasma Sources Science and Technology, 30(6):065002, jun 2021. doi:10.1088/1361-6595/abe612.

[92] Sergey Pancheshnyi. Photoionization produced by low-current discharges in O2, air, N2and CO2. Plasma Sources Science and Technology, 24(1):015023, December 2014. doi:10.1088/0963-0252/24/1/015023.

[93] Martin Seeger. Perspectives on Research on High Voltage Gas Circuit Breakers. Plasma Chemistry and Plasma Processing, 35(3):527–541, May 2015. doi:10.1007/s11090-014-9595-4.

[94] Toshiro Matsumura, Yasunobu Yokomizu, Pablo C. Almiron, Kazuma Yamamoto, Daisuke Ohta, and Masatoyo Shibuya. Breakdown Voltage of CO2 at Temperatures around 4000 K and in Range from 300 to 700 K. IEEJ Transactions on Power and Energy, 125(11):1063–1069, 2005. doi:10.1541/ieejpes.125.1063.

[95] S. Okabe, H. Goshima, A. Tanimura, S. Tsuru, Y. Yaegashi, E. Fujie, and H. Okubo. Fundamental insulation characteristic of high-pressure CO/sub 2/ gas under actual equipment conditions. IEEE Transactions on Dielectrics and Electrical Insulation, 14(1):83–90, February 2007. doi:10.1109/TDEI.2007.302875.

[96] H. Goshima, S. Okabe, T. Ueda, H. Morii, N. Yamachi, K. Takahata, and M. Hikita. Fundamental insulation characteristics of high-pressure CO2 gas for gas-insulated power equipment - effect of coating conductor on insulation performance and effect of decomposition products on creeping insulation of spacer -. IEEE Transactions on Dielectrics and Electrical Insulation, 15(4):1023–1030, August 2008. doi:10.1109/TDEI.2008.4591223.

[97] M. Hikita, S. Ohtsuka, N. Yokoyama, S. Okabe, and S. Kaneko. Effect of electrode surface roughness and dielectric coating on breakdown characteristics of high pressure CO2 and N2 in a quasi-uniform electric field. IEEE Transactions on Dielectrics and Electrical Insulation, 15(1):243–250, February 2008. doi:10.1109/T-DEI.2008.4446757.

[98] J. Wada, G. Ueta, and S. Okabe. Evaluation of breakdown characteristics of CO2 gas for non-standard lightning impulse waveforms under non-uniform electric field - breakdown characteristics for single-frequency os-

cillation waveforms -. IEEE Transactions on Dielectrics and Electrical Insulation, 18(2):640–648, April 2011. doi:10.1109/TDEI.2011.5739471.

[99] Hao Sun, Mingzhe Rong, Yi Wu, Zhexin Chen, Fei Yang, Anthony B Murphy, and Hantian Zhang. Investigation on critical breakdown electric field of hot carbon dioxide for gas circuit breaker applications. Journal of Physics D: Applied Physics, 48(5):055201, 2015.

[100] Siddharth Kumar, Tom Huiskamp, A.J.M. Pemen, Martin Seeger, Juriy Pachin, and Christian M. Franck. Electrical Breakdown Study in CO2 and CO2-O2 Mixtures in AC, DC and Pulsed Electric Fields at 0.1–1 MPa Pressure. IEEE Transactions on Dielectrics and Electrical Insulation, 28 (1):158–166, February 2021. doi:10.1109/TDEI.2020.009115.

[101] Siddharth Kumar. Electrical Breakdown Investigation in CO2: At Room and High Temperatures for High-Voltage Equipment. Phd Thesis 1 (Research TU/e / Graduation TU/e), Eindhoven University of Technology, Eindhoven, December 2021.

[102] M. Seeger, J. Avaheden, S. Pancheshnyi, and T. Votteler. Streamer parameters and breakdown in CO2. Journal of Physics D: Applied Physics, 50 (1):015207, November 2016. doi:10.1088/1361-6463/50/1/015207.

[103] S Mirpour and S Nijdam. Investigating CO$_2$ streamer inception in repetitive pulsed discharges. Plasma Sources Science and Technology, 31(5): 055007, May 2022. doi:10.1088/1361-6595/ac6a0e.

[104] Dmitry Levko, Michael Pachuilo, and Laxminarayan L Raja. Particle-in-cell modeling of streamer branching in CO$_2$ gas. Journal of Physics D: Applied Physics, 50(35):354004, September 2017. doi:10.1088/1361-6463/aa7e6c.

[105] Behnaz Bagheri, Jannis Teunissen, and Ute Ebert. Simulation of positive streamers in CO$_2$ and in air: The role of photoionization or other electron sources. Plasma Sources Science and Technology, 29(12):125021, December 2020. doi:10.1088/1361-6595/abc93e.

[106] Xiaoran Li, Siebe Dijcks, Sander Nijdam, Anbang Sun, Ute Ebert, and Jannis Teunissen. Comparing simulations and experiments of positive streamers in air: Steps toward model validation. Plasma Sources Science and Technology, 30(9):095002, September 2021. doi:10.1088/1361-6595/ac1b36.

[107] A. Przybylski. Untersuchung über die gasionisierende Strahlung einer Entladung II. Zeitschrift für Physik, 168(5):504–515, October 1962. doi:10.1007/BF01378146.

[108] Timm H. Teich. Emission gasionisierender Strahlung aus Elektronenlawinen. Zeitschrift für Physik, 199(4):395–410, August 1967. doi:10.1007/BF01332288.

[109] Jannis Teunissen and Ute Ebert. Afivo: A framework for quadtree/octree AMR with shared-memory parallelization and geometric multigrid methods. Computer Physics Communications, 233:156–166, December 2018. doi:10.1016/j.cpc.2018.06.018.

[110] Zhen Wang, Anbang Sun, and Jannis Teunissen. A comparison of particle and fluid models for positive streamer discharges in air. Plasma Sources Science and Technology, 31(1):015012, January 2022. doi:10.1088/1361-6595/ac417b.

[111] Jannis Teunissen and Ute Ebert. Simulating streamer discharges in 3D with the parallel adaptive Afivo framework. Journal of Physics D: Applied Physics, 50(47):474001, November 2017. doi:10.1088/1361-6463/aa8faf.

[112] Jannis Teunissen and Ute Ebert. 3D PIC-MCC simulations of discharge inception around a sharp anode in nitrogen/oxygen mixtures. Plasma Sources Science and Technology, 25(4):044005, August 2016. doi:10.1088/0963-0252/25/4/044005.

[113] I A Kossyi, A Yu Kostinsky, A A Matveyev, and V P Silakov. Kinetic scheme of the non-equilibrium discharge in nitrogen-oxygen mixtures. Plasma Sources Science and Technology, 1(3):207–220, August 1992. doi:10.1088/0963-0252/1/3/011.

[114] Baohong Guo and Jannis Teunissen. A computational study on the energy efficiency of species production by single-pulse streamers in air. Plasma Sources Science and Technology, 32(2):025001, Feb 2023. doi:10.1088/1361-6595/acb462.

[115] A. V. Phelps and L. C. Pitchford. Anisotropic scattering of electrons by N 2 and its effect on electron transport. Physical Review A, 31(5):2932–2949, May 1985. doi:10.1103/PhysRevA.31.2932.

[116] G J M Hagelaar and L C Pitchford. Solving the Boltzmann equation to obtain electron transport coefficients and rate coefficients for fluid models. Plasma Sources Science and Technology, 14(4):722–733, November 2005. doi:10.1088/0963-0252/14/4/011.

[117] J. Stephens. A multi-term Boltzmann equation benchmark of electron-argon cross-sections for use in low temperature plasma models. Journal of Physics D: Applied Physics, 51(12):125203, March 2018. doi:10.1088/1361-6463/aaaf8b.

[118] A. Tejero-del-Caz, V. Guerra, D. Gonçalves, M. Lino da Silva, L. Marques, N. Pinhão, C. D. Pintassilgo, and L. L. Alves. The LisbOn KInetics Boltzmann solver. Plasma Sources Science and Technology, 28(4):043001, April 2019. doi:10.1088/1361-6595/ab0537.

[119] S. F. Biagi. Monte Carlo simulation of electron drift and diffusion in counting gases under the influence of electric and magnetic fields. Nuclear Instruments and Methods in Physics Research Section A: Accelerators, Spectrometers, Detectors and Associated Equipment, 421(1):234–240, January 1999. doi:10.1016/S0168-9002(98)01233-9.

[120] M. Rabie and C. M. Franck. METHES: A Monte Carlo collision code for the simulation of electron transport in low temperature plasmas. Computer Physics Communications, 203:268–277, June 2016. doi:10.1016/j.cpc.2016.02.022.

[121] S. Pancheshnyi, S. Biagi, M.C. Bordage, G.J.M. Hagelaar, W.L. Morgan, A.V. Phelps, and L.C. Pitchford. The LXCat project: Electron scattering cross sections and swarm parameters for low temperature plasma modeling. Chemical Physics, 398:148–153, April 2012. doi:10.1016/j.chemphys.2011.04.020.

[122] Emile Carbone, Wouter Graef, Gerjan Hagelaar, Daan Boer, Matthew M. Hopkins, Jacob C. Stephens, Benjamin T. Yee, Sergey Pancheshnyi, Jan van Dijk, and Leanne Pitchford. Data Needs for Modeling Low-Temperature Non-Equilibrium Plasmas: The LXCat Project, History, Perspectives and a Tutorial. Atoms, 9(1):16, March 2021. doi:10.3390/atoms9010016. Number: 1 Publisher: Multidisciplinary Digital Publishing Institute.

[123] Phelps database (N2,O2). www.lxcat.net, retrieved on January 19, 2021.

[124] L. L. Alves. The IST-LISBON database on LXCat. Journal of Physics: Conference Series, 565:012007, December 2014. doi:10.1088/1742-6596/565/1/012007. Publisher: IOP Publishing.

[125] J. Loureiro and C. M. Ferreira. Coupled electron energy and vibrational distribution functions in stationary N2discharges. Journal of Physics D: Applied Physics, 19(1):17–35, January 1986. doi:10.1088/0022-3727/19/1/007.

[126] Ist lisbon database (N2,O2). www.lxcat.net, retrieved on January 19, 2021.

[127] Morgan database (N2,O2). www.lxcat.net, retrieved on January 19, 2021.

[128] Triniti database (N2,O2). www.lxcat.net, retrieved on January 19, 2021.

[129] Biagi database (N2,O2). www.lxcat.net, retrieved on January 19, 2021.

[130] Loup Verlet. Computer "experiments" on classical fluids. i. thermodynamical properties of lennard-jones molecules. Phys. Rev., 159:98–103, Jul 1967. doi:10.1103/PhysRev.159.98.

[131] Katsuhisa Koura. Null-collision technique in the direct-simulation monte carlo method. The Physics of Fluids, 29(11):3509–3511, 1986. doi:10.1063/1.865826.

[132] Ulrich Trottenberg, Cornelius W Oosterlee, and Anton Schuller. Multigrid. Elsevier, 2000.

[133] A A Kulikovsky. The role of photoionization in positive streamer dynamics. Journal of Physics D: Applied Physics, 33(12):1514, jun 2000. doi:10.1088/0022-3727/33/12/314.

[134] M M Nudnova and A Yu Starikovskii. Streamer head structure: role of ionization and photoionization. Journal of Physics D: Applied Physics, 41 (23):234003, nov 2008. doi:10.1088/0022-3727/41/23/234003.

[135] A Bourdon, V P Pasko, N Y Liu, S Célestin, P Ségur, and E Marode. Efficient models for photoionization produced by non-thermal gas discharges in air based on radiative transfer and the Helmholtz equations. Plasma Sources Science and Technology, 16(3):656–678, August 2007. doi:10.1088/0963-0252/16/3/026.

[136] Alejandro Luque, Ute Ebert, Carolynne Montijn, and Willem Hundsdorfer. Photoionization in negative streamers: Fast computations and two propagation modes. Applied Physics Letters, 90(8):081501, February 2007. doi:10.1063/1.2435934.

[137] O. Chanrion and T. Neubert. A PIC-MCC code for simulation of streamer propagation in air. Journal of Computational Physics, 227(15):7222–7245, July 2008. doi:10.1016/j.jcp.2008.04.016.

[138] Andrew Fierro, Jacob Stephens, Sterling Beeson, James Dickens, and Andreas Neuber. Discrete photon implementation for plasma simulations. Physics of Plasmas, 23(1):013506, 2016.

[139] J. Teunissen. 3D Simulations and Analysis of Pulsed Discharges. PhD thesis, Department of Applied Physics, 11 2015. URL https://research.tue.nl/en/publications/3d-simulations-and-analysis-of-pulsed-discharges. Proefschrift.

[140] Zhen Wang, Anbang Sun, and Jannis Teunissen. A comparison of particle and fluid models for positive streamer discharges in air. Plasma Sources

Science and Technology, 31(1):015012, January 2022. doi:10.1088/1361-6595/ac417b.

[141] S Nijdam, G Wormeester, E M van Veldhuizen, and U Ebert. Probing background ionization: Positive streamers with varying pulse repetition rate and with a radioactive admixture. Journal of Physics D: Applied Physics, 44(45):455201, November 2011. doi:10.1088/0022-3727/44/45/455201.

[142] S Nijdam, E Takahashi, A H Markosyan, and U Ebert. Investigation of positive streamers by double-pulse experiments, effects of repetition rate and gas mixture. Plasma Sources Science and Technology, 23(2):025008, March 2014. doi:10.1088/0963-0252/23/2/025008.

[143] BOLSIG+ solver ver. 03/2016. www.lxcat.net.

[144] S. V. Pancheshnyi, S. V. Sobakin, S. M. Starikovskaya, and A. Yu. Starikovskii. Discharge dynamics and the production of active particles in a cathode-directed streamer. Plasma Physics Reports, 26(12):1054–1065, December 2000. doi:10.1134/1.1331141.

[145] Jannis Teunissen and Francesca Schiavello. Geometric multigrid method for solving poisson's equation on octree grids with irregular boundaries. Computer Physics Communications, 286:108665, May 2023. doi:10.1016/j.cpc.2023.108665.

[146] Xiaoran Li, Anbang Sun, Guanjun Zhang, and Jannis Teunissen. A computational study of positive streamers interacting with dielectrics. Plasma Sources Science and Technology, 29(6):065004, June 2020. doi:10.1088/1361-6595/ab8f75.

[147] Eric W. Hansen and Phaih-Lan Law. Recursive methods for computing the Abel transform and its inverse. Journal of the Optical Society of America A, 2(4):510, April 1985. doi:10.1364/JOSAA.2.000510.

[148] Ronald Schafer. What Is a Savitzky-Golay Filter? [Lecture Notes]. IEEE Signal Processing Magazine, 28(4):111–117, July 2011. doi:10.1109/MSP.2011.941097.

[149] Sergey Pancheshnyi. Effective ionization rate in nitrogen–oxygen mixtures. Journal of Physics D: Applied Physics, 46(15):155201, March 2013. doi:10.1088/0022-3727/46/15/155201.

[150] N. L. Aleksandrov and E. M. Bazelyan. Ionization processes in spark discharge plasmas. Plasma Sources Science and Technology, 8(2):285–294, January 1999. doi:10.1088/0963-0252/8/2/309.

[151] Z. Lj Petrović, S. Dujko, D. Marić, G. Malović, Ž Nikitović, O. Šašić, J. Jovanović, V. Stojanović, and M. Radmilović-Ra\djenović. Measurement and interpretation of swarm parameters and their application in plasma modelling. Journal of Physics D: Applied Physics, 42(19):194002, September 2009. doi:10.1088/0022-3727/42/19/194002.

[152] S Pancheshnyi. Role of electronegative gas admixtures in streamer start, propagation and branching phenomena. Plasma Sources Science and Technology, 14(4):645–653, November 2005. doi:10.1088/0963-0252/14/4/002.

[153] Jacob Stephens, Andrew Fierro, S Beeson, George Laity, D Trienekens, RP Joshi, James Dickens, and Andreas Neuber. Photoionization capable, extreme and vacuum ultraviolet emission in developing low temperature plasmas in air. Plasma Sources Science and Technology, 25(2):025024, 2016.

[154] Ming Jiang, Yongdong Li, Hongguang Wang, Pengfeng Zhong, and Chunliang Liu. A photoionization model considering lifetime of high excited states of n2 for pic-mcc simulations of positive streamers in air. Physics of Plasmas, 25(1), 2018.

[155] Fumiyoshi Tochikubo and Hideyuki Arai. Numerical Simulation of Streamer Propagation and Radical Reactions in Positive Corona Discharge in N2/NO and N2/O2/NO. Japanese Journal of Applied Physics, 41(2R): 844, February 2002. doi:10.1143/JJAP.41.844.

[156] G. V. Naidis. Effects of nonlocality on the dynamics of streamers in positive corona discharges. Technical Physics Letters, 23(6):493–494, June 1997. doi:10.1134/1.1261717.

[157] Chao Li, Ute Ebert, and Willem Hundsdorfer. Spatially hybrid computations for streamer discharges with generic features of pulled fronts: I. Planar fronts. Journal of Computational Physics, 229(1):200–220, January 2010. doi:10.1016/j.jcp.2009.09.027.

[158] V R Soloviev and V M Krivtsov. Surface barrier discharge modelling for aerodynamic applications. Journal of Physics D: Applied Physics, 42(12): 125208, June 2009. doi:10.1088/0022-3727/42/12/125208.

[159] Jannis Teunissen. Improvements for drift-diffusion plasma fluid models with explicit time integration. Plasma Sources Science and Technology, 29 (1):015010, January 2020. doi:10.1088/1361-6595/ab6757.

[160] M Bujotzek, M Seeger, F Schmidt, M Koch, and C Franck. Experimental investigation of streamer radius and length in SF $_6$. Journal of

Physics D: Applied Physics, 48(24):245201, June 2015. doi:10.1088/0022-3727/48/24/245201.

[161] R Morrow and J J Lowke. Streamer propagation in air. Journal of Physics D: Applied Physics, 30(4):614–627, February 1997. doi:10.1088/0022-3727/30/4/017.

[162] G. J. M. Hagelaar, F. J. de Hoog, and G. M. W. Kroesen. Boundary conditions in fluid models of gas discharges. Physical Review E, 62(1):1452–1454, July 2000. doi:10.1103/PhysRevE.62.1452.

[163] Hans Kristian Meyer, Frank Mauseth, Robert Marskar, Atle Pedersen, and Andreas Blaszczyk. Streamer and surface charge dynamics in non-uniform air gaps with a dielectric barrier. IEEE Transactions on Dielectrics and Electrical Insulation, 26(4):1163–1171, August 2019. doi:10.1109/TDEI.2019.007929.

[164] Weizhuo Hua and Koji Fukagata. Influence of grid resolution in fluid-model simulation of nanosecond dielectric barrier discharge plasma actuator. AIP Advances, 8(4):045209, April 2018. doi:10.1063/1.5013627.

[165] Anbang Sun, Jannis Teunissen, and Ute Ebert. The inception of pulsed discharges in air: Simulations in background fields above and below breakdown. Journal of Physics D: Applied Physics, 47(44):445205, November 2014. doi:10.1088/0022-3727/47/44/445205.

[166] M. Akyuz, L. Gao, V. Cooray, T. G. Gustavsson, S. M. Gubanski, and A. Larsson. Positive streamer discharges along insulating surfaces. IEEE Transactions on Dielectrics and Electrical Insulation, 8(6):902–910, December 2001. doi:10.1109/94.971444.

[167] Natalia Yu Babaeva and Mark J Kushner. Ion energy and angular distributions onto polymer surfaces delivered by dielectric barrier discharge filaments in air: I. Flat surfaces. Plasma Sources Science and Technology, 20(3):035017, June 2011. doi:10.1088/0963-0252/20/3/035017.

[168] S. A. Stepanyan, V. R. Soloviev, and S. M. Starikovskaia. An electric field in nanosecond surface dielectric barrier discharge at different polarities of the high voltage pulse: Spectroscopy measurements and numerical modeling. J. Phys. D: Appl. Phys., 47(48):485201, November 2014. doi:10.1088/0022-3727/47/48/485201.

[169] V Soloviev and V Krivtsov. Positive Streamer in the Surface Dielectric Barrier Discharge in Air: Numerical Modelling and Analytical Estimations. Journal of Physics: Conference Series, 927:012059, November 2017. doi:10.1088/1742-6596/927/1/012059.

[170] B. h Tan, N. l Allen, and H. Rodrigo. Progression of positive corona on cylindrical insulating surfaces. I. Influence of dielectric material. IEEE Transactions on Dielectrics and Electrical Insulation, 14(1):111–118, February 2007. doi:10.1109/TDEI.2007.302878.

[171] M. D. Campanell and M. V. Umansky. Strongly Emitting Surfaces Unable to Float below Plasma Potential. Physical Review Letters, 116(8), February 2016. doi:10.1103/PhysRevLett.116.085003.

[172] Y. Motoyama and F. Sato. Calculation of secondary electron emission yield /spl gamma/ from MgO surface. IEEE Transactions on Plasma Science, 34(2):336–342, April 2006. doi:10.1109/TPS.2006.872443.

[173] Yasushi Motoyama, Yoshikuni Hirano, Keiji Ishii, Yukio Murakami, and Fumio Sato. Influence of defect states on the secondary electron emission yield γ from MgO surface. Journal of Applied Physics, 95(12):8419–8424, June 2004. doi:10.1063/1.1751239.

[174] R Tschiersch, S Nemschokmichal, M Bogaczyk, and J Meichsner. Surface charge measurements on different dielectrics in diffuse and filamentary barrier discharges. Journal of Physics D: Applied Physics, 50(10):105207, Feb 2017. doi:10.1088/1361-6463/aa5605.

[175] Masamichi Fujihira and Hiroo Inokuchi. Photoemission from polyethylene. Chemical Physics Letters, 17(4):554–556, December 1972. doi:10.1016/0009-2614(72)85104-2.

[176] A. Buzulutskov, A. Breskin, and R. Chechik. Photoemission through thin dielectric coating films. Journal of Applied Physics, 81(1):466–479, January 1997. doi:10.1063/1.364082.

[177] Anna Alexandrovna Dubinova. Modeling of streamer discharges near dielectrics. PhD thesis, TU Eindhoven, Eindhoven, 2016. OCLC: 956923350.

[178] Chuanyang Li, Baojia Deng, Zi Zhang, Wu Yan, Qiuye Li, Zhousheng Zhang, Chuanjie Lin, Yao Zhou, Tao Han, Zhipeng Lei, Simone Vincenzo Suraci, and Davide Fabiani. Full life property of surface charge accumulation on HVDC spacers considering transient and steady states. IEEE Transactions on Dielectrics and Electrical Insulation, 26(5):1686–1692, October 2019. doi:10.1109/TDEI.2019.008243.

[179] Bangdou Huang, Cheng Zhang, Jintao Qiu, Xuan Zhang, Yujian Ding, and Tao Shao. The dynamics of discharge propagation and x-ray generation in nanosecond pulsed fast ionisation wave in 5 mbar nitrogen. Plasma Sources Science and Technology, 28(9):095001, September 2019. doi:10.1088/1361-6595/ab3939.

[180] Xiaobo Meng, Hongwei Mei, Liming Wang, Zhicheng Guan, and Jun Zhou. Characteristics of streamer propagation along the insulation surface: Influence of air pressure and humidity. IEEE Transactions on Dielectrics and Electrical Insulation, 24(1):391–400, February 2017. doi:10.1109/TDEI.2016.005966.

[181] A Chachereau, A Hösl, and C M Franck. Electrical insulation properties of the perfluoronitrile C $_4$ F $_7$ N. Journal of Physics D: Applied Physics, 51(49):495201, December 2018. doi:10.1088/1361-6463/aae458.

[182] Boya Zhang, Jiayu Xiong, Li Chen, Xingwen Li, and Anthony B Murphy. Fundamental physicochemical properties of SF $_6$ -alternative gases: A review of recent progress. Journal of Physics D: Applied Physics, 53(17):173001, April 2020. doi:10.1088/1361-6463/ab6ea1.

[183] Marija Grofulović, Luís L. Alves, and Vasco Guerra. Electron-neutral scattering cross sections for CO2: A complete and consistent set and an assessment of dissociation. Journal of Physics D: Applied Physics, 49(39):395207, September 2016. doi:10.1088/0022-3727/49/39/395207.

[184] L. C. Pitchford and A. V. Phelps. Comparative calculations of electron-swarm properties in N 2 at moderate E N values. Physical Review A, 25(1):540–554, January 1982. doi:10.1103/PhysRevA.25.540.

[185] P. J. Chantry. Dissociative Attachment in Carbon Dioxide. The Journal of Chemical Physics, 57(8):3180–3186, October 1972. doi:10.1063/1.1678736.

[186] W. F. Chan, G. Cooper, and C. E. Brion. The electronic spectrum of carbon dioxide. Discrete and continuum photoabsorption oscillator strengths (6–203 eV). Chemical Physics, 178(1):401–413, December 1993. doi:10.1016/0301-0104(93)85079-N.

[187] Dennis Bouwman, Jannis Teunissen, and Ute Ebert. 3D particle simulations of positive air–methane streamers for combustion. Plasma Sources Science and Technology, 31(4):045023, April 2022. doi:10.1088/1361-6595/ac64bf.

[188] G V Naidis. Conditions for inception of positive corona discharges in air. Journal of Physics D: Applied Physics, 38(13):2211–2214, July 2005. doi:10.1088/0022-3727/38/13/020.

[189] Carolynne Montijn and Ute Ebert. Diffusion correction to the Raether-Meek criterion for the avalanche-to-streamer transition. J. Phys. D: Appl. Phys., 39(14):2979–2992, July 2006. doi:10.1088/0022-3727/39/14/017.

[190] W. Sroka. Light Emission in the VUV by Dissociative Excitation of CO2 with Low-Energy Electrons. Zeitschrift für Naturforschung A, 25(10):1434–1441, October 1970. doi:10.1515/zna-1970-1013.

Acknowledgements

As Karl Marx said, *"The human essence is the ensemble of social relations"*, I would like to express my gratitude to all the people I have met in my life. Without you, there would be no current version of Xiaoran Li.

Firstly, I would like to thank my promoter, Anbang Sun, Ute Ebert, and my co-promoter, Jannis Teunissen. Thanks to Prof. Sun, who has a sharp vision and a broad mind, I was provided with a platform for international cooperation. Thanks to Prof. Ebert, who made efforts to establish the double doctorate degree program between Eindhoven University of Technology and Xi'an Jiaotong University and accepted me as a joint PhD student in her group. Thanks to Dr. Teunissen, who supported me in every aspect of my research. Without you, this thesis wouldn't be here.

I am grateful to Prof. Guanjun Zhang, who was my promoter during my master's period and the first guide of my academic career. I extend my thanks to all the members of the FGM group, including Wendong Li, Zhe Liu, Liyuan Zhang, Chao Wang, and Zhihui Jiang. You were all there, striving alongside me when we were all academic beginners.

I was very glad to have met all the members of the Multiscale Dynamics group at CWI. Bastiaan Braams, Hani Francisco, Hemaditya Malla, Dennis Bouwman, Baohong Guo, and Zhen Wang, I am incredibly grateful to be part of such a diverse group, and you were so kind to me. And I am grateful to Sander Nijdam and Siebe Dijcks from Eindhoven University of Technology for their collaboration on model validation.

In the two years I spent in Amsterdam, I was fortunate to find new companions. Xuan Zheng, Zhouping Lyu, Wenfei Du, Shibo Zou, Xuemei Zhou, and Chen Xiao, you brought me so much happiness when I was away from home.

When I returned to Xi'an, I was happy to be welcomed by colleagues from the HVDP team. I acknowledge all the group members to help me adapt to the new environment, especially Haolin Li, Yaqi Zhang, and Yulin Guo. I cherish the time spent as your office mate.

My special thanks go to Xuequan Xu and Jiaming Shen, who accompanied me for 12 years. You were always by my side, sharing my ups and downs. I hope we can continue to be together in our next life stage.

Finally, my deep gratitude goes to my boyfriend, Yaoyu Xu, who cheered me

up throughout my entire PhD journey. We have grown together and we have become an even better match. And, of course, to my parents, my little brother, my grandparents, and all my family members—your love is my greatest source of motivation. I hope I can always be your good girl and never let you down.

In the end, I would like to acknowledge Prof. Barry Koren, Prof. Wim van Saarloos, Prof. Yongdong Li, and Prof. Xu Yang for serving on my committee board. Also, thank you to whoever is reading this thesis. I hope it won't disappoint you.

Curriculum Vitae

Xiaoran Li was born in Handan, Hebei Province, China, on January 11, 1996. She obtained her bachelor's degree in Electrical Engineering and Automation at Xi'an Jiaotong University in 2017. Then she started her master in High Voltage and Insulation Technology, also at Xi'an Jiaotong University. In February 2020, she enrolled in a double doctoral degree program between Eindhoven University of Technology, Department of Applied Physics, and Xi'an Jiaotong University, School of Electrical Engineering. For this project, she joined the Multiscale Dynamics group at the CWI (Centrum Wiskunde & Informatica) from September 2020 to August 2022. For the rest of her PhD, she worked at Xi'an Jiaotong University, supervised by Anbang Sun.

ORCID:
https://orcid.org/0000-0003-3354-9078
Google scholar:
https://scholar.google.com/citations?hl=zh-CN&user=E-P6JFsAAAAJ

List of publications

[1] **X. Li**, B. Guo, A. Sun, U. Ebert, and J. Teunissen. A computational study of steady and stagnating positive streamers in N_2–O_2 mixtures. Plasma Sources Sci. Technol., vol. 31, no. 6, p. 065011, Jun. 2022. (Chapter 4)

[2] **X. Li**, S. Dijcks, S. Nijdam, A. Sun, U. Ebert, and J. Teunissen. Comparing simulations and experiments of positive streamers in air: steps toward model validation. Plasma Sources Sci. Technol., vol. 30, no. 9, p. 095002, Sep. 2021. (Chapter 3)

[3] **X. Li**, A. Sun, and J. Teunissen. A computational study of negative surface discharges: Characteristics of surface streamers and surface charges. IEEE Transactions on Dielectrics and Electrical Insulation, vol. 27, no. 4, pp. 1178–1186, Aug. 2020. (Chapter 5)

[4] **X. Li**, A. Sun, G. Zhang, and J. Teunissen. A computational study of positive streamers interacting with dielectrics. Plasma Sources Sci. Technol., vol. 29, no. 6, p. 065004, Jun. 2020. (Chapter 5)

[5] **X. Li**, A. Sun, and J. Teunissen. The effect of photoionization on positive streamers in CO_2 studied with 2D particle-in-cell simulations. Submitted to Plasma Sources Sci. Technol. (Chapter 6)

[6] **X. Li**, Z. Liu, W. Li, G. Sun, J. Xue, C. Wang, and G. Zhang. 3D printing fabrication of conductivity non-uniform insulator for surface flashover mitigation. IEEE Transactions on Dielectrics and Electrical Insulation, vol. 26, no. 4, pp. 1172–1180, Aug. 2019.

[7] B. Guo, **X. Li**, U. Ebert, and J. Teunissen. A computational study of accelerating, steady and fading negative streamers in ambient air. Plasma Sources Sci. Technol., vol. 31, no. 9, p. 095011, Sep. 2022.

[8] W. Li, **X. Li**, B. Guo, C. Wang, Z. Liu, and G. Zhang. Topology optimization of truncated cone insulator with graded permittivity using variable density method. IEEE Transactions on Dielectrics and Electrical Insulation, vol. 26, no. 1, pp. 1-9, Feb. 2019.

[9] X. Yuan, H. Li, M. Abbas, **X. Li**, et al. A 3D numerical study of positive streamers interacting with localized plasma regions. J. Phys. D: Appl. Phys., vol. 53, no. 42, p. 425204, Jul. 2020.

Contributions to conferences

[1] **X. Li**, A. Sun, and J. Teunissen. The effect of photoionization on positive streamers in CO_2 studied with 2D particle-in-cell simulations. International Conference on Phenomena in Ionized Gases (ICPIG) XXXV, Egmond aan Zee, the Netherlands, July 2023. (Oral)

[2] **X. Li**, B. Guo, A. Sun, U. Ebert, and J. Teunissen. Steady propagation of positive streamers in air in different background electric fields. The XXV Europhysics Conference on the Atomic and Molecular Physics of Ionized Gases (ESCAMPIG). Paris, France, July 2022. (Poster)

[3] **X. Li**, S. Dijcks, S. Nijdam, A. Sun, U. Ebert, and J. Teunissen. Comparing simulations and experiments of positive streamers in air: steps toward model validation. Physics@Veldhoven, Jan. 2022. (Online, Poster)

[4] **X. Li**, A. Sun, and J. Teunissen. 2D Fluid Simulations of the Interaction Between Streamers and Dielectrics: Characteristics of Surface Charge. 47th IEEE International Conference on Plasma Science (ICOPS), Dec. 2020. (Online, Poster)

[5] **X. Li**, J. Guo, W. Li, L. Zhang, C. Wang, and G. Zhang. Analysis of Morphology and Electrical Insulation of 3D Printing Parts. 2018 IEEE International Conference on High Voltage Engineering and Application (ICHVE). Athens, Greece, Spet. 2018. (Poster)

Summary

Streamer discharges are a common initial stage of electrical discharges. They create the first ionized paths for later heat-dominated spark discharges, playing an important role in electric breakdown in nature and in high voltage devices. Simulations, which provide a full temporal and spatial evolution of fields and plasma species, are powerful tools for studying the physics of streamer discharges. They allow for the deactivation or artificial amplification of physical mechanisms, offering a detailed understanding of complex behavior of streamers.

This thesis takes a further step on previous computational studies on streamer discharges. We focus on four open questions on discharges in high-voltage devices, namely how accurate are current commonly used simulation models, how streamer properties depend on the background electric field, how streamers interact with dielectrics, and how positive streamers propagate in gases different from air.

First, simulations and experiments of positive streamer discharges in air at 100 mbar were compared for model validation. Single-filament streamers were generated in a plate-plate geometry with a protruding needle and their evolution was captured with a high-speed camera. A 2D axisymmetric drift-diffusion-reaction fluid model was used to simulate streamers under closely matched conditions. Good qualitative agreement was achieved between the experimental and simulated optical emission profiles, as well as the streamer velocity and radius throughout the evolution. However, quantitatively, the simulated streamer velocity and radius were approximately 20% to 30% smaller. The study examined the impact of various parameters, such as transport data, background ionization levels, photoionization rates, gas temperatures, voltage rise time, and voltage boundary conditions on the agreement between the simulations and experiments. The observed discrepancies could potentially be attributed to an increase in gas temperature caused by the experimental discharge repetition frequency of 50 Hz.

Second, streamers can be accelerating, steady or stagnating in different electric fields. We explored steady propagation fields for positive streamers in air and streamer deceleration in fields below the steady propagation field. To generate constant-velocity positive streamers, an axisymmetric fluid model is employed, adjusting the applied voltage based on the streamer velocity. Steady propagation is observed for streamers at constant velocities ranging from 3×10^4 m/s to

1.2×10^5 m/s, with no changes in the background field during this phase. Interestingly, faster streamers can propagate in lower background fields than slower ones, indicating the absence of a unique stability field. The study establishes a relationship between streamer radius, velocity, maximal electric field, background electric field, and a characteristic time scale for conductivity loss. Additionally, the deceleration of streamers is investigated, and a phenomenological model with fitted coefficients is presented to describe the evolution of velocity and radius for stagnating streamers. A comparison is also made between the lengths of stagnated streamers and predictions based on the conventional stability field.

Third, we performed simulations to explore streamers that propagate towards a dielectric surface, attach to it, and propagate along it with a 2D fluid model. It was found that streamers are attracted to dielectrics via electrostatic forces. Compared to streamers in bulk gas, surface streamers have smaller radii, higher electric fields, and greater electron densities, resulting in faster propagation. Positive surface streamers have a high electric field and low electron density area between the streamer head and the dielectric, while negative ones may touch the surface, creating a high field area inside the dielectric. Various parameters were investigated, including applied voltage, dielectric permittivity, secondary electron emission, positive ion mobility, and preset surface charges. A higher applied voltage increases streamer velocities for both polarities. Higher permittivity dielectrics accelerate surface streamer formation for positive polarity, while negative streamers in such conditions experience slower development. Electron emission from dielectric surfaces hardly affects positive streamer velocity due to strong photoionization in air. Preset positive surface charge accelerates negative streamer development around dielectrics, while negative surface charge delays or inhibits negative surface discharges. Additionally, 3D particle simulations were performed for positive surface discharges, revealing both surface and gas-phase streamer components, as has also been observed in experiments.

Finally, we focused on streamers in CO_2, which is increasingly used as an insulating gas in high voltage devices. Discharges in CO_2 exhibit significant differences compared to in air. In air, positive streamers rely on photoionization to create free electrons ahead of them, but photoionization is much weaker in CO_2 due to a smaller number of ionizing photons and shorter absorption distances. We examine the impact of photoionization on positive streamer propagation in CO_2 using 2D particle-in-cell simulations. Our computational results suggest that even a small amount of photoionization can sustain positive streamer propagation in CO_2, but only with a higher electric field around the streamer head compared to air. Additionally, we propose a self-sustaining criterion for streamer discharges in CO_2, based on the idea that a single photoionization event should produce, on average, at least one additional photoionization event. We also discuss the uncertainties associated with our photoionization model.